

DAHP OXIME: A TRANSITION STATE MIMIC INHIBITOR OF DAHPS

DAHP OXIME: A TRANSITION STATE MIMIC INHIBITOR OF DAHP
SYNTHASE

By

NARESH BALACHANDRAN, B. Sc.

A Thesis

Submitted to the School of Graduate Studies

in Partial Fulfillment of the Requirements

for the Degree

Doctor of Philosophy

McMaster University

© Copyright by Naresh Balachandran, May 2014

DOCTOR OF PHILOSOPHY
(Chemical Biology Graduate Program)

McMaster University
Hamilton, Ontario

TITLE: DAHP Oxime: A Transition State Mimic Inhibitor Of
DAHP Synthase

AUTHOR: Naresh Balachandran, B. Sc.

SUPERVISOR: Dr. Paul Berti

NUMBER OF PAGES: xv, 183

Abstract

The rise of bacterial infections and increase of antibiotic resistant bacteria has become a major problem in the treatment of bacterial infections. The use and overuse of antibiotics, and the inherent ability of bacteria to adapt to their environment, have led to the emergence of strains that are resistant to all antibiotics. Ideally, new targets for antibacterial drug therapy would be essential to the virulence of most or all bacteria. That is, antibiotics exploiting these targets would have broad spectrum activity. 3-Deoxy-D-arabinoheptulosonate-7-phosphate (DAHP) synthase could be such a target. This enzyme catalyzes the condensation of erythrose 4-phosphate (E4P) and phosphoenolpyruvate (PEP) to form DAHP. The DAHP synthase-catalyzed reaction is the first committed step in the shikimic acid biosynthetic pathway leading to the aromatic amino acids and other secondary metabolites in all bacteria and some parasites. Inhibition of this enzyme would lead to a depletion of aromatic amino acids within the cell, halting new protein synthesis and killing the cells. Our lab has developed a transition state analogue, DAHP oxime, which is a slow binding, potent inhibitor of DAHP synthase. Kinetic characterization of inhibitor binding revealed DAHP oxime to be a competitive inhibitor with an ultimate K_i^* of 81 nM. Crystal structures of DAHP oxime bound to DAHP synthase revealed that the inhibitor bound to two of the four subunits. The two unbound subunits remain catalytically competent, suggesting that DAHP synthase may utilize a half-of-sites mechanism during catalysis. We further investigated changes in DAHP synthase dynamics in

response to PEP and DAHP oxime binding via solvent hydrogen/deuterium exchange mass spectrometry. DAHP synthase in the unbound form was loosely structured around the surface exposed regions, whereas the X-ray crystal structures appeared to be more fully structured. Binding of both PEP and DAHP oxime introduced different degrees of dynamic stabilization.

Acknowledgements

I would like to take this opportunity to thank my supervisor, Dr. Paul Berti, for giving the opportunity to work in his lab. Your guidance, support and patience have made this possible. Thank you.

To my supervisory committee, Dr. Murray Junop and Dr. John Valliant, for your continuous support and advice throughout this project.

This would not have been possible without the unwavering support and encouragement of my family. Thank you for always believing in me.

I would like to thank all Berti lab members both past and present, Vincent Azhikannickal, Rasa Bakhtiari, Simanga Gama, Lisset Llano, Maren Heimhalt, Vladamir Popović, Shan Jiang, Fred To, Jennifer Wild, Kelvin Tsao, Vamana Rajeswaran, Lauren Wilson, Xiaoyi Ji, Peter Kim, Jenny Zheng, Adam Mephram, Jason Thomas, Edward Morrison, Grace Lou and Mohammed Chagalov. It has been a privilege working with you.

Finally, I would like to thank the numerous collaborators that have contributed to this work. Dr. Murray Junop and Dr. Ting-Wai Lee for your help with solving the crystal structures. Dr. Derek Wilson, Tamanna Rob and Peter Liuni from the Wilson group (York University) who ran all H/D exchange experiments. Dr. Dan Sorensen (McMaster NMR facility) who collected the fluorine NMR spectra. Dr. Rajeevan Selvaratnam and Dr. Giuseppe Melacini for their help with the TROSY experiments. I need to also thank Fred To who determined the steady state kinetic parameters of the DAHPS mutants.

Table of Contents

Abstract	iii
Acknowledgements	v
Table of Contents	vi
List of Figures	ix
List of Tables	xii
List of Schemes	xiii
List of Abbreviations	xiv
Chapter 1 - Introduction	1
1.1. Overview	1
1.2. Antibiotic Resistance	1
1.3. The Shikimic Acid Biosynthetic Pathway	3
1.4. DAHPS	7
1.5. DAHPS Homologues	11
1.5.1. KDO8P Synthase	12
1.5.2. NeuB	14
1.6. Catalysis	16
1.7. Inhibitors	18
1.8. Slow Binding Inhibitors	21
1.9. Cooperativity	22
1.10. DAHPS Inhibitors	23
1.11. KDO8PS/NeuB inhibitors	25
1.12. Oxime Inhibitors	27
1.13. Object of Research	27
Chapter 2 - Kinetics	29
2.1. Introduction	29
2.2. Materials and Methods	29
2.2.1. DAHP Synthase (Phe) Purification	29
2.2.2. Steady State Kinetics	30
2.2.3. E4P synthesis	32
2.2.4. DAHP Oxime Synthesis	33
2.2.5. Activation of DAHPS _{H6} by Various Metals	34
2.2.6. DAHPS _{H6} Inhibition with DAHP Oxime	34
2.2.7. Slow-binding Inhibition of DAHPS _{H6} by DAHP Oxime	35
2.2.8. Slow-binding Association Rate Constant, k_{on}	35
2.2.9. Slow-binding Dissociation Rate Constant, k_{off}	36
2.2.10. Substrate Dependence of Inhibition	37
2.2.11. Inhibition of DAHPS _{H6} During Catalytic Turnover	37
2.2.12. Tryptophan Fluorescence	38
2.2.13. Determination of the Oligomeric Form of DAHPS _{H6} by Gel filtration	38

2.2.14. Glutaraldehyde Cross-linking	39
2.2.15. Bacterial Culture Growth Assays	40
2.3. Results	41
2.3.1. Protein Purification	41
2.3.2. DAHPS _{H6} Steady State Kinetics	41
2.3.3. Metal Dependence of DAHPS Activity	43
2.3.4. Inhibition	46
2.3.5. Substrate Dependence of Inhibition	47
2.3.6. Slow-Binding Inhibition	52
2.3.7. BSA effects	60
2.3.8. Oligomerization	61
2.4. Discussion	69
2.4.1. Kinetics	69
2.4.2. Oligomeric Form	72
2.4.3. Inhibition	72
2.4.4. Slow Binding Inhibition	77
2.4.5. Residual rate	79
2.4.6. Cooperativity	80
Chapter 3 - X-ray Crystallography	88
3.1. Introduction	88
3.2. Materials and Methods	89
3.2.1. Construction of a TEV-cleavable N-terminal His ₆ -tagged DAHPS: DAHPS _{H6-TEV}	89
3.2.2. Purification of TEV-cleavable His ₆ -tagged DAHPS(Phe): DAHPS _{H6-TEV}	92
3.2.3. Purification of TEV Protease	93
3.2.4. Crystallography	94
3.3. Results	94
3.3.1. DAHPS _G •DAHP Oxime Structure	101
3.3.2. DAHP Oxime Binding	107
3.3.3. Unbound Structures	108
3.3.4. Cocrystallization of Inhibitor/Substrates/Phenylalanine	109
3.4. Discussion	111
Chapter 4 - DAHP Synthase Dynamics	119
4.1. Introduction	119
4.1.1. NMR	119
4.1.2. TROSY NMR	119
4.1.3. ¹⁹ F NMR	120
4.1.4. H/D Exchange by Mass Spectrometry	120
4.2. Materials and Methods	122
4.2.1. Purification of DAHPS _G for H/D exchange experiments	122
4.2.2. H/D Exchange Experiments	122

4.2.3. Labelling of DAHPS with 5-Fluorotryptophan or $^{15}\text{N}_2$ -Tryptophan	124
4.2.4. ^{19}F NMR	125
^{15}N -Tryptophan NMR	126
4.3. Results	126
4.3.1. ^{19}F NMR	126
4.3.2. Global H/D Exchange	130
4.3.3. Spatially Resolved H/D Exchange	131
4.4. Discussion	137
Chapter 5 - Linear Free Energy Relationship Analysis of DAHP Oxime Binding	140
5.1. Introduction	140
5.2. Materials and Methods	144
5.2.1. DAHPS _{H6} Mutagenesis	144
5.2.2. Expression and purification of Mutant DAHPS _{H6} 's	145
5.2.3. DAHPS _{H6} Mutant Kinetics/Inhibition	146
5.3. Results	146
5.4. Discussion	150
5.4.1. Effects of Mutations	150
5.4.2. LFER Analysis	151
5.4.3. Transition state mimicry	152
5.4.4. LFER Slopes	154
5.4.5. Transition State versus Substrate Mimicry	156
Chapter 6 - Concluding Remarks	159
6.1. Conclusions	159
6.2. Future work	160
Appendix	163
References	166

List of Figures

Figure 1.1: General reaction of α -carboxyketose synthases.....	4
Figure 1.2: Shikimate Pathway.....	6
Figure 1.3: Crystal structure of <i>E. coli</i> phenylalanine-regulated DAHPS.....	10
Figure 1.4: Coordination of PEP and Mn^{2+} in DAHPS active site.....	11
Figure 1.5: Lipopolysaccharide (LPS) of Gram negative bacteria.....	13
Figure 1.6: NeuB crystal structure.....	16
Figure 1.7: Proposed mechanism of DAHPS.....	17
Figure 1.8: Modes of inhibition by reversible inhibitors.....	19
Figure 1.9: Kinetic mechanism for slow binding inhibition.....	22
Figure 1.10: Inhibitors of DAHPS.....	24
Figure 1.11: Inhibitors of KDO8PS and NeuB.....	26
Figure 1.12: Oxime inhibitors of NeuB and DAHPS.....	28
Figure 2.1: 13% SDS-PAGE gel of DAHPS _{H6}	41
Figure 2.2: DAHPS _{H6} steady state kinetics.....	43
Figure 2.3: Activation of demetallated DAHPS _{H6} by various divalent metal ions relative to Mn^{2+}	45
Figure 2.4: Fast-binding inhibition of DAHPS _{H6} by DAHP oxime.....	46
Figure 2.5: Inhibition of catalytic enzyme.....	47
Figure 2.6: Substrate and metal dependence of DAHP oxime inhibition.....	50
Figure 2.7: Substrate and metal dependence of DAHP oxime inhibition.....	51
Figure 2.8: Metal ion dependence of DAHP oxime inhibition.....	52
Figure 2.9: Time dependent inhibition of DAHPS _{H6} with DAHP oxime.....	53
Figure 2.10: Determining the $E^* \cdot I$ dissociation rate.....	54
Figure 2.11: Inhibition curve depicting rate vs. DAHP oxime concentration.....	56
Figure 2.12: Inhibition of DAHPS _{H6} with DAHP oxime, shows cooperative binding when DAHPS _{H6} and DAHP oxime are preincubated.....	57
Figure 2.13: Inhibition profile of DAHPS _{H6} by DAHP <i>O</i> -ethyloxime.....	58
Figure 2.14: Inhibition profile of DAHPS _{H6} by DAHP <i>O</i> -(2-fluoroethyl)oxime.....	59
Figure 2.15: Effect of BSA on DAHPS _{H6} inhibition by DAHP oxime.....	60
Figure 2.16: DAHPS _{H6} on Superose 12 10/300 GL column.....	62

Figure 2.17: 10% native gel electrophoresis of DAHPS _{H6} cross-linked with and without DAHP oxime.	63
Figure 2.18: Tryptophan fluorescence vs. temperature of DAHP _{H6} in the presence and absence of PEP.	66
Figure 2.19: In culture assay of DAHP oxime against <i>E. coli</i> cells lines.	68
Figure 2.20: Structure of the EPSP synthase inhibitor glyphosate.	77
Figure 2.21: Thermodynamic box of inhibitor binding and conformational change.	84
Figure 2.22: Schematic representation of oxime binding.	86
Figure 3.1: Sequence of His ₆ -tagged, TEV protease cleavable DAHPS, DAHPS _{H6} -TEV.	90
Figure 3.2: Thermal cycling parameters for Gateway cloning.	92
Figure 3.3: DAHPS _G •DAHP oxime crystal structure from Wai003_4_10.	101
Figure 3.4: R-factors in the DAHPS _G •DAHP oxime structure, Wai003_4_10.	104
Figure 3.5: Alignment of DAHPS _G subunits C and D from the DAHP oxime-bound structure Wai003_4_10.	106
Figure 3.6: DAHPS _G binding site with DAHP oxime. Subunit C of Wai003_4_10 is shown.	108
Figure 3.7: Electron density map showing unidentified electron density.	110
Figure 3.8: Observed conformations in DAHPS _G and DAHPS _G •ligand crystal structures.	112
Figure 3.9: Proposed catalytic cycle for <i>E. coli</i> KDO8PS.	117
Figure 4.1: Schematic of the global H/D exchange experiment setup.	123
Figure 4.2: Diagram of the spatially resolved H/D exchange experiments.	124
Figure 4.3: ¹⁹ F NMR spectra of 5-fluorotryptophan labelled DAHPS _G	129
Figure 4.4: Global H/D exchange data for free DAHPS _G , DAHPS _G •DAHP oxime and DAHPS _G •PEP.	131
Figure 4.5: %N _{fast} vs. %N _{loop} of DAHPS _G	134
Figure 4.6: Differences in %N _{fast} amplitude between free DAHPS _G and DAHPS _G •PEP.	135
Figure 4.7: %N _{fast} vs. %N _{loop} of DAHPS _G •DAHP oxime.	136
Figure 4.8: Comparison of PF between free DAHPS _G and DAHPS _G •DAHP oxime.	137

Figure 5.1: Thermodynamic cycle of enzyme binding substrate (S) and transition state (S^\ddagger).....	141
Figure 5.2: Thermodynamic cycle for two substrates.	143
Figure 5.3: Temperature cycling method used for mutagenesis.....	145
Figure 5.4: DAHPS _{H6} mutants.....	147
Figure 5.5: Linear free energy relationships for DAHP oxime.	149
Figure 5.6: DAHP oxime vs. PEP binding.	154
Figure 5.7: Linear correlation of K_i of DAHP oxime with K_M values.....	157
Figure 5.8: Linear correlation of K_i for DAHP oxime with k_{cat}	158
Figure A.1: NMR spectrum of DAHP oxime.....	165
Figure A.2: High resolution mass spectrum of DAHP oxime.....	165

List of Tables

Table 2.1: Steady state kinetic parameters for DAHPS _{H6}	42
Table 2.2: ICP-MS analysis of purified protein.	44
Table 2.3: Superose 12 10/300 GL column calibration and DAHPS _{H6} molecular weights.	62
Table 2.4: Steady state kinetic parameters for <i>E. coli</i> DAHPS(Phe).	71
Table 3.1: Crystallization conditions used in this study.	96
Table 3.2: X-ray data collection and refinement statistics of unique DAHPS _G structures.	97
Table 3.3: Structural alignment of subunits within the Wai003_4_10 tetramer: Root mean square deviation (rmsd) of C α atoms.	103
Table 4.1: Time resolved H/D exchange statistics for free and PEP-bound DAHPS _G peptides.	133
Table 4.2: Time-resolved H/D exchange statistics from DAHP oxime bound DAHPS _G peptides.	136
Table 5.1: Mutagenesis primers.	145
Table 5.2: Steady state kinetic parameters for DAHPS _{H6} and mutants ^a	148
Table 5.3: Catalytic impairment by mutations ^a	148
Table A.1: ¹ H and ¹³ C assignment of DAHP oxime.	165

List of Schemes

Scheme 2.1: Kinetic scheme for slow-binding inhibition.	52
Scheme 2.2: Schematic representation of enzyme inhibition.	73
Scheme 2.3: Different modes of slow binding inhibition.	78

List of Abbreviations

A5P	D-arabinose-5-phosphate
BSA	bovine serum albumin
CMP-KDO	cytosine monophosphate-3-deoxy-D- <i>manno</i> -oct-2-ulosonic acid
cAMP	cyclic adenosine monophosphate
CAP	catabolite activator protein
DAHPS	3-deoxy-D- <i>arabino</i> -2-heptulosonate-7-phosphate
DAHPS	DAHPS synthase
DAHPS _G	<i>E. coli</i> DAHPS(Phe) containing an <i>N</i> -terminal Gly residue
DAHPS _{H6}	<i>E. coli</i> DAHPS(Phe) containing an <i>N</i> -terminal His ₆ -tag
DAHPS _{H6-TEV}	<i>E. coli</i> DAHPS(Phe) containing a TEV cleavable <i>N</i> -terminal His ₆ -tag
DTT	dithiothreitol
DXR	1- deoxy-D-xylulose 5-phosphate reductoisomerase
<i>E. coli</i>	<i>Escherichia coli</i>
E	enzyme
EI	enzyme inhibitor complex
E*I	tightly bound enzyme inhibitor complex
E4P	D-erythrose-4-phosphate
EDTA	ethylenediaminetetraacetic acid
EPSP	5-enolpyruvylshikimic acid-3-phosphate
ES [‡]	enzyme•transition state complex
HEPES	4-(2-hydroxyethyl)-1-piperazineethanesulfonic acid
ICP-MS	inductively coupled plasma mass spectrometry
IPTG	isopropyl β-D-1-thiogalactopyranoside
k_{cl}	rate of forming hydrogen bonds
K_d	equilibrium dissociation constant for any ligand
K_i	equilibrium dissociation constant for inhibitor binding
K_M	Michaelis constant
k_{off}	rate constant for dissociation of inhibitor from enzyme
k_{on}	rate constant for binding of inhibitor to enzyme
k_{op}	rate of breaking hydrogen bonds
K_s	equilibrium dissociation constant for substrate(s)
KDO8P	3-deoxy-D- <i>manno</i> -2-octulosonate-8-phosphate
KDO8PS	3-deoxy-D- <i>manno</i> -2-octulosonate-8-phosphate synthase
KNF	Koshland-Némethy-Filmer
LB	lysogeny broth
LPS	lipopolysaccharide
ManNAc	<i>N</i> -acetylmannosamine
MWC	Monod-Wyman-Changeux
NeuB	sialic acid synthase
NeuNAc	<i>N</i> -acetylneuraminic acid
NMR	nuclear magnetic resonance

PAGE	polyacrylamide gel electrophoresis
PEP	phosphoenolpyruvate
Phe	phenylalanine
PF	protection factor
S	substrate(s)
<i>S. aureus</i>	<i>Staphylococcus aureus</i>
SAXS	small angle x-ray scattering
SDS	sodium dodecyl sulfate
TCEP	tris(2-carboxyethyl)phosphine
TEV	tobacco etch virus
THI	tetrahedral intermediate
Tris	tris(hydroxymethyl)amino methane
TS	transition state

Standard one-letter abbreviations are used for amino acid residues:

A	Ala
C	Cys
D	Asp
E	Glu
F	Phe
G	Gly
H	His
I	Ile
K	Lys
L	Leu
M	Met
N	Asn
P	Pro
Q	Gln
R	Arg
S	Ser
T	Thr
V	Val
W	Trp
Y	Tyr

Chapter 1 - Introduction

1.1. Overview

This thesis reports the investigation of the inhibition of 3-deoxy-D-*arabino*-2-heptulosonate-7-phosphate synthase (DAHPS) by oxime-based inhibitors. DAHPS is a member of the α -carboxyketose superfamily of enzymes. These enzymes are potential antibiotic targets because they are essential to bacterial pathogenicity, and they do not occur in mammals. Understanding how oxime-based inhibitors work, and their limitations, is important for understanding how to develop more potent inhibitors that could eventually act as lead compounds for new antibiotics. Understanding DAHPS inhibition has required studying aspects of its catalytic mechanism, including its half-of-sites reactivity, slow-binding inhibition, cooperativity of inhibition, as well as the protein's structure and dynamics.

1.2. Antibiotic Resistance

The discovery of antibiotics drastically changed the treatment of bacterial infections. However, with antibiotics also came bacterial resistance to antibiotics.

Penicillin was as discovered in the mid-1930's, and was introduced for public use in 1942, but resistance was already observed in laboratories in 1940.¹⁻³ The onset of resistance is rapid; within 5 years of being on the market, the susceptibility of bacteria to any antibiotic is substantially reduced.^{1,2} Between

1945 and 1949 the level of resistance to penicillin in *Staphylococcus aureus* increased from < 8% to 60%.

The rise in resistance is attributable to many factors.³ Improper use of antibiotics is a major contributing factor.⁴ A survey of 900 people found that 44% of adults on antibiotics skip doses, 45% believed antibiotics can be used for viral as well as for bacterial infections, and healthcare providers were willing to provide prescription for antibiotics when asked, whether or not they are clinically indicated. First generation antibiotics were from natural products, and as such, resistance had already developed, but was not widespread. Intensive use of antibiotics in the clinic allowed resistant strains to become widespread.³ Bacterial resistance to antibiotics appears in many forms, including, enzymatic alteration of the drug, mutations within the target enzyme, and efflux pumps.⁵⁻⁷

Current antibiotics target a small number of enzymes/pathways that are involved in cell growth, including DNA repair/replication, protein synthesis and cell wall biosynthesis.⁸ These targets were identified and utilized in the mid 20th century. Most classes of antibiotics in use today were identified in the 1940's and 1950's. Since 1960 the rate of advance has slowed.^{9,10} Most new antibiotics that have been introduced, or are in the pipeline for approval, are structural variants of previous antibiotics. Bacteria have acquired resistance to all commonly used antibiotics. Of particular concern are the ESKAPE pathogens (*Enterococcus faecium*, *Staphylococcus aureus*, *Klebsiella pneumoniae* (including *Escherichia coli*), *Acinetobacter baumannii*, *Pseudomonas aeruginosa* and *Enterobacter*

species) as they are responsible for majority of hospital acquired infection and are resistant to multiple antibiotic treatments.¹¹ Pan-resistant bacteria, that is bacteria which are resistant to all antibiotics, have been identified.¹² Many pharmaceutical companies, including Roche, Eli Lilly, GSK and Bristol-Myers Squibb have scaled back or stopped their research in the field due to the cost of development, short drug life cycles due to resistance, large number of generic brands and short duration of therapy, further compounding the problem of resistance.^{6,13} Resistant bacteria are no longer only found in hospitals; they have been isolated in the general population, which makes containment and treatment difficult and expensive. There is a need for new inhibitors, new targets and new strategies to combat bacterial infections. Recently, there has been a push in the medical community, and by governments, to bring this to the forefront and encourage research in the field. The 10×20 initiative is a call to all researchers, health care providers and regulatory bodies to work together to develop and commit to a solution to this worldwide problem.¹⁴

1.3. The Shikimic Acid Biosynthetic Pathway

The shikimate pathway is responsible for the biosynthesis of the aromatic amino acids tyrosine (Tyr), tryptophan (Trp) and phenylalanine (Phe) in all bacteria, plants and some fungi.¹⁵ This pathway does not exist in mammals, and, as such, is an attractive target for antibiotic drug therapy. The first step of the pathway is the irreversible¹⁶ condensation of phosphoenolpyruvate (PEP) and erythrose 4-phosphate (E4P) to form 3-deoxy-D-*arabino*-2-heptulosonate-7-

phosphate (DAHP) and inorganic phosphate (P_i) (Figure 1.1).¹⁷ The reaction is catalyzed by DAHP synthase (DAHPS).

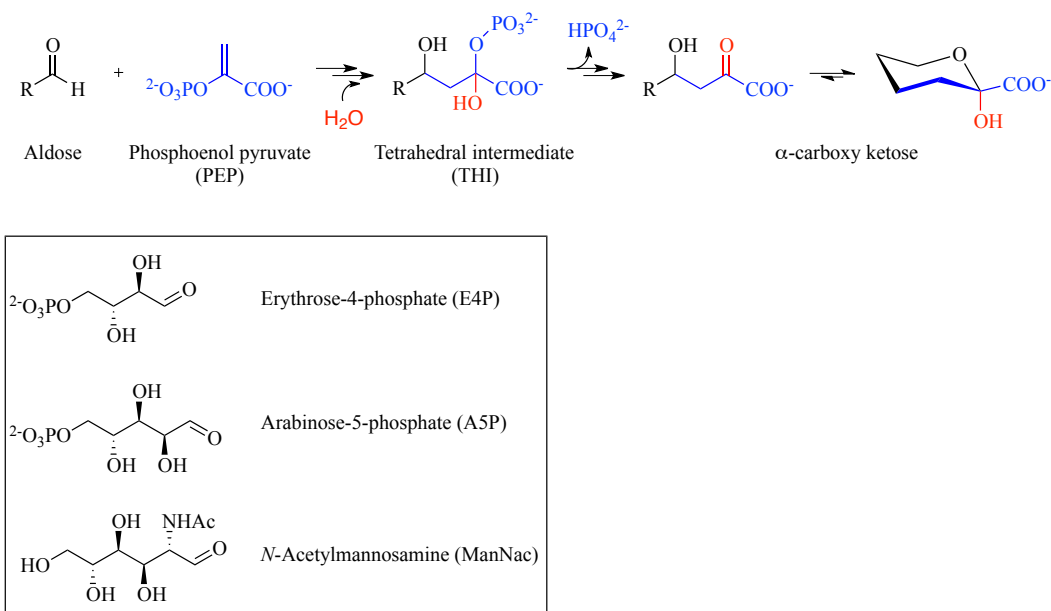


Figure 1.1: General reaction of α -carboxyketose synthases.

DAHPS catalyzes the reaction of PEP with E4P to form DAHP. The related enzyme KDO8P synthase uses arabinose 5-phosphate as the aldose substrate to form the eight carbon sugar KDO8P (see below), while NeuB uses *N*-acetylmannosamine to form *N*-acetylneuraminic acid (see below).

The product DAHP is converted through several intermediates to chorismate, the branch point precursor to aromatic amino acids synthesis (Figure 1.2). In plants, some fungi, and yeasts including *Neurospora crassa*, *Aspergillus nidulans*, *Saccharomyces cerevisiae* and *Schizosaccharomyces pombe*, steps 2 through 6 are catalyzed by a pentafunctional polypeptide known as the arom protein. The functional domains of arom and the five separable enzymes in the shikimate pathway are homologous, so it is believed that *arom* is a product of fusion of separate genes.^{15,18} In addition to aromatic amino acid biosynthesis, the pathway has branch points from which important secondary metabolites are

formed, including folates, flavanoids, cinnamate and lignans.¹⁹ For example, DAHP and 3-dehydroquinate are branch points from which 3-hydroxy-5-aminobenzoate or 3-aminobenzoate are synthesized. The aminobenzoates are precursors to antibacterial and antiviral compounds.¹⁸ Inhibition of the pathway would effectively disrupt protein biosynthesis and secondary metabolite synthesis. DAHPS is an excellent target for antibiotics because it is the first committed step in the pathway, and, as such, controls all carbon flow through the pathway. Inhibition of DAHPS inhibits the shikimic acid pathway, including all downstream pathways, and would lead to inhibition of cell growth.²⁰ Inhibition of amino acid biosynthesis has been successfully utilized with glyphosphate, a broad spectrum herbicide which inhibits 5-enolpyruvylshikimic acid-3-phosphate (EPSP) synthase, the sixth enzyme of the shikimate pathway.²¹ EPSP synthase-deficient bacteria are shikimate auxotrophs and avirulent, and can be used in live attenuated vaccination.^{22,23} Currently there are no antibiotics that target DAHPS.

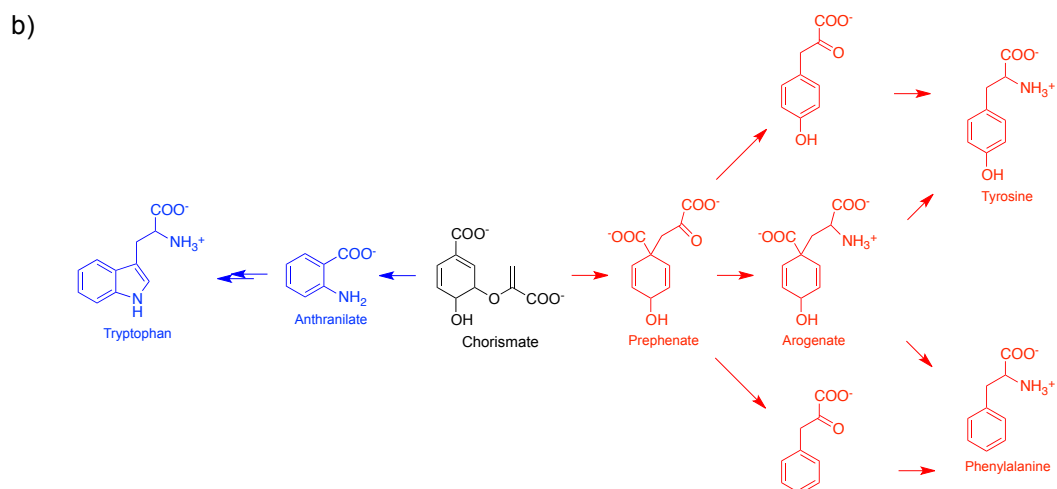
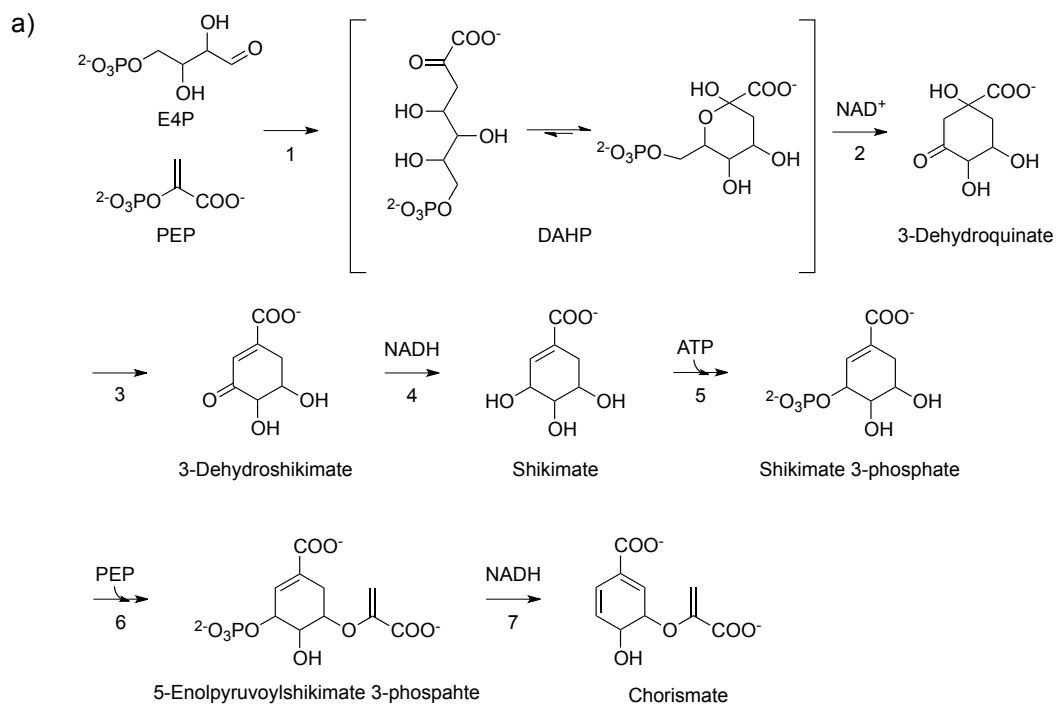


Figure 1.2: Shikimate Pathway.

(a) Main branch of the shikimate Pathway (black) starts with the condensation of PEP and E4P and finishes at chorismate. (b) Biosynthesis of tyrosine (blue) phenylalanine (red) and tryptophan (red) from chorismate.

1.4. DAHPS

There are two classes of DAHPS. Class I DAHPSs have monomeric (subunit) masses of approximately 40 kDa, and are further divided into two subgroups, I α and I β . Class I α enzymes are comprised of those DAHPSs that are similar to the *E. coli* DAHPS, with molecular masses of \approx 40 kDa. Class I β DAHPSs have higher sequence identity to 3-deoxy-D-manno-2-octulosonate-8-phosphate synthase (KDO8PS, a homologous enzyme involved in lipopolysaccharide biosynthesis) than to the Class I α DAHPSs. Class II DAHPSs initially encompassed DAHPSs found in plants; however, they have recently been expanded to include microbial enzymes that are more similar to plant DAHPSs than Class I. Class II enzymes are the larger enzymes, with monomeric molecular mass of $>$ 50 kDa.²⁴⁻³¹

Because it catalyzes the first step in the shikimate pathway, DAHPS controls carbon flow through the pathway. In bacteria there are two known regulatory mechanisms of DAHPS activity, namely allosteric feedback regulation, and suppression of protein expression. Allosteric regulation of DAHPS activity is by different products or intermediates of the shikimate pathway. Class I α enzymes are regulated by the aromatic amino acids. *E. coli* expresses three DAHPS isozymes, one each regulated by tyrosine, tryptophan, and phenylalanine.³²⁻³⁶ *S. cerevisiae* expresses two isozymes, regulated by tyrosine and phenylalanine.^{24,26,28} Class I β enzymes can contain an extra regulatory domain, and they show a more diverse regulation pattern. *Lysobacter*

enzymogenes, *Xanthomonas campestris* and *P. aeruginosa* DAHPSs are regulated by either tryptophan or chorismate.^{37,38} *Mycobacterium tuberculosis* DAHPS, on the other hand, is regulated by combinations of at least two of the aromatic amino acids; no one amino acid alone inhibits the enzyme.³⁹ *Bacillus subtilis* DAHPS is bifunctional, with both DAHPS and chorismate mutase domains. It is regulated by the shikimate pathway intermediates prephenate and chorismate. Due to its low activity the chorismate domain is believed to be acquired primarily for regulation and not for bifunctional activity.^{40,41} In contrast, *Oceanospirillum minutulum* expresses one isozyme which does not appear to be feedback regulated.³⁷ Regulation of DAHPS transcription has been identified in bacteria. In *E. coli* DAHPS employs the *tyrR* and *trpR* repression systems which respond to tyrosine and tryptophan levels.⁴²⁻⁴⁵

Plants contain separate cytoplasmic and chloroplast DAHPSs.⁴⁶ Chloroplast-isolated DAHPS is inhibited by argonate⁴⁷ by a "sequential feedback mechanism" in which the enzymes that use argonate as a substrate are feedback inhibited by their ultimate products (Tyr and Phe), which in turn causes argonate to accumulate, leading to DAHPS inhibition. Unlike bacterial DAHPS, plant DAHPS have not been shown to be inhibited by the aromatic amino acid end products; rather tryptophan has been seen to activate it.^{35,48} Primary regulation appears to be at the expression level.⁴⁹

DAHPS is dependent on a divalent metal cation for activity. A diverse set of divalent metals have been shown to activate DAHPS in vitro, including Mn^{2+} ,

Fe^{2+} , Co^{2+} , Ca^{2+} , Cu^{2+} , Ni^{2+} , Zn^{2+} and Cd^{2+} .³⁵ It is not clear what the preferred metal is in vivo; Fe^{2+} , Zn^{2+} and Cu^{2+} have been suggested.^{35,50,51} Catalytically, the metal ion is believed to both coordinate and orient the C1 carbonyl oxygen of E4P for catalysis, and it serves as an electrophile to polarize the C1 carbonyl of E4P for nucleophilic attack by C3 of PEP.^{52,53}

DAHPSs assume a TIM barrel $(\alpha/\beta)_8$ fold (Figure 1.3b), and are oligomeric (dimers or tetramers) in solution.^{39,52,54} *E. coli* Phe-regulated DAHPS is a homotetramer. Subunits A & B form a "tight" dimer with an extensive interface between the subunits; similarly with subunits C & D. The AB and CD tight dimers have a "loose" interface with each other to form a dimer of dimers (Figure 1.3a).

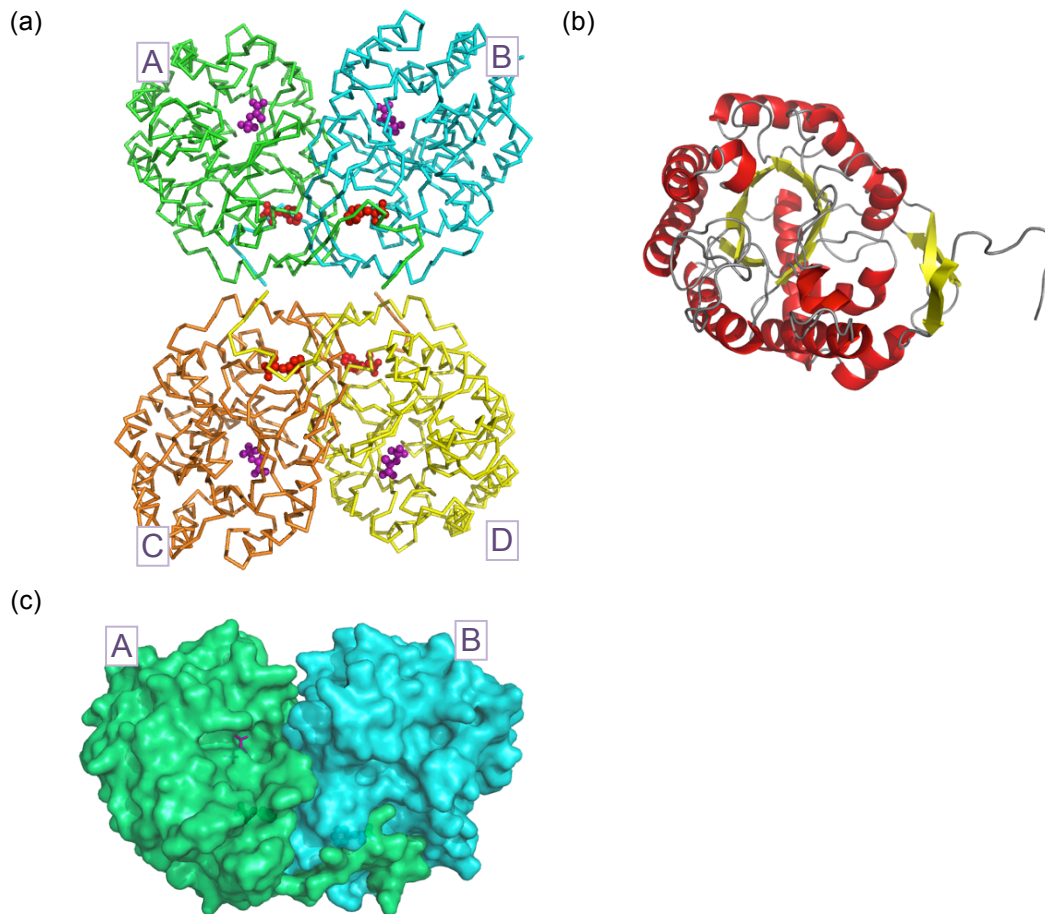


Figure 1.3: Crystal structure of *E. coli* phenylalanine-regulated DAHPS.

(a) Ribbon diagram of DAHPS from PDB 1KFL.⁵⁵ Each subunit is labelled. Extensive contact is made between the tight dimers AB and CD. The tetramer is formed by the association of the tight dimers to form a dimer of dimers. The substrate PEP is shown in purple, and the allosteric inhibitor, phenylalanine is in red. (b) Depiction of the DAHPS supersecondary structure, an $(\alpha/\beta)_8$ fold. α -Helices are shown in red, β -strands in yellow, and loops in grey. (c) Subunits A and B showing the overlap of the *N*-terminus from subunit A wrapping around subunit B, and capping the phenylalanine binding site.

Each monomer contains a complete active site. The essential divalent metal ion is coordinated by residues C61, H268, E302, D326 and a water molecule (Figure 1.4). The carboxylate of PEP also makes contact with the metal ion. PEP binds deep in the pocket, coordinated by Arg and Lys residues.

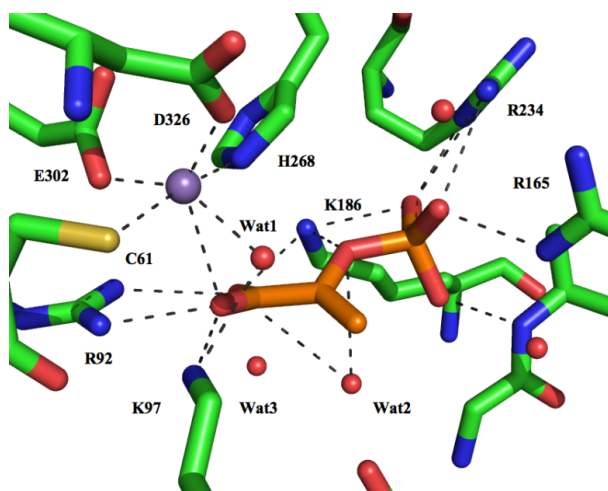


Figure 1.4: Coordination of PEP and Mn^{2+} in DAHPS active site.

Crystal structure of Mn^{2+} (purple) and PEP (orange) bound to DAHPS (green). PEP is anchored in the active site through interaction with its phosphate and carboxylate moiety and Lys and Arg residue of the enzyme. The carboxylate of PEP makes further contact with the metal ion and two water molecules (Wat2, Wat3). Wat2 is in close proximity to the bridging oxygen of PEP's phosphate. Wat2 is believed to be the water molecule that attacks C2 of the presumed oxacarbenium ion intermediate, leading to the tetrahedral intermediate (THI). Mn^{2+} assumes a distorted octahedral geometry, with C61 and H268 as the axial ligands. The equatorial ligands are D326, E302, the PEP carboxylate, and Wat1 (the presumed binding site of the C1 carbonyl oxygen of E4P). This figure was made from PDB file 1N8F.

E4P has not been co-crystallized with the enzyme, but its binding site has been inferred from sulfate ion binding in the presumed E4P-binding area.^{4,54} The phenylalanine-binding site is located near the tight dimer interface, along the dimer-dimer interface. Its binding site also includes the *N*-terminus from the adjacent dimer that caps the binding site (Figure 1.3c).⁵⁵

1.5. DAHPS Homologues

DAHPS belongs to the α -carboxyketose synthase superfamily of enzymes that includes KDO8PS and sialic acid synthase (NeuB). All members within this family catalyze a similar aldol-like condensation between PEP and their aldose sugar substrates (erythrose 4-phosphate, arabinose 5-phosphate, and *N*-

acetylmannosamine, respectively) to form an α -carboxyketose and inorganic phosphate (P_i) (Figure 1.1).^{16,56,57} All are considered potential targets for drug development, as none occur in mammals and all are essential for pathogenicity.

1.5.1. KDO8P Synthase

KDO8PS is involved in lipopolysaccharide (LPS) biosynthesis in Gram-negative bacteria.^{8,58} It catalyzes the condensation of arabinose 5-phosphate (A5P) with PEP to form 3-deoxy-D-manno-2-octulosonate-8-phosphate (KDO8P) and P_i .⁵⁶ KDO8P is subsequently dephosphorylated to form 3-deoxy-D-manno-oct-2-ulosonic acid (KDO), which is then activated by formation of the cytosine nucleotide derivative, CMP-KDO.⁵⁹ CMP-KDO serves as the KDO source for LPS biosynthesis. LPS is a glycolipid found on the outer leaflet of the outer membrane of Gram-negative bacteria (Figure 1.5). LPS is vital for cell growth and bacterial pathogenicity.⁵⁸ LPS is also essential in maintaining the integrity of the outer membrane; LPS deficiency increases organisms' susceptibility to antibiotics.⁶⁰ LPS consists of three components: a lipid layer (Lipid A) embedded in the membrane, a nonrepeating oligosaccharide core, and a polysaccharide layer (*O*-antigen) that extends away from the membrane.⁶¹ The oligosaccharide core links lipid A and the *O*-antigen. The oligosaccharide core's composition varies, but almost all species of Gram-negative bacteria have two KDO subunits covalently attached to Lipid A. The KDO₂:Lipid A unit forms the minimum requirement for cell growth. Without the KDO subunits the complete synthesis of

the Lipid A does not occur.^{15,62} Inhibition of the KDO:Lipid A formation inhibits cell growth and increases the bacterial susceptibility to antibiotics and host defences.⁶³ A mutation in KDO8PS that causes a temperature dependent increase in the K_M of A5P leads to the inhibition of cell growth.^{64,65} Recent evidence suggest that inhibition of KDO8PS by small molecules leads to cell growth inhibition in vivo.²⁰

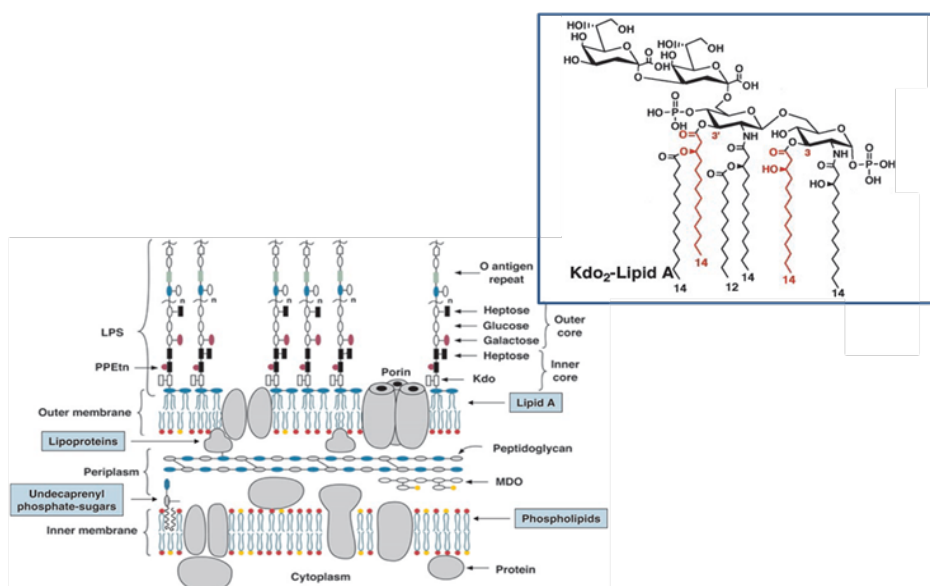


Figure 1.5: Lipopolysaccharide (LPS) of Gram negative bacteria.

Image taken from Raetz et al.⁶¹

KDO8PS and DAHPS are homologous,³¹ but key functional differences exist. The majority of DAHPSs are regulated by shikimate pathway intermediates, but no such regulation exists for KDO8PSs. All known DAHPSs require divalent metal for catalytic activity, while both metal-dependent and -independent KDO8PSs exist.²⁹ Mutation of a metal-coordinating Cys residue to Asn in a metal-dependent KDO8PS abolished the metal dependence

with a minimal effect on k_{cat} . Similarly, an Asn-to-Cys mutation in a metal-independent KDO8PS introduced metal dependence.⁶⁶ Although KDO8PS and DAHPS have low sequence similarity, crystal structures show that they have the same TIM barrel $(\alpha/\beta)_8$ supersecondary structure.

1.5.2. NeuB

NeuB catalyzes the synthesis of *N*-acetylneuraminic acid (NeuNAc) from PEP and *N*-acetylmannosamine (ManNAc).⁵⁷ NeuNAc is a derivative of neuraminic acid, the simplest form of the sialic acids. Sialic acids occur as *N*- or *O*- substituted derivatives of neuraminic acid, and are usually found in glycoconjugates on eukaryotic cell surfaces. Their functions include cellular recognition and immune response.⁶⁷ Certain bacteria, including neuroinvasive *E. coli*, *Campylobacter jejuni* and *Neisseria meningitidis* have NeuNAc residues on their cell surface to mimic the host cell and evade the immune system. Although NeuNAc is synthesized in mammalian cells, the synthetic pathway is different from bacteria.⁶⁸ Bacteria use NeuB to synthesize NeuNAc from ManNAc directly. In contrast, mammals first phosphorylate ManNAc at the 6 position, from which NeuNAc-9-phosphate is synthesized by NeuNAc-9-phosphate synthase, followed by dephosphorylation to NeuNAc. This difference allows for the possibility of selective inhibition of bacterial versus mammalian NeuNAc synthesis.

There is evidence in the literature for NeuB existing both as a dimer of dimers⁶⁹ and as a homodimer,^{70,71} but the consensus favours the latter. The monomer structure is composed of two domains. The active site is contained within the *N*-terminal domain which adopts the familiar TIM barrel (α/β)₈ supersecondary structure. The *N*-terminal domain is connected through a 10 amino acid linker to the *C*-terminal domain, which has high sequence similarity to fish type III antifreeze protein.⁷² The *C*-terminal domain of the first monomer overlaps the *N*-terminal domain of the second monomer (Figure 1.6). This overlap is essential to creating a complete active site, as the *N*-terminal domain, which contains the active site, requires three residues (R314, T285, F288) from the *C*-terminal domain of the adjacent monomer to form the complete active site. The *C*-terminal domain also serves to close the active site once substrates are bound.

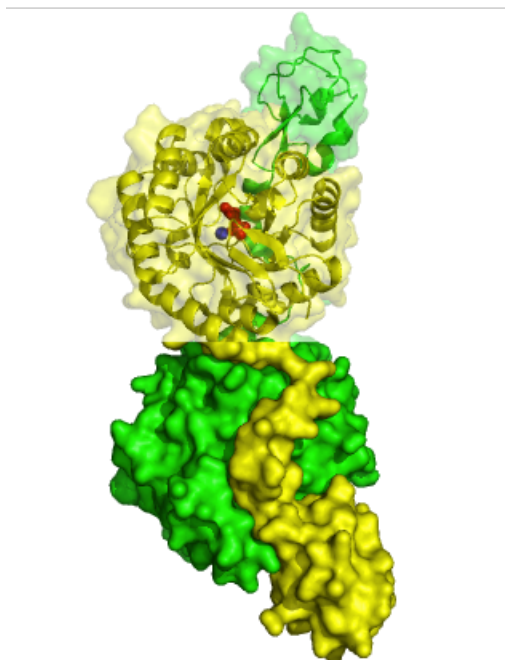


Figure 1.6: NeuB crystal structure.

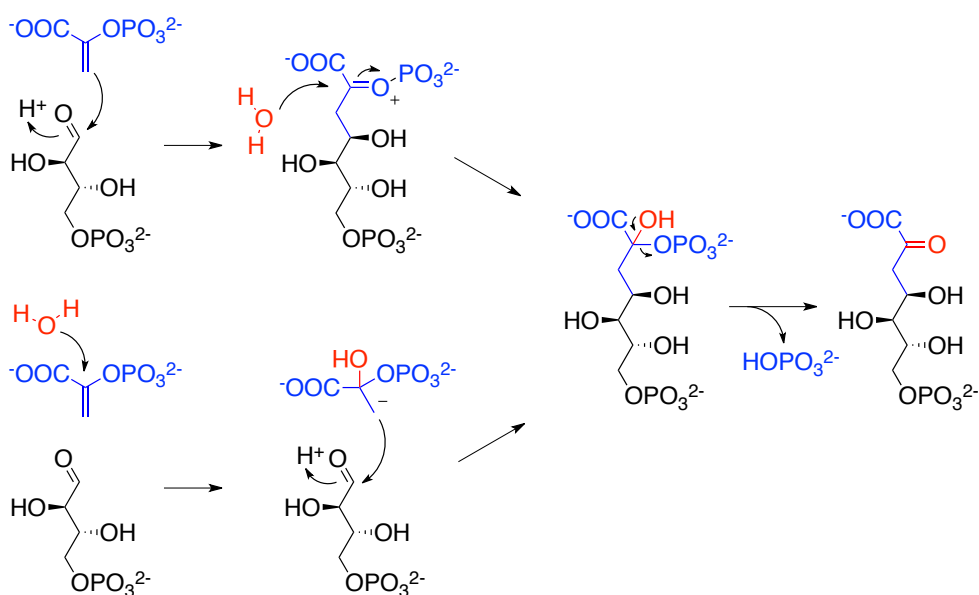
Homodimeric structure of *N. meningitidis* NeuB, from PDB: 1XUZ.⁷⁰ The C-terminal "tail" domain of one monomer overlays the active site pocket of the adjacent monomer's N-terminal domain to form the complete active site. Mn^{2+} and PEP in the yellow monomer's N-terminal domain are colored purple and red respectively. The asymmetric unit of 1XUZ is a monomer; the homodimer was generated by applying the symmetry operator to the monomer structure.

1.6. Catalysis

The precise catalytic mechanisms of the α -carboxyketoses is under debate; two main models have been proposed (Figure 1.7). In the first proposed mechanism (Figure 1.7, Path A), C3 of PEP performs nucleophilic attack on the carbonyl carbon of the aldose substrate, forming a oxacarbenium ion intermediate.^{35,73} Nucleophilic attack by water then forms a tetrahedral intermediate (THI).^{74,75} The second proposed catalytic mechanism involves nucleophilic attack by water or hydroxide on C2 of PEP to form a carbanion intermediate, which then attacks the carbonyl carbon of the aldose⁷⁶⁻⁷⁸ (Figure 1.7,

Path B). Given the recent evidence that nucleophilic attack on C2 of PEP without prior activation of C3 is essentially impossible, this mechanism should be considered unlikely.⁷⁹ Both pathways converge at the THI, and the proposed mechanisms for THI breakdown would be the same. Concerted reaction mechanisms are also possible, in which discrete cationic or anionic intermediates are not formed. Recent computational analysis of the KDO8PS reaction postulated that the stepwise mechanisms above do not represent the lowest energy pathway.⁸⁰ Rather, it found the most favourable transition state had formation of the C-C bond between PEP and A5P occurring well in advance of C-O bond formation from water addition. The computational transition state was on the border between a stepwise and concerted mechanism, but in either case, the transition state would have significant oxacarbenium ion character.

PATH A



PATH B

Figure 1.7: Proposed mechanism of DAHPS.

The kinetic mechanism is ordered with respect to substrate binding, where PEP binds before the aldose sugar in both DAHPS and KDO8PS.^{34,81} The order of substrate binding is not known for NeuB. The reaction is stereospecific; with DAHPS and KDO8PS, the *si* face of PEP attacks the *re* face of the aldehyde functionality.^{16,78,82-84} In NeuB, the *si* face of PEP attacks the *si* face of ManNAc's aldehyde group.⁸⁵ Inorganic phosphate departure occurs through C-O bond cleavage.^{16,78,84}

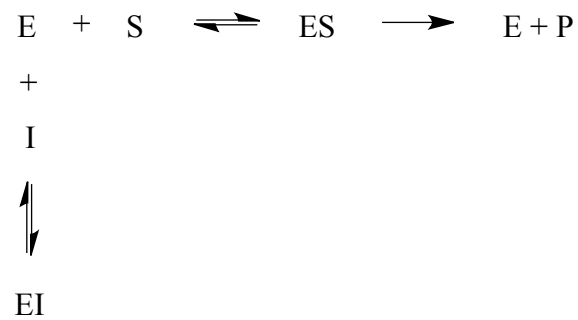
1.7. Inhibitors

Inhibitors can serve as probes of enzyme function in addition to any potential clinical use. Almost half of all drugs, 47%, are enzyme inhibitors⁸⁶ including those targeting HIV protease and reverse transcriptase (AIDS), HMG-CoA reductase (hypercholesterolemia), angiotensin-converting enzyme (hypertension), and cyclooxygenases (inflammation, pain).⁸⁷

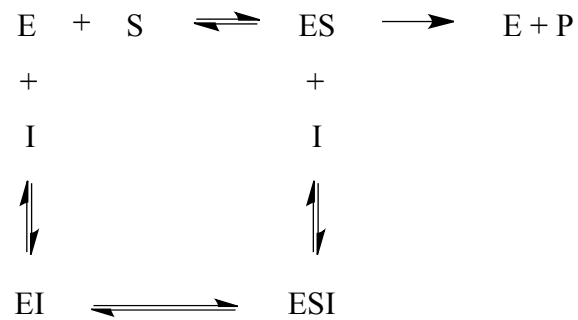
There are a number of strategies that can be utilized when designing inhibitors, with differing kinetic outcomes.⁸⁸ Covalent inhibitors permanently inactivate enzymes by chemically modifying them, whereas reversible inhibitors non-covalently modulate enzyme activity. Competitive reversible inhibitors prevent substrate binding. This is generally because the inhibitor occupies the substrate binding site, but competitive inhibition simply implies that inhibitor and substrate binding are mutually exclusive. Because binding is competitive, inhibition can be relieved by increased substrate concentrations. Noncompetitive reversible inhibitors decrease enzyme activity but do not compete with substrates

for binding, and so are insensitive to substrate concentration. Uncompetitive inhibitors bind specifically to the E•S complex (Figure 1.8).

Competitive inhibitor



Noncompetitive inhibitor



Uncompetitive inhibitor

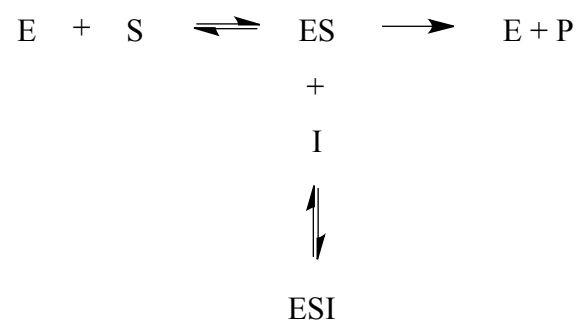


Figure 1.8: Modes of inhibition by reversible inhibitors.

E = enzyme, S = substrate(s), I = inhibitor, P = product(s).

Given its multiple substrates and allosteric inhibition sites, DAHPS has multiple possible avenues for inhibition. DAHPSs from different organisms use different allosteric inhibitors, including different isozymes within some species, so there will not be a universal allosteric inhibitor for all DAHPSs. Competitive inhibitors, on the other hand, will be effective against all DAHPS, can be useful in the study of enzyme mechanisms, and can be potential drug candidates.

Enzymes derive their catalytic power by binding to and stabilizing transition states, and to a lesser extent, high energy unstable intermediates. Enzymes provide rate enhancement of 10^7 - to 10^{19} -fold compared to the corresponding noncatalyzed reactions.⁸⁹ Enzymes accomplish this in a number of ways, including general acid/base catalysis, covalent catalysis, metal ion catalysis, ground state destabilization, high local concentration and orientation of reactive moieties.⁹⁰ To achieve this rate enhancement, the enzyme binds the transition state with higher affinity than the substrate, with K_d values on the order of 10^{-8} to 10^{-23} M. In this context, transition state mimics, that is, inhibitors that are designed to mimic the structural features of the highest energetic point in the reaction coordinate, having the potential to be bound with dissociation constants as low as 10^{-23} M.⁸⁹ In reality, stable molecules cannot perfectly mimic inherently unstable transition states, so even the best transition state mimics capture only a small fraction of the theoretically available binding energy. Due to their short lifetimes ($\approx 10^{-13}$ s), transition state structures are hard to study.⁹¹

The transition states for α -carboxyketose synthesis is not known. Experimental evidence for the THI has been presented by mass spectrometry⁷⁴ and crystallography,⁷⁵ and an oxacarbenium ion intermediate has been proposed (Figure 1.7). The putative oxacarbenium ion, an intermediate with a positive charge resting primarily on the C2 carbon atom,^{91,92} would be less stable than the THI. Oxacarbenium ions have lifetimes in aqueous solution of 10^{-12} to 10^{-10} s;⁹³⁻¹⁰¹ they thus require more stabilization, and therefore stronger binding to the enzyme. Recent computational simulations of the KDO8PS reaction indicate significant oxacarbenium ion character in the transition state, with C-C bond formation proceeding in advance of C-O bond formation, though it did not necessarily indicate formation of a discrete oxacarbenium ion intermediate.⁸⁰ Both intermediates are attractive targets for inhibitor design.

1.8. Slow Binding Inhibitors

Slow binding inhibitors are inhibitors that show time-dependent inhibition, requiring extended incubation of enzyme and inhibitor together to see maximum inhibition.^{87,102} Typically, these inhibitors initially interact weakly with the enzyme, forming a weak EI complex. The enzyme in the EI complex then undergoes isomerization to optimize binding with inhibitor, forming the tightly bound E*I complex (Figure 1.9). The true affinity of this class of inhibitor lies in the E*I complex as k_4 in some cases are measured in days, leading to long residency times in the active site, and high affinity inhibitors.⁸⁷ Recently, increasing residency times has become an explicit goal of inhibitor design.^{103,104} Transition

state mimics are commonly slow binding inhibitors.¹⁰⁵ As enzymes are optimized to initially bind substrates, the enzyme must often isomerize to optimize binding with transition state mimics.¹⁰⁶

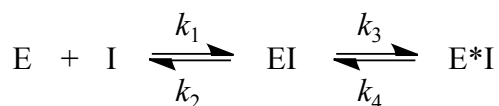


Figure 1.9: Kinetic mechanism for slow binding inhibition.

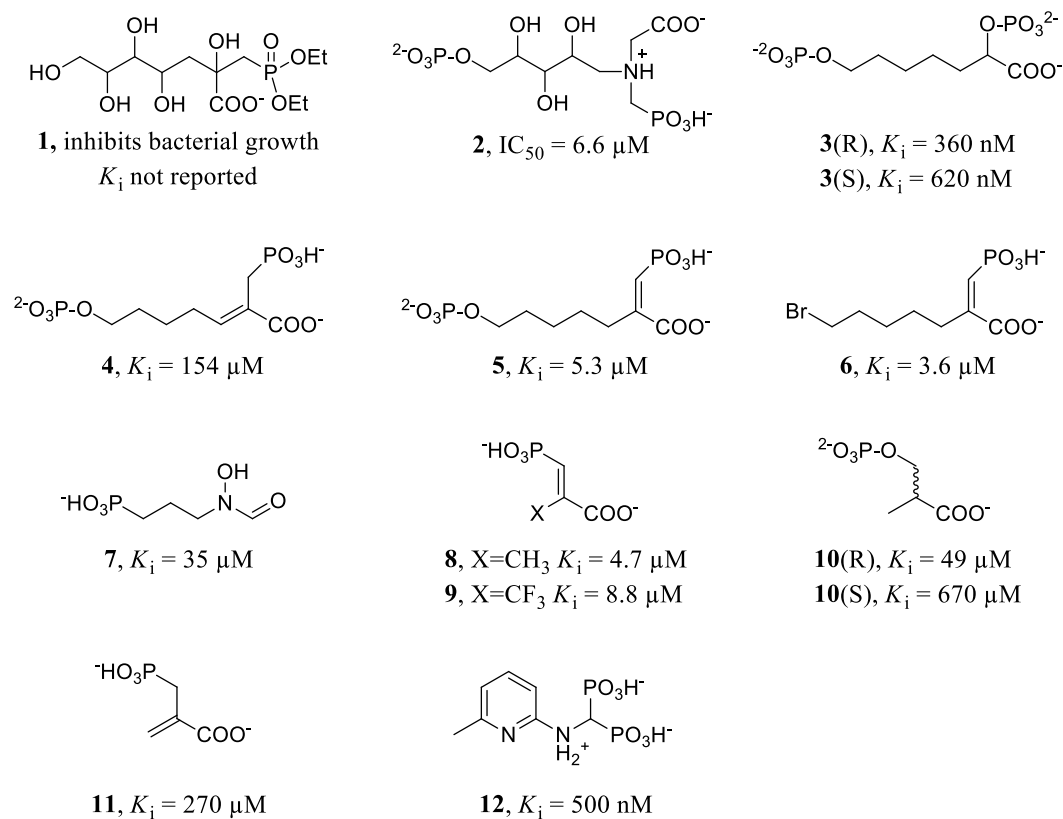
1.9. Cooperativity

DAHPS oxime binding to DAHP displays both negative cooperativity (inhibitor binding to subunit B blocks its binding to subunit A) and positive cooperativity (inhibitor binding to subunit B increases binding to subunit C) (see Chapters 2 and 3). Cooperativity is the communication between subunits in oligomeric enzymes that manifests in K_s (K_i) values, whereby binding of the first substrate (inhibitor) affects the affinity of subsequent ligand molecules binding in the unoccupied sites. Cooperativity can be either positive (binding of one ligand enhances subsequent ligand binding) or negative (binding of one ligand hinders subsequent binding). There are two prominent models of cooperativity in literature, the Monod-Wyman-Changeux (MWC) and Koshland-Némethy-Filmer (KNF) models.^{107,108} The MWC model is a concerted symmetry model in which all subunits exist in the same state. Ligand binding to the first subunit causes it to switch from a low affinity to high affinity state, causes all unoccupied subunits to adopt the same high affinity state.¹⁰⁸ The KNF model is a sequential model in

which ligand binding in the first subunit, affects binding in the second subunits (either positively or negatively), binding of the second substrate molecule then affects binding in the third subunit (either positively or negatively), and so on.¹⁰⁷ Oxygen binding to hemoglobin is a classic example of positive cooperativity.¹⁰⁹ Hemoglobin is a tetramer that fluctuates between two states of high and low O₂ affinity. Upon binding the first O₂ molecule the iron heme undergoes structural changes that is mirrored in all subunits. This conformational change shifts all remaining subunits into the high affinity state, increasing the affinity for O₂, (i.e., $K_{M1}(O_2) > K_{M2}(O_2)$). Alternatively, in some systems, binding of the first ligand increases the K_M for subsequent substrate binding; this is negative cooperativity.¹¹⁰ An extreme example of negative cooperativity is when substrate binding in one site completely inhibits binding in other sites.¹¹¹⁻¹¹³ This gives rise to “half-of-sites reactivity”, that is, in oligomeric proteins catalysis alternates between subunits such that only a fraction of the active sites is active at one time. With purine nucleoside phosphorylation, a homotrimer, only one site is active at a time, with the energy released from one active site during catalysis driving product release in another site.^{114,115}

1.10. DAHPS Inhibitors

A number of DAHPS inhibitors have been reported in literature that try to mimic structural features of the intermediates (Figure 1.10).

DAHPS inhibitors**Figure 1.10: Inhibitors of DAHPS.**

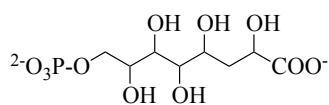
Compound **1** was designed to be a THI analogue.²⁰ Compound **2** was designed to be an oxacarbenium ion intermediate analogue.¹¹⁶ Inhibitors **3** to **6** extend from PEP binding site to E4P's phosphate binding site.^{117,118} Inhibitors **7** to **11** are competitive with respect to PEP.¹¹⁹ Compound **12** was a noncompetitive inhibitor.¹²⁰

Compounds **8** to **11** were designed to target the PEP binding site.¹¹⁹ These compounds mimic the reaction intermediates with respect to the position of C2. PEP analogue **11**, was a poor inhibitor with $K_i = 270 \mu\text{M}$. Compound **10** mimics the sp^3 hybridization of C2 in the THI. The **10(R)** configuration was preferred 5-fold over **10(S)**. It was, however, the vinyl phosphonate (**8**), which mimics the geometry of the presumed oxacarbenium ion intermediate, but lacking the positive charge at C2, that was the most potent inhibitor in the series. Extension of **8** into

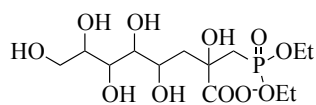
the E4P binding site (**4-7**) did not improve binding affinity.¹¹⁷ Interestingly, it was the THI mimic **3** what was the most potent inhibitor reported. Compound **3**, which is an extension of **10(R)** into the E4P binding site, had a nanomolar K_i . Changing the hybridization of the C2 of PEP from sp^2 (**5**) to sp^3 (**3**) resulted in a < 10-fold decrease in K_i . Compound **1** was designed as a THI mimic. It was active against *Escherichia coli*, *Yersinia enterocolitica*, *Pseudomonas aeruginosa*, *Staphylococcus aureus* and *Bacillus subtilis* cultures, though the K_i value was not reported.²⁰ Removal of the ethyl groups from the phosphate abolished inhibition, presumably because the charged compound was unable to cross the cell membrane. Compound **2** attempted to mimic the cationic character of the oxacarbenium ion with a positively charged tertiary amine group. It showed slow binding inhibition, with $IC_{50} = 6.6 \mu\text{M}$, but K_i was not measured. Compound **7**, a competitive inhibitor with respect to PEP, showed slow binding character, with residual rate at high inhibitor concentrations.¹¹⁹

1.11. KDO8PS/NeuB inhibitors

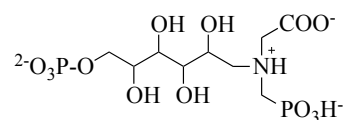
Due to the likely similarity in catalytic mechanisms, similar inhibition strategies should be transferrable from DAHPS to KDO8PS and NeuB.

KDO8P inhibitors

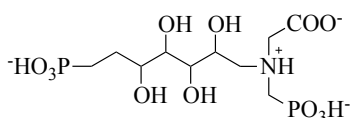
$$K_i = 0.60 \text{ mM}$$

13

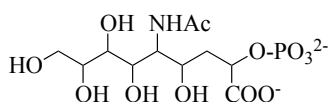
inhibits bacterial growth

14

$$K_i = 400 \text{ nM}$$

15

$$K_i = 50 \text{ }\mu\text{M}$$

16NeuB inhibitors

$$K_i = 3.1 \text{ }\mu\text{M}$$

17**Figure 1.11: Inhibitors of KDO8PS and NeuB.**

As with DAHPS, inhibitors of KDO8PS and NeuB that mimic reaction intermediates were shown to be inhibitors. For KDO8PS, reduced KDO8P (**13**), with a hydroxyl instead of keto group at C2 had $K_i = 0.6 \text{ mM}$.¹²¹ Compound **14** inhibited *Escherichia coli*, *Yersinia enterocolitica* and *Pseudomonas aeruginosa* growth in culture, presumably by inhibiting KDO8PS.²⁰ The oxacarbenium ion mimic **15** was a slow binding inhibitor with $K_i = 400 \text{ nM}$,¹²¹ but had no activity in cultures.¹²² The lack of activity in culture may have been due to phosphate cleavage *in vivo*, so the noncleavable compound **16** was assayed. The K_i was increased 10-fold and it was not active against wild-type *E. coli K12* or *E. coli*

mutant SM101,19a R477-10,19b, nor D22 cultures.¹²² THI mimic **17** had a similar low micromolar K_i against NeuB.¹²³

As is evident from the reported inhibitors, catalytic similarities in this family of enzymes means that similar inhibition strategies can be utilized for all three enzymes.

1.12. Oxime Inhibitors

Previous work in the lab found that NeuNAc oxime (**18**) (Figure 1.12) was a potent, but very slow binding, inhibitor of NeuB, with a K_i of 1.6 pM, but $t_{1/2}$ = 2.5 h for inhibitor binding.^{124,125} The oxime moiety is not a tetrahedral intermediate nor is it a true oxacarbenium ion intermediate. It mimics the sp^2 hybridization of the oxacarbenium ion intermediate but lacks the positive charge. Bulk is not added to the compound with respect to the intermediates, and should utilize all of same enzyme-ligand contacts outside of the oxime group itself.

1.13. Object of Research

The oxime moiety represents a new motif for inhibitors of α -carboxyketose synthases. Due to the structural and catalytic similarities within α -carboxyketose synthases family, an inhibitory motif against one of the enzymes might be expected to translate into inhibition of all members of the family. As NeuNAc oxime is a potent inhibitor of NeuB, we hypothesized that its DAHP equivalent (**19**) (Figure 1.12) could be similarly potent against DAHPS. In this work, we describe the characterization of the inhibition of *E. coli* phenylalanine-

regulated DAHPS by DAHPS oxime. Three main methodologies were utilized in this study. Steady state kinetic assays were used to characterize DAHP oxime inhibition. X-ray crystallography was employed to study the binding of DAHP oxime with DAHPS. Finally, we attempted to study changes in enzyme dynamics upon inhibitor binding through NMR and hydrogen/deuterium (H/D) exchange via mass spectrometry.

We show that DAHP oxime is a potent, slow-binding inhibitor. The binding of DAHPS oxime to DAHPS revealed a new 2-fold symmetry in DAHPS's active sites in the tetramer that had not been observed previously.

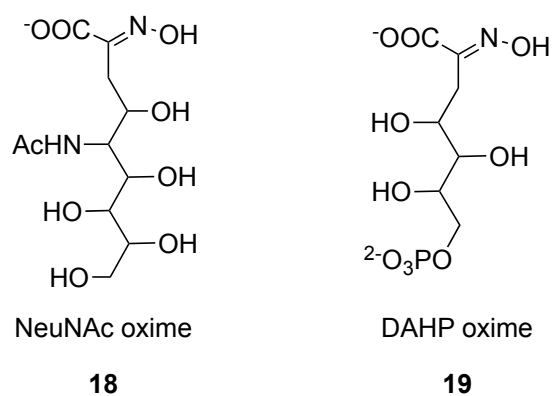


Figure 1.12: Oxime inhibitors of NeuB and DAHPS.

Chapter 2 - Kinetics

2.1. Introduction

NeuNAc oxime is a potent slow-binding inhibitor of NeuB.^{124,125} Inhibition requires 20 h preincubation to achieve maximal binding, with $K_i = 1.6$ pM.¹²⁴ Inhibition is incomplete; that is, even at high inhibitor concentrations, a residual rate persists. Due to the structural and mechanistic similarities between NeuB and DAHPS, DAHP oxime was expected to be an inhibitor of DAHPS.

Here we describe the purification and characterization of the phenylalanine-regulated *N*-terminally His₆-tagged DAHPS (DAHPS_{H6}) from *E. coli*.

2.2. Materials and Methods

2.2.1. DAHP Synthase (Phe) Purification

The pCA24N expression plasmid for *E. coli* DAHP synthase (Phe) (also called *aroG*) with an *N*-terminal His₆ tag (DAHPS_{H6}) was a gift from Dr. Eric Brown (McMaster University). The vector *aroG*:pCA24N was transformed into *E. coli* BL21*(DE3) cells and plated on a lysogeny broth (LB)/agar plate containing 10 µg/mL chloramphenicol. Plates were incubated at 37 °C for 16 h. A single colony from the overnight plate was inoculated into 50 mL LB medium with 10 µg/mL chloramphenicol and cultured overnight at 37°C. The 50 mL overnight culture was subcultured into 1 L LB with 10 µg/mL chloramphenicol

and grown at 37 °C to $OD_{600} = 0.6$. DAHPS_{H6} expression was induced with 0.3 mM isopropyl β -D-1-thiogalactopyranoside (IPTG) at 37 °C for 4 h. Cells were harvested by centrifugation at $8000 \times g$ for 20 min. All samples were kept at 4 °C from this point forward. Cells were re-suspended in 15 mL of buffer A (50 mM Tris-Cl, pH 7.5, 150 mM NaCl, 50 mM imidazole, 1 mM phenylmethylsulfonyl fluoride). Cells were lysed by passage through EmulsiFlex-C5 High Pressure Homogenizer at 10,000 psi. Cell debris was removed by centrifugation for 30 min at $10,000 \times g$. The supernatant was loaded onto 1 mL HiTrap chelating column (GE Healthcare) that was charged by running 5 column volumes of 100 mM nickel sulfate. DAHPS_{H6} was eluted with buffer B (50 mM Tris-Cl, pH 7.5, 150 mM NaCl, 500 mM imidazole). Based on SDS/PAGE electrophoresis, the protein was purified to homogeneity. The purified protein was then buffer exchanged into storage buffer (50 mM Tris-Cl, pH 7.5, 100 mM KCl, 1 mM TECP and 10% (v/v) glycerol). Protein concentration was determined from A_{280} , using $\epsilon_{280} = 34\,166\text{ M}^{-1}\text{cm}^{-1}$, as determined by the Edelhoch method.^{126,127} The purified enzyme was flash frozen in ethanol/dry ice bath and stored at -80°C.

2.2.2. Steady State Kinetics

All initial velocities (v_0) were measured using by following inorganic phosphate (P_i) production using the Malachite Green/ammonium molybdate colorimetric assay for P_i .¹²⁸ All buffers and substrates, except $MnCl_2$, were

treated with Chelex 100 (Bio-Rad Laboratories, Inc.) prior to use, to remove residual divalent metal ions.

Steady state kinetic parameters were determined by holding two substrates' concentrations fixed, and varying the third. The metal ion is, strictly speaking, not a substrate, as it is not chemically changed by the enzyme; however, it is treated as a substrate in the Michaelis-Menten equation. The fixed concentrations were, 250 μM E4P, 250 μM PEP and 250 μM MnCl_2 . The variable concentrations were 0 to 700 μM E4P, 0 to 1 mM PEP and 0 to 1 mM MnCl_2 . Reactions were typically run with 10 or 25 nM DAHPS_{H6} in reaction buffer at 25 °C. Reaction buffer was 50 mM K-HEPES, pH 7.0, 100 mM KCl and 0.1 mM tris(2-carboxyethyl)phosphine (TCEP). The steady state kinetic parameters were determined by fitting the initial velocity data to the equation for a ternary ordered sequential kinetic mechanism (eq. **2.1**):

$$\frac{v_0}{[E]_0} = \frac{k_{cat} \left[\frac{[A][B][C]}{K_A K_B K_C} \right]}{1 + \frac{[A]}{K_A} + \frac{[A][B]}{K_A K_B} + \frac{[A][B][C]}{K_A K_B K_C}} \quad (2.1),$$

where [A], [B] and [C] are the concentrations of the substrates Mn^{2+} , PEP, and E4P respectively, and the corresponding Michaelis constants (K_M) are K_A , K_B and K_C .

Equation **2.1** was rearranged to allow k_{cat}/K_M values to be fitted directly, for example:

$$\frac{v_0}{[E]_0} = \frac{\left(\frac{k_{cat}}{K_M}\right)_A \left[\frac{[A][B][C]}{K_B K_C}\right]}{1 + \frac{[A]}{K_A} + \frac{[A][B]}{K_A K_B} + \frac{[A][B][C]}{K_A K_B K_C}} \quad (2.1a),$$

with $(k_{cat}/K_M)_A$ fitted as a single parameter, or to fit $k_{cat}/K_A K_B K_C$ directly as a single parameter:

$$\frac{v_0}{[E]_0} = \frac{\left(\frac{k_{cat}}{K_A K_B K_C}\right) [A][B][C]}{1 + \frac{[A]}{K_A} + \frac{[A][B]}{K_A K_B} + \frac{[A][B][C]}{K_A K_B K_C}} \quad (2.1b).$$

Initial velocities were also fitted to the single substrate Michaelis-Menten equation, in order to compare with kinetic constants reported in the literature:

$$\frac{v_0}{[E]_0} = \frac{k_{cat} [S]}{[S] + K_M} \quad (2.2)$$

2.2.3. E4P synthesis

E4P was synthesized by the previously described oxidative degradation of glucose 6-phosphate to erythrose 4-phosphate using lead tetraacetate.¹²⁹ Briefly, glucose 6-phosphate (0.3 mmol) prepared in 75 mL of acetic acid containing 0.3 mmol of H₂SO₄ was titrated with 0.5 mmol lead tetraacetate prepared in 12 mL of acetic acid with 0.5 mmol H₂SO₄. The solution was filtered through a Celite filter and concentrated under vacuum to a volume of 10mL. The Celite was washed with 150 mL of water, which was added to the concentrate, and

concentration continued to 10mL. An additional 150 mL of water was added to the concentrate, and concentration continued to 10mL. The sample was purified on a 5 mL Q-Sepharose column using the conditions outlined above. The collected E4P was run through 5 mL SP-Sepharose (GE Healthcare) cation exchange column charged with HCl to remove Pb^{2+} , using ddH₂O to elute the E4P. E4P was lyophilized to a volume of 5 to 10 mL and stored at -20°C.

2.2.4. DAHP Oxime Synthesis

E4P (4 mM), 4.25 mM PEP, 10 μ M MnCl₂ and 300 nM DAHPS_{H6} in 10 mM K-HEPES, pH 7.0 were incubated at room temperature for 1 h to synthesize DAHP. The reaction was monitored by the Malachite Green/ammonium molybdate assay for P_i, and by HPLC chromatography at 230 nm for loss of PEP. A 5 mL Q-Sepharose (GE Healthcare) anion exchange column was used to purify DAHP, with a linear gradient of 0.1 to 0.8 M ammonium formate in 10 mM ammonium bicarbonate, pH 6.2, over 30 min at 1 ml/min. Elution times were: E4P, 16 min; DAHP, 24 min; PEP, 28 min. Hydroxylamine hydrochloride (25 mM) was added to the DAHP synthesis mixture, and the pH was adjusted to pH 5.5 to start DAHP oxime synthesis. The synthesis was carried out over 24 h at room temperature. DAHP oxime was purified by HPLC chromatography on a 5 mL Q-Sepharose column under the same conditions as DAHP, with DAHP oxime eluting at 24 min. The salts were removed by lyophilisation. The identity

of DAHP oxime was confirmed by NMR spectroscopy and mass spectrometry (see Appendix).

2.2.5. Activation of DAHPS_{H6} by Various Metals

Rate constants of DAHPS_{H6} with various divalent metal cofactors were determined by measuring initial rates of DAHPS_{H6} catalysis with FeCl₂, CaCl₂, NiSO₄, ZnCl₂, MgCl₂, MnCl₂ and CoCl₂. The reaction mixtures contained 0.1 mg/mL BSA, 1mM DTT, 250 μM PEP, 250 μM E4P, and 1 mM of the divalent metal salt. Reaction was started by the addition of DAHPS_{H6} to a final concentration of 50 nM. Initial rates were measured by Malachite Green/ammonium molybdate assay.

2.2.6. DAHPS_{H6} Inhibition with DAHP Oxime

Steady state kinetic assays to determine K_i was carried out by varying the DAHP oxime concentration from 0 to 1 mM while keeping the substrate concentrations constant at 100 μM PEP, 100 μM E4P, and 2 μM MnCl₂ in reaction buffer. DAHPS_{H6} was added to a final concentration of 10 nM to start the reaction. The reaction was monitored for 5 min using the Malachite Green/ammonium molybdate assay for P_i. Data were fitted to a three substrate, ordered binding competitive inhibitor model (eq. 2.3) using Grafit 5 software.⁸⁸

$$\frac{v_0}{[E]_0} = \frac{k_{cat} \left[\frac{[A][B][C]}{K_A K_B K_C} \right]}{1 + \frac{[A]}{K_A} + \frac{[A][B]}{K_A K_B} + \frac{[A][B][C]}{K_A K_B K_C} + \frac{[I]}{K_i}} \quad (2.3),$$

where [A], [B] and [C] are the concentrations of the substrates Mn^{2+} , PEP and E4P, respectively, and the corresponding Michaelis constants (K_M) are K_A , K_B and K_C . [I] and K_i are the inhibitor concentration, and its equilibrium dissociation constant.

2.2.7. Slow-binding Inhibition of DAHPS_{H6} by DAHP Oxime

In order to measure the ultimate binding of DAHP oxime binding to DAHPS_{H6} under slow-binding conditions, enzyme and inhibitor were first incubated together, then the other reaction components were added to start the reaction. DAHPS_{H6} (0.5 μM) and DAHP oxime (0 to 50 μM) were preincubated for 45 min in reaction buffer. The mixture was then diluted 25-fold into the substrate mixture (100 μM PEP, 100 μM E4P, 2 μM MnCl_2) in reaction buffer, and the initial velocity was measured.

2.2.8. Slow-binding Association Rate Constant, k_{on}

Time-dependant loss of activity was measured by preincubating 500 nM DAHPS_{H6} and 1 mM DAHP oxime plus 0.33 mM TCEP, and 0.25 mg/mL bovine serum albumin (BSA) in reaction buffer for varying amounts of time. The preincubated enzyme and inhibitor mixture was diluted 50-fold into reaction

buffer containing 100 μM PEP, 100 μM E4P, 3 μM MnCl_2 , and 0.25 mg/mL BSA. The association rate constant, k_{on} , was determined by fitting the initial velocity data to a first order eq. **2.4**:

$$v_t = v_i \cdot e^{-k_{\text{on}}t} + \text{offset} \quad (2.4),$$

The initial velocity with zero preincubation was v_i , and the initial velocity after preincubation for time, t , was v_t . The offset is a constant to fit the non-zero residual rate.

2.2.9. Slow-binding Dissociation Rate Constant, k_{off}

In 60 μL , 20 μM DAHPS_{H6} was preincubated with 3 mM DAHP oxime in reaction buffer at room temperature for 60 min to allow the formation of the $\text{DAHPS}_{\text{H6}} \cdot \text{DAHP}$ oxime complex. The mixture was desalted to separate the complex from excess inhibitor. This was done using Sephadex G-25 spin columns (GE Healthcare), centrifuged for 2 min at $719 \times g$ at 20 $^\circ\text{C}$. To the $\text{DAHPS}_{\text{H6}} \cdot \text{DAHP}$ oxime complex solution was added 1 mM TCEP, 1 mM PEP and 1 mM MnCl_2 . At set intervals, aliquots were taken and added to reaction buffer containing 100 μM E4P, 100 μM PEP, 5 μM MnCl_2 and the initial velocity was determined. Initial velocity data were fitted to eq. **2.5**:

$$v_t = v_i + \text{Limit} \cdot (1 - e^{-k_{\text{off}}t}) \quad (2.5),$$

where t is the preincubation time, v_t is the initial velocity at time = t , and k_{off} is the dissociation rate constant, v_i is the initial velocity at $t = 0$, and Limit is the maximum recovery of initial velocity at $t = \infty$.

2.2.10. Substrate Dependence of Inhibition

In order to determine the mode of inhibition, namely whether it is competitive, noncompetitive, or uncompetitive, the dependence of K_i on substrate concentrations was determined. Two substrate concentrations were held constant while the third was varied, along with the inhibitor concentration. [E4P] was varied from 0 to 170 μM while [DAHP oxime] was varied from 50 to 300 μM and the other substrates were held constant at [PEP] = 100 μM and [MnCl₂] = 2 μM . [PEP] was varied from 0 to 100 μM while [DAHP oxime] was varied from 50 to 200 μM and the other substrates were held constant at [E4P] = 30 μM and [MnCl₂] = 2 μM . [MnCl₂] was varied from 0 to 10 μM while [DAHP oxime] was varied from 50 to 300 μM and the other substrates were held constant at [E4P] = 60 μM and [PEP] = 60 μM .

2.2.11. Inhibition of DAHPS_{H6} During Catalytic Turnover

Slow-binding inhibition assays were normally performed by simply preincubating DAHPS_{H6} with DAHP oxime to form the DAHPS_{H6}•DAHP oxime complex, then adding the substrates to start the reaction. As with DAHPS_{H6}, preincubation of NeuB with its cognate oxime gave partial inhibition.^{124,128}

However, if the oxime was incubated with NeuB in the presence of all the substrates (i.e., when NeuB was actively catalyzing its reaction), complete inhibition was achieved after ≈ 6 h. In order to test whether the same thing occurred with DAHPS_{H6}, inhibition by DAHP oxime over 8 h in the presence of substrates was monitored. The reaction mixture contained 5 nM DAHPS_{H6}, 2 mM DAHPS oxime, 2 mM PEP, 2 mM E4P, 3 μ M MnCl₂ in reaction buffer, except with increased TCEP (1 mM), plus 0.25 mg/mL BSA. As DAHPS_{H6} lost activity over 8 h, control experiments lacking DAHP oxime were run in parallel.

2.2.12. Tryptophan Fluorescence

The effects of DAHP oxime binding on the melting temperature (T_m) of DAHPS_{H6} was probed through intrinsic tryptophan fluorescence. Fluorescence was measured with excitation at 280 nm and emission at 340 nm. Samples contained 0.5 μ M DAHPS_{H6} with 0.1 or 2 mM PEP, or 0.1 μ M MnCl₂, or 0.1 mM DAHP oxime in reaction buffer. Protein denaturation was carried out between 20 to 90 °C with $\Delta t = 1$ °C/min. Renaturation was carried out from 90 to 20 °C with $\Delta t = -1$ °C/min.

2.2.13. Determination of the Oligomeric Form of DAHPS_{H6} by Gel filtration

The oligomeric form of DAHPS_{H6} was probed by gel filtration. Samples (50 μ L) were chromatographed on a Superose 12 10/300 GL column (10 \times 300 mm, GE Healthcare) at a flow rate of 1 mL/min, with A₂₈₀ detection, in

running buffer (50 mM K-HEPES, pH 7.0, 100 mM KCl). The column was calibrated with ferritin (MW = 440 000), catalase (MW = 232 000), aldolase (MW = 158 000), albumin (MW = 67 000), ovalbumin (MW = 43 000) and ribonuclease K (MW = 13 700). Standards were prepared in running buffer. Both DAHPS_{H6} and the tag-free version, DAHPS, were tested. Sample injections included (i) 25 μ M DAHPS_{H6} or DAHPS, (ii) 25 μ M DAHPS_{H6}/DAHPS with 1 mM PEP and 1 mM MnCl₂, and (iii) 25 μ M DAHPS_{H6}/DAHPS with 2 mM DAHP oxime. The retention times were fitted to the calibration curve to determine molecular weight of the enzyme.

2.2.14. Glutaraldehyde Cross-linking

Gel filtration did not show any higher oligomers of DAHPS than the homotetramer. In order to test for transient formation of unstable higher oligomers, glutaraldehyde cross-linking experiments were performed. Samples included (i) 25 μ M DAHPS_{H6} only, (ii) 25 μ M DAHPS_{H6} + 2 mM DAHP oxime, or (iii) 25 μ M DAHPS_{H6} + 1 mM PEP + 1 mM MnCl₂. Samples were preincubated at room temperature for 45 min in reaction buffer. Glutaraldehyde (pentanedial, 5 mM) was added and the cross-linking was allowed to proceed for 30 s. Cross-linking was quenched by the addition of 250 mM Tris-glycine, pH 7.5. Sample buffer (30% glycerol, 25 mM Tris-acetate, pH 7.5, 0.025 % (w/v) Bromophenol Blue) was added (2 μ L of for every 5 μ L sample) and loaded onto a 10% native PAGE gel made with 25 mM Tris-acetate, pH 7.5. The gel was run at

200 V for 20 h. Protein bands were visualized by silver staining using the method of Blum et al.¹³⁰

2.2.15. Bacterial Culture Growth Assays

In 15 mL sterile round bottom Falcon tubes, 25 μ L of *E. coli* XL1 Blue, *E. coli* AG1 or *E. coli* MG1655 cultures were inoculated into 1 mL M9 minimal medium (1L of M9 medium is composed of; 9 g of M9 minimal salts; 0.4% (w/v) glycerol; 2mM MgSO₄; 100 μ M CaCl₂; 0.01mg/mL thiamine-HCl; 0.01mg/mL biotin; 80 μ L of trace metal mix [27 mg/mL FeCl₃•6H₂O, 1.3 mg/mL ZnCl₂, 10 mg/mL (NH₄)₆Mo₇O₂₄, 2.5 mg/mL CaCl₂•2H₂O, 2 mg/mL CoCl₂•6H₂O, 1.9 mg/mL CuSO₄•5H₂O, 3.3 mg/mL MnCl₂•4H₂O, 0.5 mg/mL H₃BO₃ in 1.2 M HCl.]) and incubated with shaking overnight at 37 °C. An aliquot of each overnight mixture was diluted 100-fold in M9 minimal medium and incubated with shaking for 8 h at 37 °C. Each culture was then diluted to OD₆₀₀ = 0.001 and added to an equal volume of DAHP oxime (0 - 32 mM) in a 96 well plate. The cells were shaken overnight at 37 °C, and OD₆₀₀ was read the following day.

2.3. Results

2.3.1. Protein Purification

N-terminally His₆-tagged DAHPS, DAHPS_{H6}, was purified using nickel affinity chromatography. The purity was verified by SDS/PAGE (Figure 2.1). As purified, the enzyme was unstable at high concentrations, precipitating when [DAHPS_{H6}] > 100 μM. Adding 10% glycerol helped, though precipitation from concentrated solutions was still sometimes observed. DAHPS_{H6} was stable for months at -80 °C.

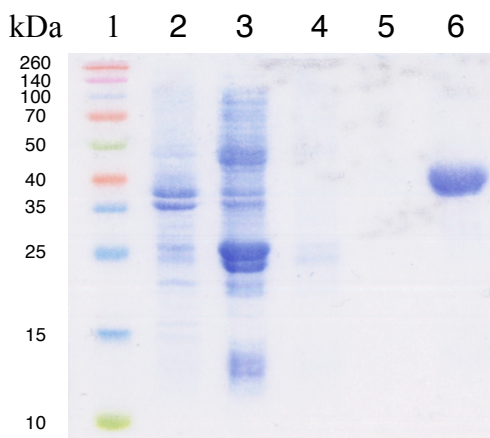


Figure 2.1: 13% SDS-PAGE gel of DAHPS_{H6}.

Lane 1: Molecular weight standards; lane 2: Pellet after centrifugation of cell lysate; lane 3: column flowthrough; lane 4: column wash with buffer A; lane 5: wash with 10 % buffer B; Lane 6: elution with 100 % buffer B.

2.3.2. DAHPS_{H6} Steady State Kinetics

Reaction rates were followed by detection of the P_i using the Malachite Green/ammonium molybdate colorimetric assay.¹²⁸ The steady state kinetic

parameters for DAHPS_{H6} were determined by fitting initial velocity data to eq. **2.1** (Table 2.1). The data followed traditional Michaelis-Menten kinetics.

Table 2.1: Steady state kinetic parameters for DAHPS_{H6}.

	Substrate		
	Mn ²⁺	PEP	E4P
ternary ordered sequential kinetic mechanism			
k_{cat} (s ⁻¹) ^a		16.4 ± 0.6	
$k_{\text{cat}}/(K_{\text{M,Mn}}K_{\text{M,PEP}}K_{\text{M,E4P}})$ (M ⁻³ •s ⁻¹) ^b		(1.5 ± 0.2) × 10 ¹⁵	
K_{M} (μM) ^b	5.5 ± 0.7	140 ± 20	15 ± 2
single substrate kinetic mechanism ^c			
k_{cat} (s ⁻¹)	14.4 ± 0.6	15.9 ± 0.7	18.4 ± 0.4
$k_{\text{cat}}/K_{\text{M}}$ (M ⁻¹ •s ⁻¹)	(6 ± 1) × 10 ⁷	(1.7 ± 0.4) × 10 ⁶	(7.7 ± 0.9) × 10 ⁵
K_{M} (μM)	0.26 ± 0.06	9 ± 2	24 ± 3

^a Fitted to eq. **2.1**.

^b Fitted to eq. **2.1b**, as it gave the same K_{M} values within experimental error as fitting to eq. **2.1**, but smaller standard errors. The fitted K_{M} values using eq. **2.1** were $K_{\text{M,Mn}} = 9 \pm 3 \mu\text{M}$, $K_{\text{M,PEP}} = 220 \pm 150 \mu\text{M}$, $K_{\text{M,E4P}} = 10 \pm 7 \mu\text{M}$.

^c Fitted to eq. **2.2**. This equation is incorrect for DAHPS, but is included in order to be able to compare with steady state kinetic parameters reported in the literature.

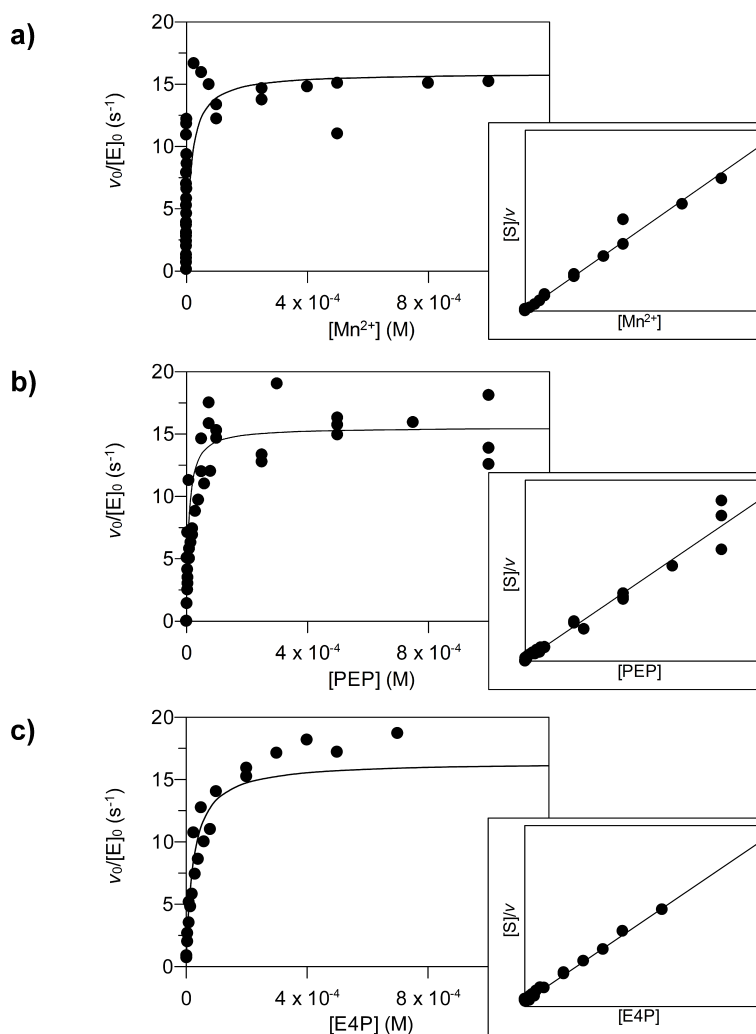


Figure 2.2: DAHPS_{H6} steady state kinetics.

Initial velocity vs. [substrate] and (inset) Hanes plots for each substrate: a) Mn²⁺, b) PEP, and c) E4P. The curves represent the best fit of the experimental data to eq. 2.1, for a ternary ordered sequential kinetic mechanism. For Hanes plots, the lines are the best fit linear regression of the $[S]/v$ vs. $[S]$ data.

2.3.3. Metal Dependence of DAHPS Activity

All known DAHPSs are divalent metal ion-dependent. Purified DAHPS_{H6} was partially active without adding metal, implying that it was purified with bound metal. The identity of the bound metal was not known. Previous studies implicated Fe²⁺ and/or Zn²⁺ as the preferred metals of DAHPS due to their

presence in the purified enzyme.³⁵ Inductively coupled plasma mass spectrometry (ICP-MS) analysis of purified DAHPS_{H6} revealed that the metals present in the largest amounts, relative to a buffer blank, were Mn, Ni, Cu, and, to a lesser extent, Co (Table 2.2). The high Ni concentration was presumably due to the fact that DAHPS_{H6} was purified by Ni²⁺ affinity chromatography, and likely scavenged Ni²⁺ from the affinity column. Given the extensive washing on the affinity column before elution with imidazole, weakly bound metals would have dissociated from DAHPS_{H6} before elution. Thus, only tightly-bound metal ions would have been detected. Ca was present in higher concentrations in the buffer blank than DAHPS_{H6} in the protein sample, so Ca binding would not have been sensitively detected in this experiment. Based on this experiment, DAHPS_{H6} bound a variety of metal ions *in vivo*.

Table 2.2: ICP-MS analysis of purified protein.

The protein sample contained 80 μM DAHPS_{H6} in 2 mL. Metal concentrations are in M.

Sample	Mg	Ca	Mn	Co	Ni	Cu
Buffer Blank	2.5×10^{-6}	1.2×10^{-4}	2.2×10^{-8}	2.0×10^{-9}	1.5×10^{-7}	1.7×10^{-7}
Protein sample	2.9×10^{-6}	1.4×10^{-4}	1.9×10^{-7}	5.8×10^{-9}	7.0×10^{-6}	3.3×10^{-6}
Concentration Ratio ^a	1.2	1.2	8.6	2.9	47	19

^a Concentration Ratio = $[\text{M}]_{\text{protein sample}}/[\text{M}]_{\text{buffer blank}}$

Treatment of DAHPS_{H6} with EDTA removed all activity, though the activity loss was gradual, indicating slow dissociation of DAHPS_{H6}•metal complex. It took a 48 h incubation with 10 mM EDTA to completely demetallate DAHPS_{H6}. The demetalation occurred in two stages, a quick demetalation event where majority of the activity was lost, followed by a slow demetalation that led

to complete inactivation. Presumably there were multiple metal species bound to DAHP_{H6}.

Reintroduction of single metals reactivated the enzyme. Of the activating metals, Mn²⁺ had the highest activity; Co²⁺, Ni²⁺, Fe²⁺ and Ca²⁺ had moderate activation, while Mg²⁺ and Zn²⁺ did not significantly reactivate DAHP_{H6} (Figure 2.3). Cu²⁺ had a narrow activation range (5 to 100 μM) outside of which no activation was observed. Fe²⁺ initially activated DAHP_{H6}, but the enzyme underwent inactivation over ~ 45 min, likely due to oxidation of Fe²⁺ to Fe³⁺, which cannot be utilized by the enzyme. As enzyme activity was greatest with Mn²⁺, it was used for all subsequent assays.

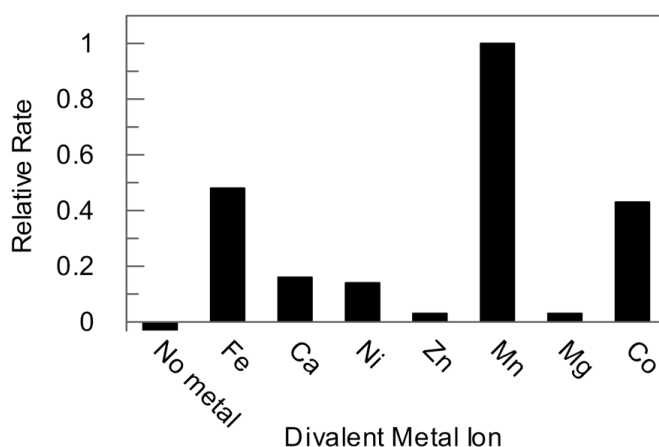


Figure 2.3: Activation of demetallated DAHP_{H6} by various divalent metal ions relative to Mn²⁺.

Relative rates of DAHP_{H6} with various divalent metal ions. Each reaction contained 1 mM of the respective metal with 0.1 mg/mL BSA, 1 mM DTT, 50 nM DAHP_{H6} and 250 μM of E4P and PEP. The rates were normalized to Mn²⁺ as DAHP_{H6} activity was greatest in the presence of Mn²⁺.

2.3.4. Inhibition

DAHP oxime inhibited DAHPS_{H6} with $K_i = 1.7 \pm 0.5 \mu\text{M}$ (Figure 2.4). The inhibition was not complete, as there was residual activity. Even at DAHP oxime concentrations of 1 mM, >500-fold higher than K_i , residual activity remained. NeuB inhibition by NeuNAc oxime showed similar residual activity.¹²⁴ Preliminary data with *Campylobacter jejuni* KDO8PS and KDO8P oxime have similar results, suggesting that residual activity is a common feature of the oxime inhibitor with the α -carboxyketose synthase family (Simanga Gama, personal communication).

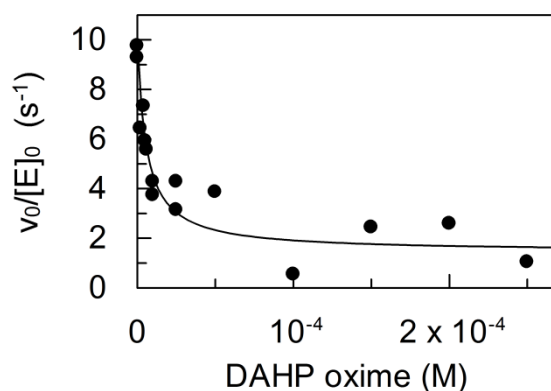


Figure 2.4: Fast-binding inhibition of DAHPS_{H6} by DAHP oxime.

Inhibition of NeuB by NeuNAc oxime was shown to yield complete inhibition when NeuNAc oxime was incubated with NeuB while the reaction was running. Under this condition, complete inhibition was observed over 6 h incubation.¹²⁴ When the same experiment was performed with DAHPS_{H6} and DAHP oxime, the enzyme remained active during the 7 hour experiment (Figure 2.5). From the graph there was no indication that complete inhibition would occur.

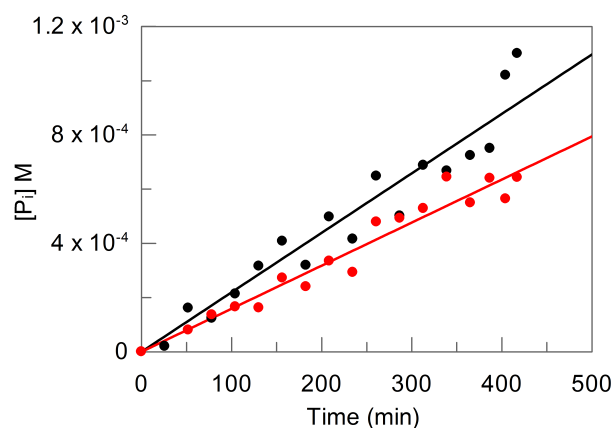


Figure 2.5: Inhibition of catalytic enzyme.

Effect of DAHP oxime on DAHPS_{H6} catalysis was monitored over 7 h. The reaction mixture contained 5 nM DAHPS_{H6}, 2 mM DAHPS oxime, 2 mM PEP, 2 mM E4P, 3 μ M MnCl₂ 0.25 mg/mL BSA and 1 mM TCEP in reaction buffer (red). Control experiments lacking DAHP oxime were run in parallel to account for loss of DAHPS_{H6} activity over time (black). The observed rate of phosphate production in the reaction mixture containing DAHP oxime was 65% of the uninhibited control. The expected relative rate, based on $K_i = 1.7 \mu\text{M}$, was 60%. However, based on $K_i^* = 81 \text{ nM}$, the expected relative rate was 7%. Thus, the extent of inhibition was more consistent with the fast-binding K_i value. It is not clear why inhibition did not increase with time to reflect K_i^* , though it could be related to the fact that slow-binding inhibition assays typically involved first forming the $E^* \cdot I$ complex in the absence of substrates. In any case, the results here clearly demonstrated that, unlike NeuB, complete inhibition was not observed at long reaction times.

2.3.5. Substrate Dependence of Inhibition

The inhibition patterns with respect to the three substrates were ambiguous, making it impossible to distinguish kinetically between competitive, noncompetitive, and uncompetitive inhibition.⁸⁸ This can be explained by the half-of-sites inhibitor binding (see Chapter 3). In the DAHP•DAHPS oxime X-ray crystallographic structures, the inhibitor bound in the active sites of two monomers of the tetrameric protein. Thus, inhibition must be competitive with respect to the enzyme subunits to which the inhibitor was bound, i.e., subunits B and C. The remaining unbound subunits retained activity with a decreased

apparent k_{cat} value, but no change in K_M values (Figure 2.6, Figure 2.7). This demonstrated that inhibition was noncompetitive with respect to subunits A and D, as K_M values would have increased for uncompetitive inhibition. Thus, the overall DAHP oxime inhibition mode was a combination of competitive and noncompetitive. The apparent inhibition mode shifted from primarily competitive at low [DAHP oxime], as the first two active sites became occupied, to primarily noncompetitive at high [DAHP oxime], when the residual activity was primarily from the unoccupied subunits in enzyme molecules with inhibitor already bound in two subunits.

The residual k_{cat} value at high inhibitor concentrations was 15% of the uninhibited enzyme's, which indicates that the k_{cat} value of the two unbound subunits (subunits A and D) was decreased 70% through their interactions with the two bound subunits (subunits B and C).

Inhibition with respect to Mn^{2+} followed a similar pattern. DAHP oxime did not occupy the same physical space as Mn^{2+} in the crystal structures, making it possible, in principle, that inhibitor and Mn^{2+} could bind simultaneously. This would make inhibition noncompetitive with respect to Mn^{2+} . On the other hand, none of the crystal structures contained both Mn^{2+} and DAHP oxime in the same subunit, implying that their binding was mutually exclusive, which would make inhibition competitive with respect to Mn^{2+} . It is possible, though, that Mn^{2+} and DAHP oxime not binding together was a crystallographic artifact. This question was resolved kinetically. At low Mn^{2+} concentration, a noncompetitive inhibition

pattern was observed (Figure 2.7C). At higher Mn^{2+} concentrations, the inhibition behavior became competitive, such that uninhibited rate was achieved at high Mn^{2+} concentrations (Figure 2.8).

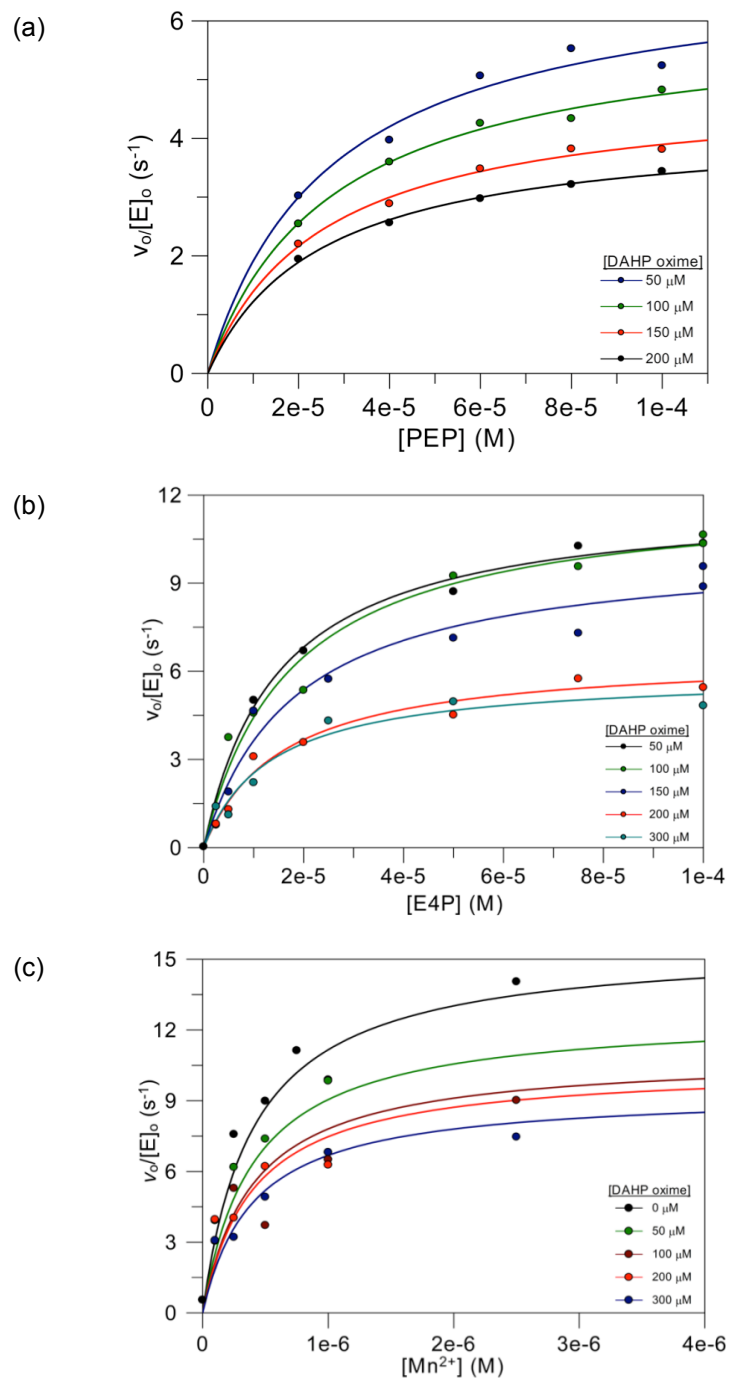


Figure 2.6: Substrate and metal dependence of DAHP oxime inhibition.

Initial velocities with one variable substrate concentration and variable [DAHP oxime].
 (a) Variable [E4P], [Mn²⁺] = 2 μM, [PEP] = 60 μM. (b) Variable [PEP], [Mn²⁺] = 2 μM, [E4P] = 30 μM. (c) Variable [Mn²⁺], [E4P] = 60 μM, [PEP] = 60 μM.

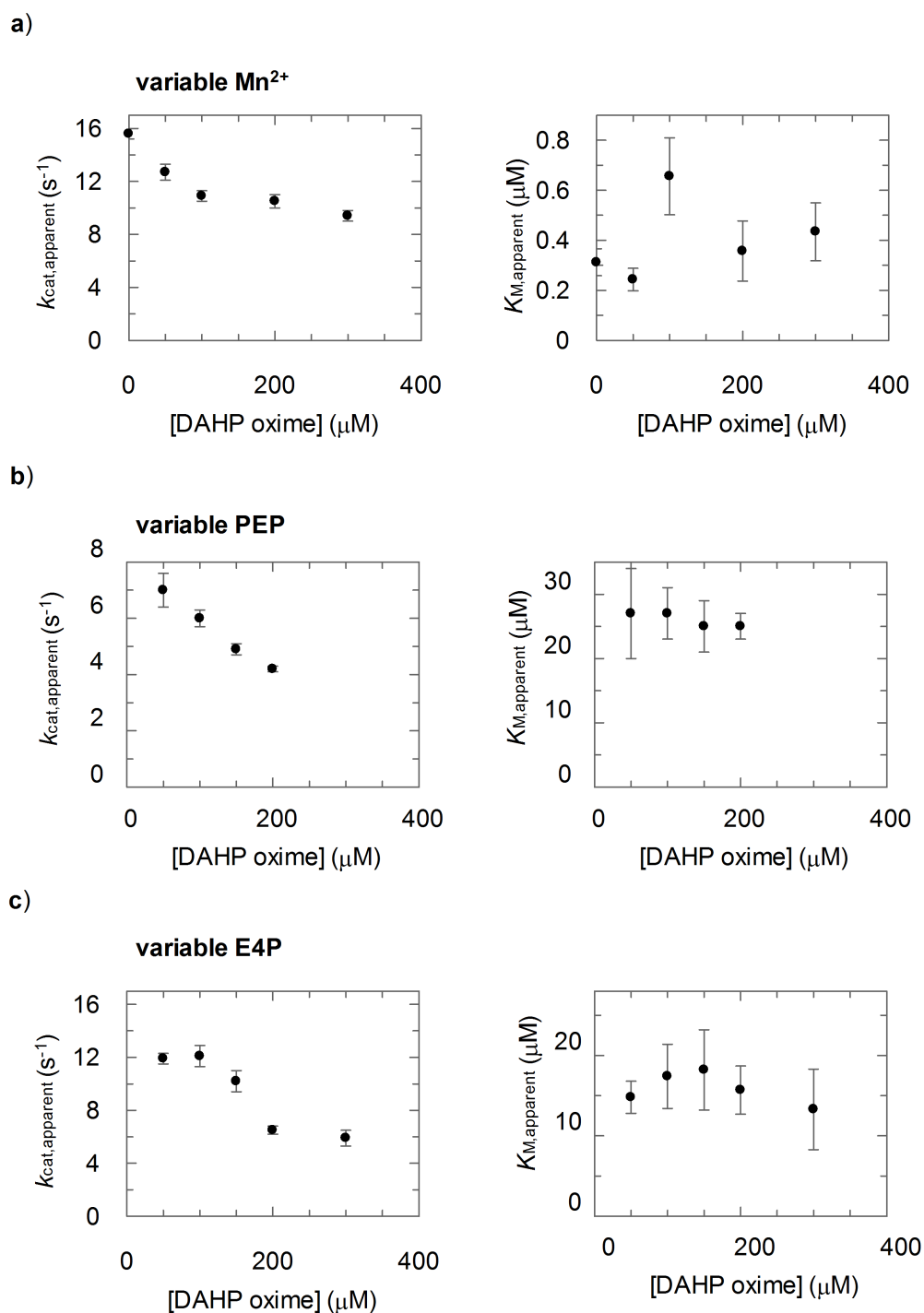


Figure 2.7: Substrate and metal dependence of DAHP oxime inhibition.

Initial velocities with one variable [substrate] and variable [DAHP oxime]. **a)** Variable $[Mn^{2+}]$, $[E4P] = 60 \mu M$, $[PEP] = 60 \mu M$. **b)** Variable $[PEP]$, $[Mn^{2+}] = 2 \mu M$, $[E4P] = 30 \mu M$. **c)** Variable $[E4P]$, $[Mn^{2+}] = 2 \mu M$, $[PEP] = 60 \mu M$.

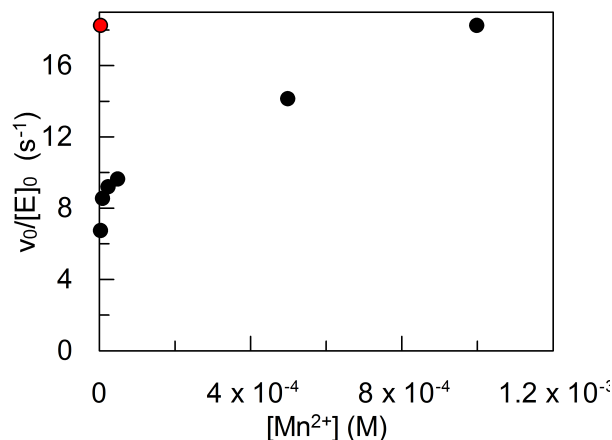


Figure 2.8: Metal ion dependence of DAHP oxime inhibition.

Effect of high $[\text{Mn}^{2+}]$ on inhibition. Mn^{2+} concentration was varied while $[\text{DAHP oxime}]$ was held constant at $100 \mu\text{M}$ (black symbols). Control rate with no DAHP oxime is highlighted in red.

2.3.6. Slow-Binding Inhibition

Slow-binding inhibition of DAHPS_{H6} by DAHP oxime was modelled as a two-step binding process in which there is a fast-binding step to form a loose $\text{E}\cdot\text{I}$ complex, followed by a slower step (e.g., conformational change) to form a tight $\text{E}^*\cdot\text{I}$ complex (Scheme 2.1).

Scheme 2.1: Kinetic scheme for slow-binding inhibition.



k_{on} Determination

When DAHPS_{H6} and DAHP oxime were preincubated together, slow-binding inhibition was observed. That is, when DAHPS_{H6} was preincubated with DAHP oxime for an extended time before adding substrates, the initial velocity decreased with increasing pre-incubation time. The activity loss followed an

apparent first order rate constant of $0.24 \pm 0.08 \text{ min}^{-1}$, or $t_{1/2} = 2.9 \text{ min}$. Maximum inhibition was observed by 20 min of preincubation (Figure 2.9).

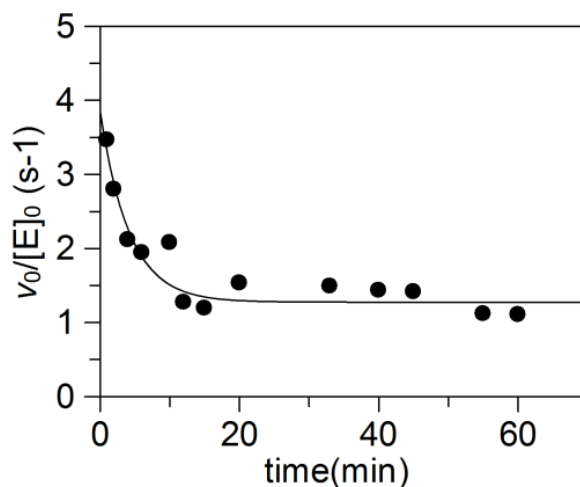


Figure 2.9: Time dependent inhibition of DAHPS_{H6} with DAHP oxime.

DAHPS_{H6} (2.5 μM) was preincubated with 5 mM DAHP oxime for up to 1 h. The preincubated mixture was added to the substrates in reaction buffer to start the reaction. The concentrations in the reaction mixture were 20 nM DAHPS_{H6} and 20 μM DAHP oxime. The kinetic assays to determine initial velocity ($v_0/[E]_0$) were fast relative to k_3 .

k_{off} Determination

In order to measure the rate of DAHPS_{H6}•DAHP oxime dissociation, the complex was pre-formed, excess DAHP oxime was removed by gel filtration, and then the purified E*•I complex was incubated with large excesses of PEP and MnCl₂ to ensure that when the E*•I complex dissociated, E would preferentially bind Mn²⁺ and PEP, rather than re-bind the inhibitor. Without added PEP and MnCl₂, there was no return of activity, presumably due to inhibitor re-binding. The enzyme concentration was kept above 5 μM to ensure the stability of the enzyme during the extended incubation. The control reaction (DAHPS_{H6} in the absence of inhibitor) retained > 90% activity during the dissociation period. An

off rate, k_{off} , of $0.012 \pm 0.004 \text{ min}^{-1}$ was obtained by fitting the data to eq. 2.4

(Figure 2.10). This corresponds to a dissociation half-life of $t_{1/2} = 58 \text{ min}$.

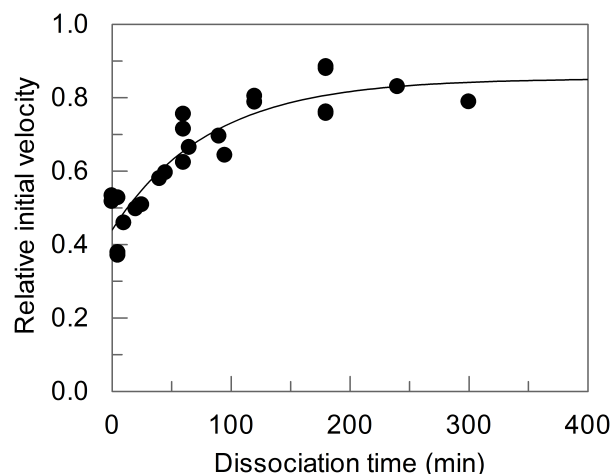


Figure 2.10: Determining the E*•I dissociation rate.

Preformed DAHPS_{H6}•DAHP oxime complex (E*•I) was incubated for varying times in the presence of large excesses of PEP (1 mM) and MnCl₂ (1 mM) in order to trap any dissociated enzyme as the DAHPS•Mn²⁺•PEP complex, then mixed with E4P in reaction buffer to start the reaction and determine the initial velocity. The relative initial velocity, compared with the no inhibitor control reaction, is plotted.

*Slow-binding inhibition constant, K_i^**

The concentration dependence of slow-binding inhibition was examined in an effort to determine the equilibrium dissociation constant for slow-binding, K_i^* .

The concentration dependence when DAHPS_{H6} and DAHP oxime were preincubated together indicated cooperative inhibitor binding. Cooperative binding is often described with the Hill equation (eq. 2.6).

$$\frac{v_0}{[E]_0} = (\max - \min) \times \frac{1 - [I]^n}{K_i^* + [I]^n} + \min \quad (2.6),$$

where max and min are $v_0/[E]_0$ at zero and infinite [I], respectively, [I] is the inhibitor concentration, K_i is the equilibrium dissociation constant, and n is the Hill coefficient.

Values of $n > 1$ indicate cooperative binding, with n being commonly, but not always accurately, interpreted as the number of ligand molecules that bind per protein molecule. The slow-binding inhibition data did not yield a satisfactory fit to eq. 2.6; the fitted value of n was always close to the initial estimate, regardless of the initial guess (Figure 2.11). Thus, the equation had poor resolving power for the value of n . Forcing a fit to a Hill coefficient of $n = 2$ yielded a reasonable fit to the data at high [I], but not low [I] values. Conversely, fixing n at a large value ($n=8$ shown) yielded a reasonable fit to the data at low [I], but not at high [I].

An alternative method of determining n is to rearrange the Hill equation (eq. 2.7), and perform linear regression to obtain n .

$$\log \frac{f}{1-f} = n \log([I]) - \log(K_d) \quad (2.7),$$

where f is the fractional inhibition at a given value of [I] (eq. 2.8),

$$f = (\max - i)/(\max - \min) \quad (2.8),$$

where max, min, and i are the $v_0/[E]_0$ values at $[I] = 0, \infty$, and i , respectively. Fitting the slow-binding inhibition data to eq. 2.7 gave $n = 4.65$ (Figure 2.12a). With a fixed value of $n = 4.65$, a reasonable fit to eq. 2.6 was obtained (Figure 2.12b). Preliminary studies with two derivatives of DAHP oxime, DAHP *O*-ethyloxime and DAHP *O*-(2-fluoroethyl)oxime, showed similar

highly cooperative behaviour. With DAHP *O*-ethyloxime the slow binding half life was reduced from $t_{1/2} \approx 2.9$ min to < 1 min (data not shown). Fitting the pre-incubated inhibition profile of DAHP *O*-ethyloxime (Figure 2.13) with eq. 2.7 gave $n = 7.9$. Inhibition with DAHP *O*-(2-fluoroethyl)oxime showed the strong cooperativity without preincubation (Figure 2.14). The presence of slow binding inhibition by DAHP *O*-(2-fluoroethyl)oxime was not tested. Also DAHP *O*-(2-fluoroethyl)oxime showed complete inhibition of DAHPS_{H6}. Due to the lack of data points in the steep part of the curve, the data could not be fit to eq. 2.7. Fitting to eq. 2.6 with $n = 18$ provided a reasonable fit to the data.

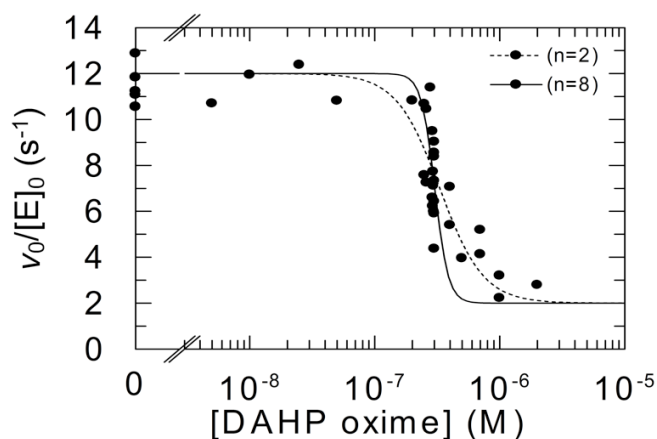


Figure 2.11: Inhibition curve depicting rate vs. DAHP oxime concentration.

Inhibition velocities were measured after 45 min preincubation. Reaction mixtures contain 100 μ M PEP, 100 μ M E4P, 2 μ M MnCl₂ and 20 nM DAHPS_{H6} in reaction buffer, and the initial velocity was measured. The concentration of DAHP oxime was varied from 0 – 10 μ M. Data was fit to eq. 2.6.

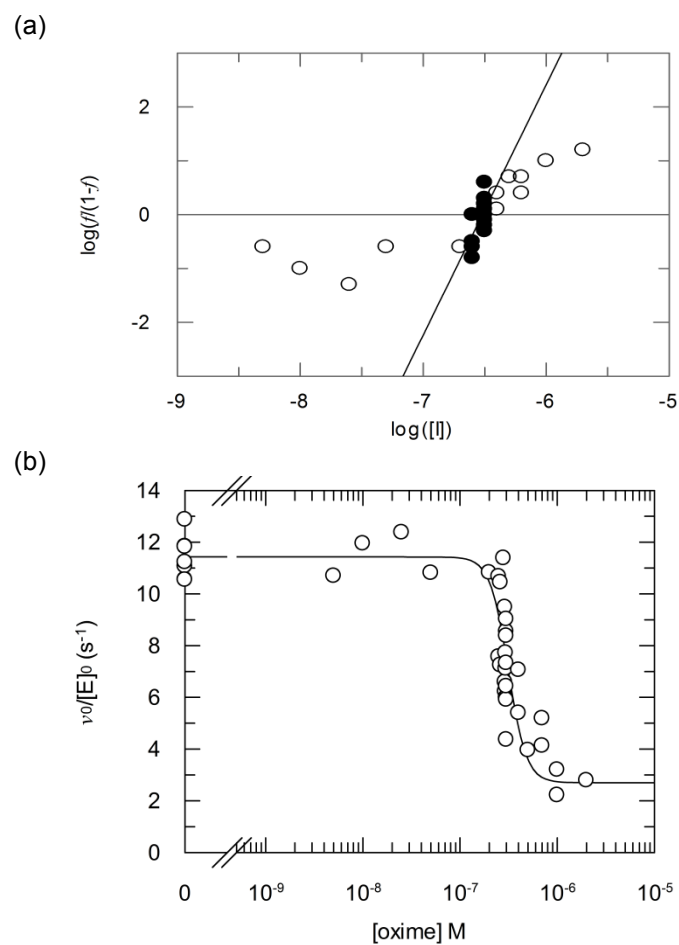


Figure 2.12: Inhibition of DAHPS_{H6} with DAHP oxime, shows cooperative binding when DAHPS_{H6} and DAHP oxime are preincubated.

(a) Fit to eq. 2.7 gives $n = 4.65$. Only data in the steep part of the curve are fitted in this analysis. (b) Fit to eq. 2.6 with fixed $n = 4.65$.

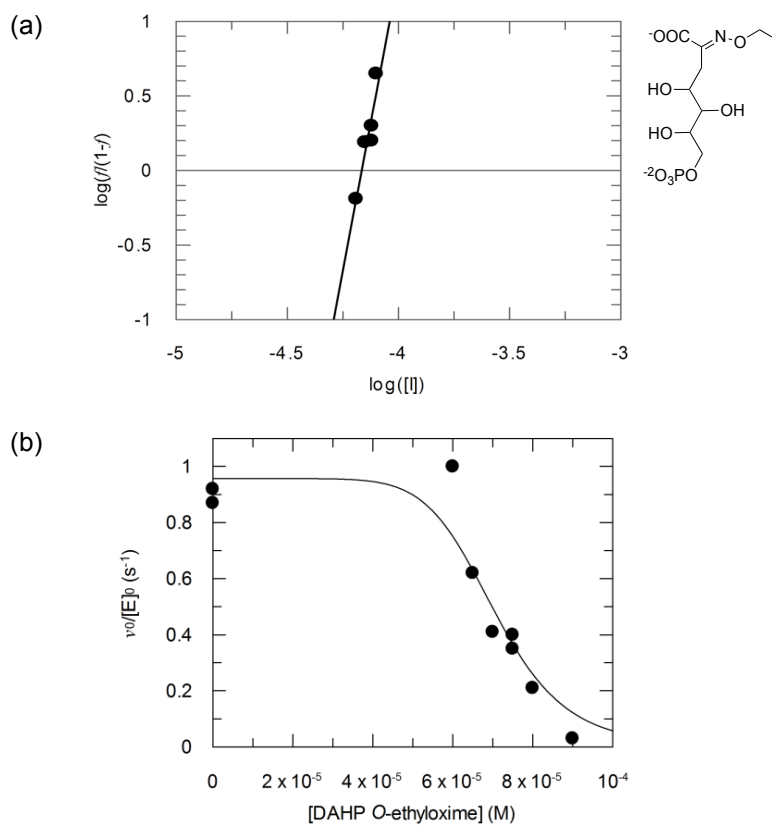


Figure 2.13: Inhibition profile of DAHPS_{H6} by DAHP O-ethyloxime.

Initial velocities were measured after 60 min preincubation. The reaction mixture contained 100 μ M E4P, 100 μ M PEP, 5 μ M MnCl₂, and 15 nM DAHPS_{H6} in reaction buffer. The DAHP O-ethyloxime concentration was varied from 0 – 100 μ M. (a) The fit to eq. 2.7 gives $n = 7.9$. (b) $v_0/[E]_0$ vs. [DAHP O-ethyloxime], with data fitted to eq. 2.6 using $n = 7.9$.

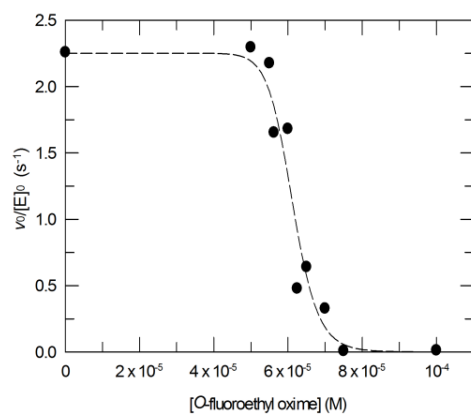


Figure 2.14: Inhibition profile of DAHPS_{H6} by DAHP O-(2-fluoroethyl)oxime.

The reaction mixture contained 125 μ M E4P, 125 μ M PEP, 10 μ M MnCl₂, and 50 nM DAHPS_{H6} in reaction buffer. [DAHP O-(2-fluoroethyl)oxime] was varied from 0 – 100 μ M, and the data were fitted to eq. 2.6 using $n = 18$.

2.3.7. BSA effects

Bovine serum albumin (BSA) was added to the reaction mixture in some assays to stabilize DAHPS_{H6}'s activity when it was used at low concentrations. It was found, however, that BSA decreased inhibition by DAHP oxime in a concentration-dependent manner (Figure 2.15). It would appear that BSA interacts with DAHPS oxime nonspecifically. This interaction would reduce the effective inhibitor concentration in solution and thus reduce inhibition.

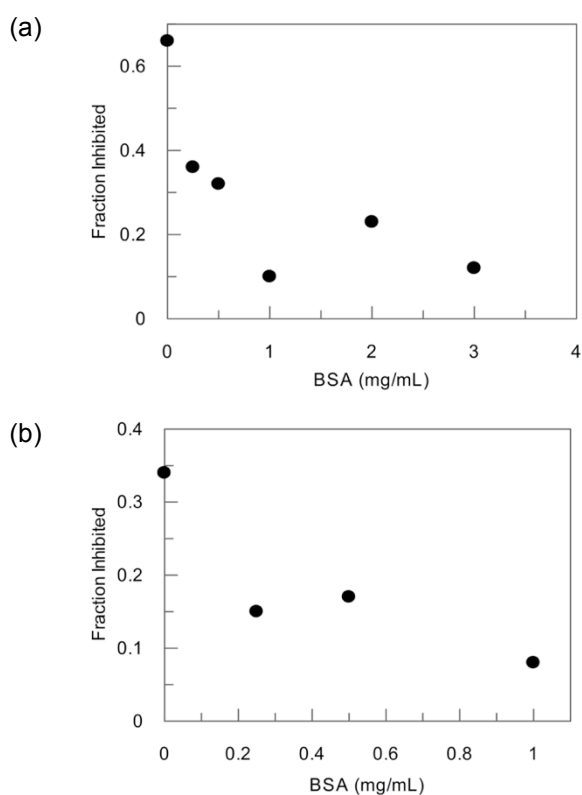


Figure 2.15: Effect of BSA on DAHPS_{H6} inhibition by DAHP oxime.

(a) No preincubation of DAHPS_{H6} and DAHP oxime. The DAHP oxime concentration was 200 μ M, while the BSA concentration was increased from 0 to 3 mg/mL. (b) DAHPS_{H6} and DAHP oxime were preincubated for 30 min. The final concentration of DAHP oxime was 1 μ M.

2.3.8. *Oligomerization*

Given the fact that two DAHP oxime molecules bound per DAHPS tetramer in the crystal structures (see Chapter 3), the maximum expected value of n , the Hill coefficient, was 2. One explanation of the observed values of $n > 2$ (Figure 2.11) is the possibility that DAHP oxime binding caused DAHPS_{H6} to oligomerize. Potential changes to the oligomeric states of DAHPS_{H6} upon DAHPS oxime binding were investigated by gel filtration chromatography and glutaraldehyde cross-linking.

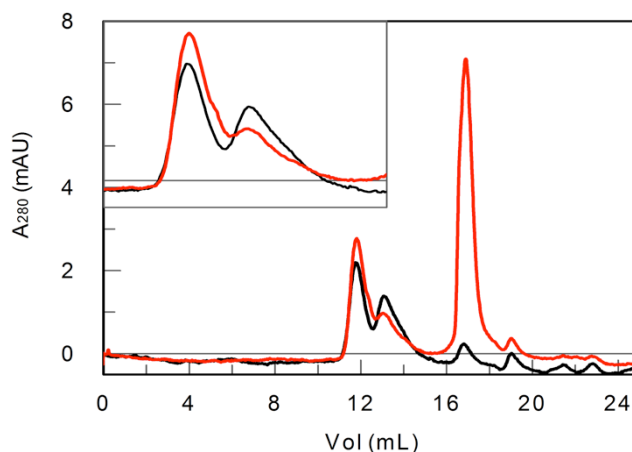
Free DAHPS_{H6} appeared to be a mixture of tetramer and dimer upon chromatography on a Superose 12 10/300 GL gel filtration column (Figure 2.16). This was unexpected, as previous gel filtration studies indicated solely a tetramer form of DAHPS.^{35,131} Cross-linking studies had provided evidence for trimer, dimer and monomer forms (Figure 2.17), though cross-linking studies are more prone to artifacts,¹³¹ while gel filtration is more reliable in indicating the dominant form in solution. Addition of substrates or DAHP oxime changed the tetramer/dimer equilibrium towards tetramer, though dimer was still detectable. No higher oligomers were visible by gel filtration.

Table 2.3: Superose 12 10/300 GL column calibration and DAHPS_{H6} molecular weights.

Protein	Mol. wt. (Da)	Elution volume (mL)
DAHPS _{H6} , unbound		
tetramer	161 000 (obs) ^a	11.78
dimer	64 000 (obs) ^b	13.06
DAHPS _{H6} •DAHP oxime		
tetramer	158 000 (obs) ^a	11.80
dimer	65 000 (obs) ^b	13.03
Molecular weight standards		
Blue Dextrin 2000	2 000 000	8.44
Ferritin	440 000	10.39
Catalase	232 000	11.62
Aldolase	158 000	12.04
Albumin	67 000	12.28
Ovalbumin	43 000	13.20
Ribonuclease K	13 700	15.70

^a Calculated molecular weight = 157 764 Da

^b Calculated molecular weight = 78 882 Da

**Figure 2.16: DAHPS_{H6} on Superose 12 10/300 GL column.**

Injections are of 50 μ L of 25 μ M DAHPS_{H6} (black) or 25 μ M DAHPS_{H6} with 5 mM DAHP oxime (red). The first peak (11.8 mL) was consistent with the molecular weight of the DAHPS_{H6} tetramer, while the second peak (13.7 mL) was consistent with the dimer (Table 2.3). The third peak (>16 mL) was small molecular weight species, presumably DAHP oxime and buffer components. Addition of DAHP oxime caused a redistribution of the tetramer/dimer equilibrium favouring more tetramer. The inset shows an expanded view from 10 to 16 mL of the chromatogram.

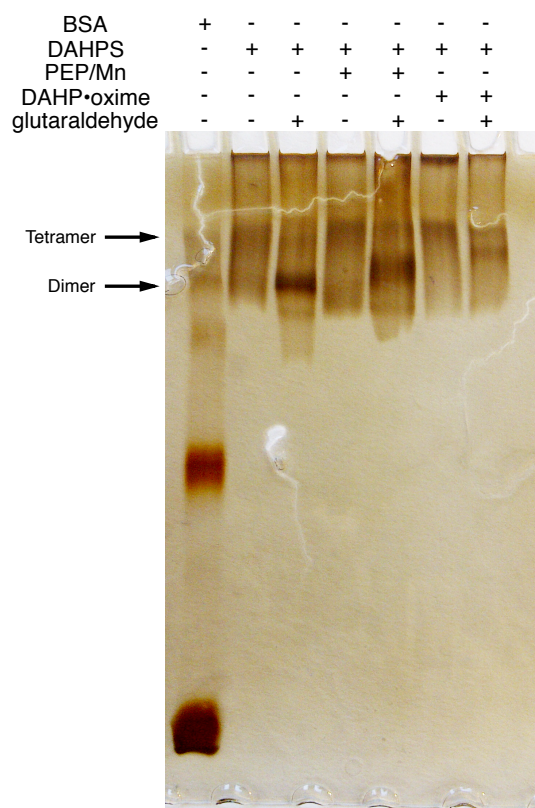


Figure 2.17: 10% native gel electrophoresis of DAHPS_{H6} cross-linked with and without DAHP oxime.

DAHPS_{H6} (25 μ M) was incubated in the absence or presence of substrates (1 mM PEP, 1 mM Mn²⁺), or 2 mM DAHP oxime. Samples were preincubated for 45 min before cross-linking with 5 mM glutaraldehyde. The cross-linking reaction was quenched with 250 mM Tris-glycine, pH 7.5.

In spite of being more prone to artifacts, cross-linking experiments were conducted to test whether transient higher order oligomers, not visible by gel filtration, were forming.¹³² DAHPS_{H6} was prone to forming very high molecular weight species that did not enter the gel when cross-linked with 5 mM glutaraldehyde for longer than 1 min. Cross-linking with 5 mM glutaraldehyde for 30 s, then quenching the cross-linking reaction with 200 mM Tris-glycine, pH 7.5 produced an acceptable level of cross-linking. Cross-linking of DAHPS_{H6} in

the presence and absence of oxime did not produce observable higher order oligomers.

In the non-cross-linked DAHPS_{H6} sample, dimeric and tetrameric species are visible. Upon cross-linking, a lower band also appears, presumably the monomer, similar to what was observed previously upon cross-linking with dimethylsuberimidate.¹³¹ Interestingly, in the presence of PEP and Mn²⁺ the dimer band appeared to shift, for reasons that are not clear. With DAHP oxime the dimer peak was further shifted. The cause of this shift is unclear, but it could possibly indicate a slow equilibrium of dimer/tetramer (or even trimer) species, a large conformational change, or some other cause. The non-cross-linked sample containing DAHP oxime had a higher proportion of protein that did not enter the gel with respect to the other samples, demonstrating that cross-linking was not solely responsible for the formation of very high molecular weight species. No clear bands of oligomer structures higher than tetramers was observed. This was consistent with results from the gel filtration experiment.

Tryptophan fluorescence

There are four tryptophan residues in each DAHPS monomer. One of the residues (W159), is buried in the core of the protein close to the active site, and W104 is located in the loop whose structure changes upon DAHP oxime binding (see Chapter 3). As Trp fluorescence is sensitive to its environment, and can often be used to detect conformational changes and/or ligand binding, we attempted to use Trp fluorescence as a probe to study changes in DAHPS melting temperature

in response to substrate/inhibitor binding. Our data showed no changes of the free DAHPS_{H6} curve from the baseline losses of signal from which melting temperature could be determined (Figure 2.18). DAHP oxime-bound DAHPS_{H6} melting curves were similar to free enzyme. PEP-bound melting curves were more characteristic of tryptophan melting curves from which a melting temperature could be determined, $T_m = 65^\circ\text{C}$ (Figure 2.18) based on 50 % fractional denaturation. However due to the overall poor signal and inability to measure melting temperatures for both the free and DAHP oxime-bound DAHPS_{H6}, this experiment was not pursued any further.

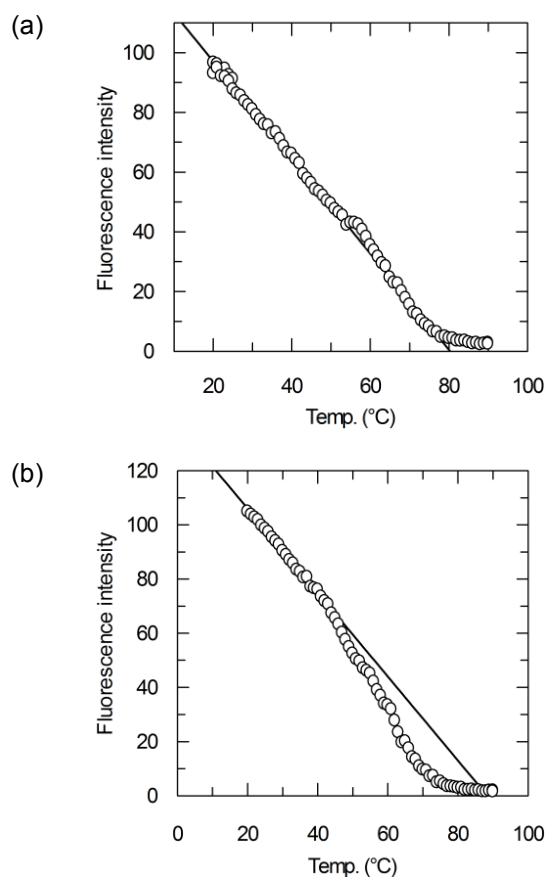


Figure 2.18: Tryptophan fluorescence vs. temperature of DAHP_{H6} in the presence and absence of PEP.

(a) Melting curve of free DAHPS_{H6} (500 nM) in reaction buffer from 20 to 90 °C with $\Delta t = 1$ °C/min. (b) Melting curve of DAHPS_{H6} (500 nM) with 0.1 mM PEP in reaction. $T_m = 65^\circ\text{C}$.

In culture activity of DAHP oxime against E. coli

Cell-based assays in 96 well plates were used to probe the activity of DAHP oxime against *E. coli* in culture. DAHP oxime was screened against three strains of *E. coli*, namely XL1-Blue, AG1 and MG1655. XL1-Blue and AG1 are cloning strains, while MG1655 is a derivative of wild-type K-12 strain with minimal genetic modification.

XL1-Blue showed a concentration-dependent inhibition of cell growth. No inhibition was observed with MG1655 or AG1 strains (Figure 2.19).

Inhibition of growth in XL1-Blue cells suggested that DAHP oxime had activity against live cells, although inhibition of cell growth due to other factors other than DAHPS inhibition cannot be ruled out. The lack of inhibition in AG1 and MG1655 could be a result of three factors. The first is permeability; the highly charged DAHP oxime will not favour passive diffusion through the lipid membrane. Second, alternate pathways may compensate for DAHPS inhibition. Third, resistance mechanisms may chemically modify DAHP oxime, or efflux pumps could remove it from the cell. It is also possible that the incomplete inhibition seen *in vitro* occurs *in vivo*, and the residual activity is sufficient for cell viability.

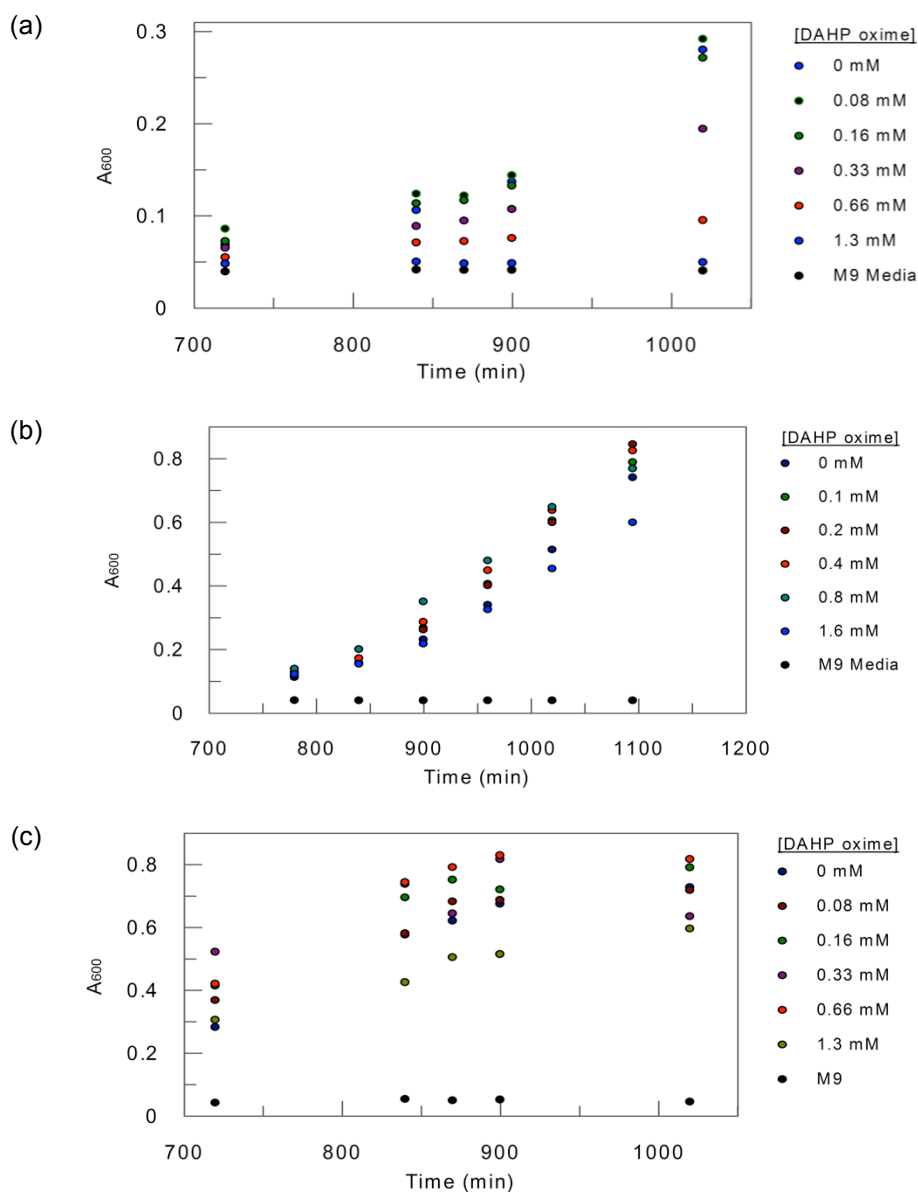


Figure 2.19: In culture assay of DAHP oxime against *E. coli* cells lines.

The effect of DAHP oxime on the growth of *E. coli* cultures was followed. (a) XL1 Blue, (b) AG1 and (c) MG1655 cells. Cultures were grown in 96 well plates incubated at 37°C with shaking at 300 rpm. OD₆₀₀ readings were taken periodically to monitor growth.

2.4. Discussion

2.4.1. Kinetics

The steady-state kinetic constants for His₆-tagged DAHPS(Phe), DAHPS_{H6}, were determined (Table 2.1). The fitted kinetic parameters differ from those previously reported for wild-type enzyme (Table 2.4), largely because previous kinetic constants were fitted to the single substrate Michaelis-Menten equation (eq. 2.2), rather than to the correct, ternary ordered sequential kinetic mechanism (eq. 2.1).^{32,133-135}

The DAHPS reaction has been characterized as an ordered sequential bi-bi mechanism.^{16,34} This means that PEP binds before E4P; the chemical reaction occurs once both substrates are bound, and then the products are released in order, first P_i, then DAHP. In this description, the metal ion is ignored. Although, the metal binding order with respect to PEP and E4P has not been demonstrated kinetically, its position buried in the active site behind PEP strongly implies that it must bind before PEP. Due to the absolute requirement of a metal ion for catalysis and the metal dependence of inhibition, we treated the metal as a substrate and fitted the data to the three substrate ordered binding equation (eq. 2.1). Though the single substrate Michaelis-Menten equation (eq. 2.2) has been used in the literature,^{32,133-135} it leads to artifactually low apparent K_M values. For example, when measuring the K_M of Mn²⁺ at saturating PEP and E4P concentrations, the high PEP and E4P concentrations can trap Mn²⁺ in the active

site, decreasing the apparent $K_{M,Mn}$ value. Similarly, high concentrations of E4P can trap PEP. The single substrate Michaelis-Menten equation, eq. 2.2, does not take this into account. The apparent $K_{M,Mn}$ and $K_{M,PEP}$ values derived from eq. 2.2 are 35- and 24-fold lower, respectively, than the true values derived from eq. 2.1 (see Table 2.4). This is problematic because the K_M values from eq. 2.2 have been used in the literature in eq. 2.3 to find K_i ; however, because the K_M values are artifactually low, and because the substrates compete with the inhibitor for enzyme binding, this leads to artifactually low K_i values being reported.

For the purposes of comparison, we also fitted our initial velocity data to eq. 2.2, which resulted in kinetic parameters that are more in line with published figures (Table 2.4). $K_{M,Mn}$ was similar to that previously reported for wild-type enzyme. There was an 5-fold increase in $K_{M,PEP}$ and 8-fold increases in $K_{M,E4P}$ between our results and the values reported by Stephens et al.,³⁵ but a smaller difference when compared to others.¹³³⁻¹³⁵ Considering the variance in all reported values, our data is in line with what has previously been reported. Some of the differences can be explained by differences in assay conditions. Our assays were run in 50 mM K-HEPES, pH 7.0, with 100 mM KCl, while other groups used 10 to 50 mM Bis-Tris propane, pH 6.8. The higher ionic strength will screen ionic interactions, leading both to decreased favourable interactions (e.g., phosphate with Arg) and decreased unfavourable interactions (e.g., phosphate with Asp). Higher ionic strength also strengthens hydrophobic interactions. Also, all assays were run in the presence of the reducing agent TCEP. Reducing agents

were not used in the other reports. Differences in the reported k_{cat} values also can be attributed to enzyme preparations. Furdui et al.¹³³ determined that in their purification only 30% of the enzyme was active. Active enzyme concentration was not determined in this study. The presence of inactive enzyme would decrease the apparent k_{cat} and k_{cat}/K_M values, but not K_M .

The K_i value for DAHP oxime, 1.7 μM , was found by fitting initial velocity data to eq. 2.3, using the steady state kinetic parameters obtained with eq. 2.1. In contrast, fitting the same data to eq. 2.3, but using K_M values obtained with eq. 2.2, as done in other reports,^{116, 117, 118, 120} decreased the apparent K_i value dramatically to 13 ± 3 nM. When comparing the K_i value of DAHP oxime with previously reported inhibitors (Figure 1.10), it is important to be aware of the different ways in which K_i values were calculated.

Table 2.4: Steady state kinetic parameters for *E. coli* DAHPS(Phe).

	k_{cat} (s^{-1})	$K_{M,\text{Mn}}$ (μM)	$K_{M,\text{PEP}}$ (μM)	$K_{M,\text{E4P}}$ (μM)	IC50(Phe) (μM)
this study, eq. 2.1 ^a	16.4	5.5	140	15	
this study, eq. 2.2 ^b	16	0.25	9	23	
this study					15 ± 8^c
Sundaram et al. ¹³⁴	32		9	86	
Tran et al. ¹³⁵	26			39	
Stephens et al. ³⁵	61	0.56	2	170	12
Furdui et al. ¹³³	23 ^d	1			

^a Eq. 2.1 is for a ternary sequential ordered kinetic mechanism (see Table 2.1).

^b Eq. 2.2 is for a single substrate kinetic mechanism (see Table 2.1).

^c IC₅₀ was derived from the following equation; the fitted value of $s = 2.1 \pm 0.2$.

$f = 1/\{1 + ([\text{Phe}]/\text{IC}_{50})^s\}$, where f is the fractional activity, and s is the slope factor.

^d Enzyme was reported to be 30% active.

2.4.2. Oligomeric Form

The appearance of both tetramer and dimer species in gel filtration chromatograms was somewhat surprising given previous reports that DAHPS(Phe) is a tetramer in solution.^{35,131} Presumably the presence of the *N*-terminal His₆-tag near the dimer-dimer interface affected the dimer/tetramer equilibrium. However, given the similarity of steady state kinetic parameters in this study compared with literature values, plus the facts that the Phe-sensitive isozyme has recently evolved³⁷ and that both the Tyr-sensitive and Trp-sensitive isozymes are dimers, the change in the dimer/tetramer equilibrium should not affect catalysis significantly. The Glu24Gln mutation that renders the Phe-sensitive DAHPS a dimer in solution has been reported to have similar kinetic parameters as those of the wild-type.¹³⁶

2.4.3. Inhibition

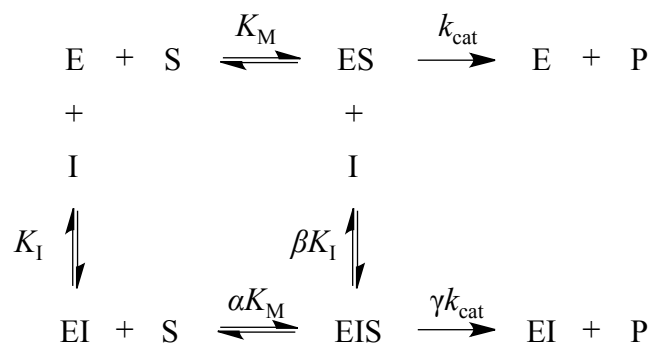
There are three possible modes of non-covalent enzyme inhibition: competitive, noncompetitive or uncompetitive^{87,88} (Scheme 2.2). Mixed mode inhibition are also possible, for example, where an inhibitor has features of both noncompetitive and uncompetitive inhibition.

(1) Competitive inhibitors bind specifically to the free enzyme. Inhibitor binding precludes substrate binding and is therefore mutually exclusive. The EI complex is catalytically inactive (Scheme 2.2, K_i).

(2) Noncompetitive inhibitors are those compounds that bind at a site different from the substrate binding site. As such, they can bind to either the free enzyme or substrate bound enzyme. In most cases the EIS complex is a dead end complex, though it may retain partial activity (Scheme 2.2, $K_I = \beta K_I$).

(3) Uncompetitive inhibitors bind specifically to the ES complex. They require formation of the ES complex to allow them to bind (Scheme 2.2, βK_I). This kind of inhibition is most commonly seen in multisubstrate enzymes, where the inhibitor binds in the active site only after binding of the first substrate. In this case the inhibitor would be uncompetitive with respect to the first substrate and competitive with respect to the second substrate.

Scheme 2.2: Schematic representation of enzyme inhibition.



For noncompetitive and uncompetitive inhibitors, EIS is usually a dead end complex. However, as the inhibitor and substrate are bound in different areas of the protein, it is possible that their binding alters the enzyme conformation such that the binding of I to E affects the K_M by a factor α . When $\alpha > 1$, the binding of substrate to the EI complex is hindered relative to the free enzyme. When $\alpha < 1$, substrate binding is more favourable (when small molecule is an activator rather

than inhibitor), and when $\alpha = 1$ there is no effect of the binding of I on the substrate. In some cases, EIS is not a dead end complex; rather, it is still able to catalyze the reaction, albeit at a slower rate ($0 < \gamma < 1$).

The structure of DAHP oxime resembles the substrates E4P and PEP taken together, and it bound in the active sites of subunits B and C, as shown by the DAHPS_G•DAHP oxime crystal structures (see Chapter 3). Thus, DAHP oxime was a competitive inhibitor with respect to both PEP and E4P in subunits B and C. That is, it occupies the same physical space as both substrates, and inhibitor binding is mutually exclusive with substrate binding. Kinetically, this is seen in the ability of high substrate concentrations to abolish inhibition. In contrast, DAHP oxime did not bind to subunits A or D. Thus, DAHP oxime inhibition was noncompetitive with respect to PEP and E4P in subunits A and D. In other words, the EIS complex (i.e., DAHPS with DAHP oxime bound to subunits B and C) retained partial activity. This is supported by the residual DAHPS activity which could not be abolished even at very high [I], and the fact that the values of $K_{M,Mn}$, $K_{M,PEP}$ and $K_{M,E4P}$ were the same at high [I] as in uninhibited enzyme (Figure 2.6, Figure 2.7).

As a consequence of this half-of-sites binding by DAHP oxime, the inhibition pattern was mixed. Traditional linear plots meant to distinguish modes of inhibition (e.g., Lineweaver-Burke or Dixon plots) were not useful because inhibition was competitive with respect to two subunits and noncompetitive with respect to the other two, leading to ambiguous plots.

While the crystal structures showed that inhibition was competitive with respect to PEP and E4P (see Chapter 3), they were not informative with respect to Mn^{2+} . DAHP oxime did not occupy the metal binding site in the crystal structures, but no crystal structure was found in which both Mn^{2+} and DAHP oxime were bound to the same subunit. It is known that the metal interacts with the PEP carboxylate and it is presumed to coordinate with O1 of E4P.⁵² These interactions are still available with DAHP oxime, through the C1 carboxylate moiety and the C4 hydroxyl group. Although no crystal structure contained both Mn^{2+} and DAHP oxime in the same subunit, this cannot be taken as evidence that it does not happen in the solution phase. The question was resolved with inhibition assays. High $[Mn^{2+}]$ could completely overcome DAHP oxime inhibition (Figure 2.8), a hallmark of competitive inhibition. Thus, though Mn^{2+} and DAHP oxime did not occupy the same physical space, their binding was mutually exclusive, making DAHP oxime inhibition competitive with respect to Mn^{2+} in subunits B and C, but still noncompetitive in subunits A and D.

Previous studies of DAHPS inhibition revealed two potential complications regarding the role of metal ions in inhibition. In one study, metal ion complexation with the inhibitor rendered it ineffective,^{137,138} while in another, metal ions apparently affected the extent of inhibition.¹¹⁹ At one point, glyphosate (Figure 2.20) was thought to inhibit DAHPS,¹³⁹ however, further investigation showed that the observed inhibition was due to formation of a glyphosate• Co^{2+} complex, which effectively reduced free $[Co^{2+}]$ in solution, inactivating the

enzyme.¹³⁸ Glyphosate•metal ion interactions are mediated through carboxylate, amine and phosphonate moieties; thus, it is reasonable to consider the possibility that DAHP oxime, with its carboxylate, nitrogen atom, and phosphate groups could form similar complexes with metal ions.^{140,141} However, glyphosate•Mn²⁺ complexes did not form,¹³⁸ therefore, it is unlikely that formation of a DAHP oxime•Mn²⁺ complex is the cause of high [Mn²⁺] relieving DAHP oxime inhibition.

Other effects of metal ions on inhibition were observed with fosmidomycin (**7**, Figure 1.10) inhibition of DAHPS, though the nature of these interactions is not well understood. Fosmidomycin inhibition was competitive with respect to PEP,¹¹⁹ and the extent of inhibition depended on the identity of the metal ion. Inhibition plateaued at 45% residual activity in the presence of Mn²⁺ or Fe²⁺, but 80% with Co²⁺ as the activating metal. The authors speculated that there was an inhibitor•metal ion interaction, but did not investigate further. In the case of DAHP oxime, inhibition was observed in the slow binding experiments when DAHPS_{H6} and DAHP oxime were incubated in the absence of Mn²⁺, demonstrating that inhibitor binding was not metal ion dependant. However, no experiments were done to determine the dependence of residual activity on the identity of the metal ion.

NeuNAc oxime binding to NeuB also appeared to be mutually exclusive with metal ion binding.¹²⁴ In the crystal structures, no metal ion was found in the active site, even though the inhibitor did not occupy the metal ion-binding site.

The crystal structure of NeuB with a THI mimic inhibitor, **17** (Figure 1.11), showed that the binding of both inhibitor and metal caused a distortion of the coordination sphere of the Mn^{2+} ion. In that study, NeuB was crystallized in the presence of Mn^{2+} , then soaked with **17**. In these structures, Mn^{2+} occupancy decreased to 50%, implying a loss of affinity of the NeuB•inhibitor complex for Mn^{2+} .¹²³

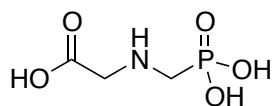


Figure 2.20: Structure of the EPSP synthase inhibitor glyphosate.

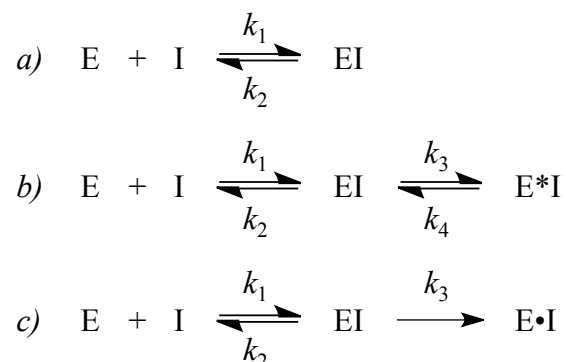
2.4.4. Slow Binding Inhibition

DAHP oxime displayed slow-binding behaviour. Slow-binding inhibitors can be classified into three categories (Scheme 2.3):^{87,102} (a) Formation of the EI complex is a slow equilibrium that is established at the time scale of minutes to hours. (b) Formation of the EI complex is fast, followed by a slow isomerization or rearrangement of EI to form a tighter E*I complex. (c) Formation of EI complex is fast followed by the formation of a covalent E-I complex.

The distinction between mechanisms (a) and (b) can be made by whether the EI complex forms without the need for preincubation at high inhibitor concentrations. Distinguishing (b) from (c), which is the covalent modification of enzyme, is based on the ability of the inhibitor to dissociate from the E*I complex, as covalent modifications are irreversible. In some cases, such as when

the enzyme is unstable and dissociation is slow, it is not possible to measure dissociation of the E*I complex even if there is no covalent bond.

Scheme 2.3: Different modes of slow binding inhibition.



Our data supported slow binding inhibition through mechanism (b). That is, initial binding of the inhibitor is followed by conformational changes in the enzyme such that a more tightly bound E*I species forms. This conversion is on the minute time scale. The ultimate dissociation constant (K_i^*) can be calculated with eq. 2.9.⁸⁷

$$K_i^* = \frac{K_i}{1 + \frac{k_3}{k_4}} \quad (2.9),$$

where $k_3 = k_{\text{on}}$ (Section 2.3.6), and $k_4 = k_{\text{off}}$ (Section 2.3.6). Applying the measured values of $K_i = 1.7 \mu\text{M}$ (Section 2.3.4), $k_{\text{on}} = 0.24 \text{ min}^{-1}$ (Section 2.3.6) and $k_{\text{off}} = 0.012 \text{ min}^{-1}$ (Section 2.3.6) to eq. 2.9 gave a K_i^* value of $81 \pm 45 \text{ nM}$. By comparison, using the incorrect value of $K_i = 13 \text{ nM}$, obtained by plugging the single substrate K_M values into eq. 2.3, gives an apparent K_i^* value of 0.6

± 0.3 nM. This value is incorrect, but is useful for comparison with literature values obtained the same way.

2.4.5. Residual rate

DAHP oxime inhibition, regardless of preincubation time, resulted in a residual rate at high inhibitor concentration that was 15% of the uninhibited rate (Figure 2.4). NeuB similarly showed incomplete inhibition, even after overnight incubation with high concentrations of NeuNAc oxime. However, if NeuNAc oxime was incubated with actively catalyzing NeuB (i.e., in the presence of substrates), complete inhibition was achieved after 6 h.¹²⁴ This was rationalized as being the result of changes in protein dynamics induced during catalysis. Proteins are dynamic molecules that continually sample numerous conformations; ligand binding and/or catalysis can expand or change the subset of conformations that are available to the protein molecule.¹⁴² In some cases certain conformations are only accessible as an intermediate in a sequential pathway in a “catalytic network” of multiple parallel and sequential pathways.¹⁴³ Complete inhibition of NeuB by NeuNAc oxime during extended catalysis could have arisen from the selective binding of the inhibitor to an enzyme conformation that is infrequently populated and accessible only during catalysis. With DAHPS_{H6}, this did not occur over the 7 h period that catalysis in the presence of DAHP oxime was monitored. Taking into account the observation that the K_M values did not change when DAHP oxime was bound, and that the crystal structures of DAHPS•DAHP

oxime showed two of four subunits occupied, we conclude that the observed residual rate arose from the two subunits to which the inhibitor did not bind. The fact that the residual rate was 15%, rather than 50%, of the uninhibited rate indicated that inhibitor binding in the remote subunits (i.e, B and C) decreased k_{cat} in the unbound subunits (i.e., A and D).

2.4.6. Cooperativity

Cooperativity describes the presence of functional interactions between subunits within multimeric or multidomain enzymes. When binding of a ligand increases the binding affinity of subsequent ligand molecules, this is positive cooperativity. When binding of a ligand molecule hinders subsequent binding the system is displaying negative cooperativity.

In the formalism of the Hill equation (eq. **2.6**) the Hill coefficient (n) is a measure of the degree of cooperativity between subunits (or domains).¹⁴⁴ It ranges from $0 < n < \text{number of binding sites}$; $n > 1$ indicates positive cooperativity, and $n < 1$ indicates negative cooperativity, while $n = 1$ indicates no interaction between subunits. The Hill equation assumes all-or-none cooperativity. For example, if $n = 2$, then the assumption is that the enzyme has no affinity for a single ligand molecule, and it only exists as E and EI_2 , but not EI . In reality, all-or-none binding is unlikely, and any binding of a single ligand molecule will be manifested by the value of n being less than the number of binding sites.

The two dominant models of cooperativity are the Monod-Wyman-Changeux (MWC) model¹⁰⁸ and the Koshland-Nemethy-Filmer (KNF) model.¹⁰⁷ The MWC model is a symmetric model which requires all subunits to assume an identical conformation. In this model the enzyme exists in a high affinity and a low affinity state with respect to ligand binding. Ligand binding to one binding site causes all binding sites to switch from low to high affinity, an all-or-nothing response. The KNF model is a sequential binding model where ligand binding at one site affects, either positively or negatively, ligand binding at neighbouring sites. Both models assume rapid equilibria between the different enzyme conformations. Under these assumptions, the Hill coefficient, n , will approach the number of binding sites in a highly cooperative system, but cannot exceed it. Only in the presence of strong cooperativity can n equal the number of binding sites.

The MWC model failed to explain our data on two counts: (a) asymmetry of the tetramer, and (b) the presence of negative cooperativity. (a) The MWC model requires that all subunits be in the same conformation, either all low-, or all high-affinity. This was not observed; inhibitor-bound subunits (subunits B and C) had different conformations from subunits A and D (Chapter 3). Treating DAHPS as a dimer of dimers, in which each dimer follows the MWC model, also does not work because in some structures, subunit D had a different conformation than subunit A (Chapter 3). (b) In the MWC model ligand binding induces a high affinity conformation. As such, it cannot explain the negative cooperativity

observed within the tight dimers where binding of DAHP oxime to subunit B (or C) prevented binding to subunit A (or D).

The KNF model describes cooperativity in terms of sequential ligand binding. It allows different subunits to be in different conformations, and allows for negative cooperativity. Under the KNF model, cooperativity is a function of ligand binding, equilibrium of conformational states, and an equilibrium constant describing the interaction of neighbouring subunits. In this model, the monomers of a tetrameric protein exist in equilibrium (K_t) between conformations α and β . Ligand (L) binds to conformation β , locking the subunit into conformation β . The favourability of subsequent ligand binding is dependent on interactions between neighbouring subunits. If $\beta:\beta$ interactions are energetically favourable, then the equilibrium of the system will be pushed toward the ligand-bound β state, and will exhibit positive cooperativity. If $\beta:\beta$ interactions are unfavourable, then subsequent ligand binding will be unfavourable and the system will display negative cooperativity. The KNF model described our observations better than the MWC model, but it does not account for the slow equilibrium for the onset of cooperativity.

Fitting the concentration dependence for slow-binding inhibition directly to the Hill equation (eq. 2.6) gave a poorly defined value for n . Using a linearized form of the Hill equation (eq. 2.7) gave an $n = 4.65$ (Figure 2.11), which, in turn, gave a reasonable fit to the data when used in the Hill equation. This would imply that at least 5 (≈ 4.65) inhibitor molecules bind cooperatively to DAHPS in a KNF

model. Gel filtration (Figure 2.16) and cross-linking (Figure 2.17) experiments failed to provide evidence for higher oligomers of DAHPS beyond the normally observed tetramer, and the DAHPS:DAHP oxime crystal structures demonstrated that only two inhibitor molecules bound per tetramer. One important limitation of the KNF model of cooperativity (and any experimental Hill coefficient based on that model) is that it assumes that all enzyme conformations are at equilibrium with each other, which is not necessarily true for slow-binding inhibition.

Sigmoidal concentration dependences, a signature of cooperativity, have been observed in some monomeric enzymes.¹⁴⁵ This is frequently thought of as a signature of multimeric enzymes. In monomeric systems, the observed cooperativity is a manifestation of the slow interconversion of enzyme conformations that have different intrinsic rate constants.¹⁴⁵ In these systems, enzymes can exist in slowly interconverting conformations, E and E', each of which can catalyze the reaction at different rates, with the proportion of each species being influenced by the substrate concentration. Assuming E' is the lower populated, higher rate species, increasing substrate concentration would shift the enzyme population toward E' and cooperativity would be observed.

In order to rationalize the observed extreme cooperativity of DAHP oxime inhibition of DAHPS_{H6}, we posit a contribution from the slow-binding nature of the inhibitor. It is possible that if the dissociation of E*•I to E* + I is faster than the relaxation of E* to E, then one oxime molecule can interact with more than

one DAHPS_{H6} and shift the equilibrium between E and E* toward E*. This could potentially yield an n value greater than the number of binding sites (Figure 2.21).

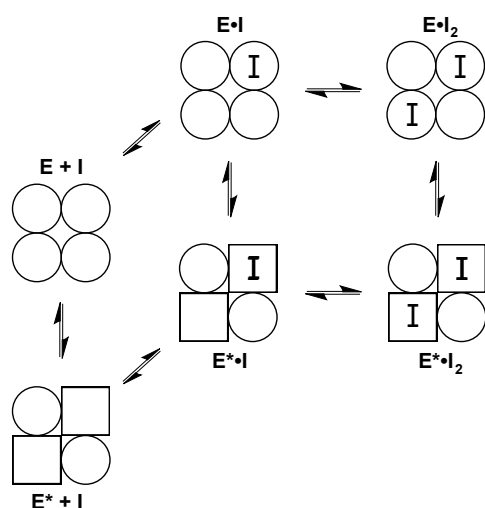


Figure 2.21: Thermodynamic box of inhibitor binding and conformational change.

In this model, unbound enzyme exists in two distinct forms with respect to inhibitor binding, E and E*, where E* has higher affinity for DAHP oxime. In the absence of inhibitor, the equilibrium favours E over E*. Initially, DAHP oxime binds E to form EI and subsequently EI to form EI₂. Both binding events are rapid equilibria, as fast-binding inhibition is observed.

At lower inhibitor concentrations, slow binding and cooperativity are observed as the EI isomerizes to E*I, which, because of its higher affinity for the inhibitor, is quickly converted to E*I₂. E* has a higher affinity for I than E, as seen by the onset of cooperativity. k_{on} for this transformation, that is, the conversion of EI to E*I₂, was measured to be 0.24 min^{-1} . Similarly the dissociation of E*I₂ to EI was slow, $k_{\text{off}} = 0.012 \text{ min}^{-1}$.

When I is bound, E*, with higher affinity for DAHP oxime accumulates. Given the initial low concentration of E* and the slow formation of E* in the presence of inhibitor, it is reasonable to expect E* relaxation to E will be a similarly slow process. Under this condition, provided that the relaxation of E* to E is slow, one molecule of DAHP oxime can dissociate from the E*I complex and rebind another molecule of E before E* relaxes to E. Thus, one inhibitor molecule is interacting with more than one DAHPS_{H6} molecule, and as a result $n > 4$ is observed.

Attempts to model this mechanism via numerical simulations (using Dynafit software by BioKin Ltd.) (Simulations were run by Dr. Berti) did not reproduce the experimental data. From the simulation we noted that the system must not be at equilibrium for n to be greater than the number of subunits.

An overall picture of DAHPS inhibition by DAHP oxime has emerged, even if not all the details have been explained. In fast-binding inhibition, DAHP oxime binds quickly to subunits B and C of DAHPS (Figure 2.22A). There is no apparent cooperativity between subunits B and C, but strong negative cooperativity within the tight dimers A•B and C•D. Since no cooperativity was observed in the fast-binding step, the K_i 's were the same for subunits B and C.

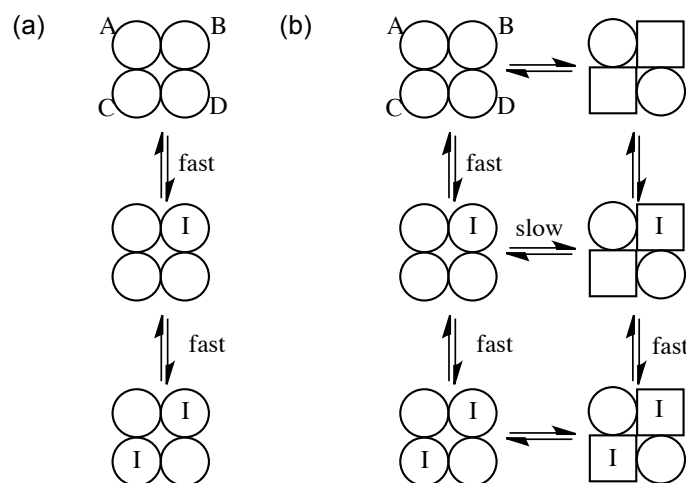


Figure 2.22: Schematic representation of oxime binding.

(a) Fast binding of DAHP oxime to DAHPS_{H6} with no preincubation. (b) The transition from a weakly bound DAHPS_{H6}•DAHP oxime complex to a tightly bound DAHPS_{H6}•DAHP oxime complex induces strong cooperativity, which makes binding of the second oxime molecule highly favourable.

Preincubation of DAHPS_{H6} with DAHP oxime demonstrated a slow-binding phase to inhibition. Slow-binding inhibition is generally characterized as involving an initial, fast inhibitor binding step to form a weak E•I complex, followed by a slow conformational change into a tighter binding form, E*•I (Scheme 2.3)¹⁰². In the case of DAHPS_{H6}, there was a fast binding step with $K_i = 1.7 \mu\text{M}$ and no apparent cooperativity, followed by a slower step with strong cooperativity (Figure 2.22B). This conformation is accompanied by strong positive cooperativity in binding the second DAHP oxime molecule (Figure 2.22C). It is not known if this cooperativity originates between the dimers A•B and C•D, or if it arises from direct interactions between subunits B and C alone. The strong negative cooperativity between subunits A and B and subunits C and D remains, as residual activity could not be eliminated at high inhibitor concentrations.

The source of negative cooperativity is not clear. From the crystal structure, DAHP oxime-bound DAHPS_{H6} adopted a similar conformation to PEP-bound DAHPS_{H6}. PEP binding is known to be cooperative,^{35,146} and crystal structures with all four subunits containing PEP have been solved.^{54,55,136} Also, DAHP oxime binding to subunit B(C) prevented oxime binding to subunit A(D); however, the substrate K_M values for subunit A(D) were unaffected (Figure 2.6, Figure 2.7). Although k_{cat} for subunits A and D decreased in the DAHP oxime-bound complex, they were catalytically competent.

Chapter 3 - X-ray Crystallography

3.1. Introduction

X-ray crystallographic structures of enzymes with substrates, products and inhibitors give insight into binding sites, potential binding contacts, and insights into catalytic mechanisms. For example, X-ray crystallography was invaluable in early mechanistic studies of serine proteases.¹⁴⁶ Although distant in the primary sequence, in the folded protein, Asp102, His57 and Ser195 are situated in close proximity to each other allowing for a network of hydrogen bonding interactions.¹⁴⁷ Ser195-OH hydrogen bonded to His57, which further interacted with Asp102, effectively increasing the nucleophilicity of the catalytic serine residue. This arrangement of the three residues has become to be known as the “active site triad” and is a common feature of all serine proteases.¹⁴⁸

The study of HIV/AIDS benefitted from crystallography in that the first structures of HIV protease provided insight in to the structure of a drug candidate in AIDS therapy.^{149,150} These structures revealed the structure of HIV protease to be a dimer with a single active site. The crystal structure, along with homology analysis and inhibition studies, helped classify HIV protease as an aspartic protease. Although the exact mechanism employed by HIV protease is not known, inhibitor-bound structures have led to the proposal of a concerted hydrolytic mechanism where the nucleophile water and acidic proton on one of the catalytic aspartic acid residues attacks the scissile bond in a single step.^{151,152} This proposed mechanism for HIV protease is different than the mechanism

proposed for other aspartic proteases where nucleophilic attack by a water molecule takes place prior to protonation of the scissile amide.¹⁵³

In this study we outline the use of X-ray crystallography to study DAHP oxime binding to DAHPS_G. We report seven unique structures of DAHPS_G, including a new 2-fold symmetry that reveals inhibitor binding in half of the binding sites.

3.2. Materials and Methods

3.2.1. Construction of a TEV-cleavable N-terminal His₆-tagged DAHPS:

DAHPS_{H6-TEV}

A Tobacco Etch Virus (TEV) protease-cleavable N-terminally His₆-tagged version of *aroG*, the Phe-sensitive isozyme of *E. coli* DAHPS, DAHPS_{H6-TEV}, was constructed utilizing the Gateway cloning strategy (Invitrogen). TEV cleavage of DAHPS_{H6-TEV} yielded wild-type DAHPS with a one amino acid (Gly) N-terminal extension: DAHPS_G (Figure 3.1).

```

          6x His tag                               TEV sequence
atgcatcatcatcatcatcacatcacagaagtttgtacaaaaaagcaggcttcgaaaacctg
M H H H H H H I T S L Y K K A G F E N L

tattttcaggcatgaattatcagaacgacgatttacgcatcaagaatcaagagtta
Y F Q G M N Y Q N D D L R I K E I K E L

cttcctcctgtgcattgctggaaaaattccccgctactgaaaatgccggaatacggtt
L P P V A L L E K F P A T E N A A N T V

gcccatgccgaaaagcgatccataagatcctgaaaggtaatgatgatcgccctgttggtt
A H A R K A I H K I L K G N D D R L L V

gtgattggccatgctcaattcatgatcctgtcgcggcaaaagagtatgccactcgttg
V I G P C S I H D P V A A K E Y A T R L

ctggcgctgcgtgaagagctgaaagatgagctggaaatcgtaatgcgcgtctattttgaa
L A L R E E L K D E L E I V M R V Y F E

aagccgctaccacgggtgggctggaaaggctgattaacgatccgcatatggataatagc
K P R T T V G W K G L I N D P H M D N S

ttccagatcaacgacggctcgcgtatagcccgtaaattgctgctgatattaacgacagc
F Q I N D G L R I A R K L L L D I N D S

ggctcgcagcggcagggtgagtttctcgatgatcaccacacaatatctcgcgtgacctg
G L P A A G E F L D M I T P Q Y L A D L

atgagctggggcgcaattggcgacgtaccaccgaatcgaggtgcaccggaactggca
M S W G A I G A R T T E S Q V H R E L A

tcagggttttctgtccggctcggttcaaaaatggcaccgacggtacgattaagtggct
S G L S C P V G F K N G T D G T I K V A

atcgatgccattaatgccgccggtgcgccactgcttcctgtccgtaacgaaatggggg
I D A I N A A G A P H C F L S V T K W G

cattcggcgattgtgaataccagcggtaacggcgattgccatattcattctcgcggcggt
H S A I V N T S G N G D C H I I L R G G

aaagagcctaactacagcgcgaagcacgttgctgaagtgaagaagggtgaacaagca
K E P N Y S A K H V A E V K E G L N K A

ggcctgcagcacagggtgatgatcattcagccatgctaactcgtccaaacaattcaaa
G L P A Q V M I D F S H A N S S K Q F K

aagcagatggatggtgtgctgacgtttgccagcagattgccgggtggcgaaggccatt
K Q M D V C A D V C Q Q I A G G E K A I

attggcgtgatggtggaagccatctggtggaaggcaatcagagcctcagagcggggag
I G V M V E S H L V E G N Q S L E S G E

ccgctggcctacggtaagagcatcaccgatgcctgcacgctggggaagataccgatgct
P L A Y G K S I T D A C I G W E D T D A

ctgttacgtcaactggcgaatgcagtaaaagcgcgtcggggtaa
L L R Q L A N A V K A R R G -

```

Figure 3.1: Sequence of His₆-tagged, TEV protease cleavable DAHPS, DAHPS_{H6-TEV}. DNA and peptide sequence of the TEV protease cleavable *N*-terminally His₆-tagged DAHPS construct. TEV protease cleavage occurs at the Q↑G bond of the TEV protease recognition sequence (ENLYFQ↑G). Upon cleavage, DAHPS_G is liberated, i.e. DAHPS with an additional *N*-terminal glycine residue.

The *aroG* gene was PCR amplified from the *aroG*:pCA24N plasmid^{154,155} (provided by Dr. Eric Brown, Department of Biochemistry and Biomedical Sciences, McMaster University), using Pfu polymerase and the PCR conditions in Figure 3.2. The forward primer (5'-GGGG ACA AGT TTG TAC AAA AAA GCA GGC TTC GAA AAC CTG TAT TTT CAG GGC *ATG AAT TAT CAG AAC GAC GAT TTA CGC*-3') contained the TEV protease cleavage site (bold) between the *aatB* restriction site (underlined) and the *aroG* gene (italics). The reverse primer (5'-GGG GAC CAC TTT GTA CAA GAA AGC TGG GTC TTA CCC GCG ACG CGC TTT TAC TGC ATT CG-3') contained the *aatB* site (underlined) and the *aroG* gene (italics). The PCR product was run on a 1% agarose gel and purified using the QIAquick Gel Extraction Kit (Qiagen). Purified DNA was quantified by UV spectroscopy and used in a BP clonase recombination reaction with the pDONR221 entry vector for 1 h. The BP clonase recombination reaction (1 μ L) was transformed into *E. coli* Top10 cells and plated onto an LB/agar plate containing 50 μ g/mL kanamycin, and incubated overnight at 37 °C. The resulting colonies were grown overnight in LB media containing 50 μ g/mL kanamycin. Plasmid DNA was isolated using a QIAprep spin miniprep kit (Qiagen). The plasmid was confirmed by PCR to contain the *aroG* gene, then used in LR clonase recombination reaction for 1 h using the pET300/NT-DEST destination vector, which carries an *N*-terminal His₆ tag. The LR clonase recombination reaction (1 μ L) was transformed into *E. coli* Top10 cells and plated onto an LB/agar plate containing 100 μ g/mL ampicillin. Colonies were grown in

LB with 100 $\mu\text{g/mL}$ ampicillin; the plasmid was isolated and sequenced. The same strategy was used to introduce a TEV cleavage site into *E. coli* DAHP synthases *aroH* and *aroF*, *E. coli* KDO8PS and *C. jejuni* KDO8PS.

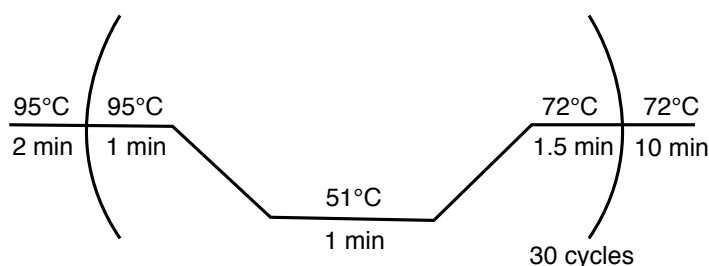


Figure 3.2: Thermal cycling parameters for Gateway cloning.

3.2.2. Purification of TEV-cleavable His₆-tagged DAHPS(Phe): DAHPS_{H6-TEV}

DAHPS_{H6-TEV} in the pET300/NT-DEST plasmid was transformed into chemically competent *E. coli* BL21*(DE3) cells and grown overnight at 37 °C on LB/agar plate containing 100 $\mu\text{g/mL}$ ampicillin. A single colony was inoculated into 50 mL LB medium with 100 $\mu\text{g/mL}$ ampicillin and cultured overnight at 37 °C. The 50 mL overnight culture was added into 1 L LB medium with 100 $\mu\text{g/mL}$ ampicillin, and grown at 37 °C to OD₆₀₀ = 0.6. DAHPS_{H6-TEV} expression was induced with 0.3 mM IPTG at 37 °C for 4 h. Cells were harvested by centrifugation at 8000 \times g for 20 min at 4 °C. All subsequent steps were performed at 4 °C. Cells were re-suspended in 15 mL of buffer A (50 mM Tris-Cl, pH 7.5, 150 mM NaCl, 50 mM imidazole, 1 mM phenylmethylsulfonyl fluoride) and lysed by passage through EmulsiFlex-C5 High Pressure Homogenizer at 10,000 psi. Cell debris was removed by centrifugation for 30 min at 10,000 \times g. DAHPS_{H6-TEV} was purified by nickel affinity chromatography

on a 1 mL HiTrap chelating column (GE Healthcare) that was charged with 5 column volumes of 100 mM nickel sulfate. DAHPS_{H6-TEV} was eluted with buffer B (50 mM Tris-Cl, pH 7.5, 150 mM NaCl, 500 mM imidazole), and was homogeneous as judged by SDS-PAGE.. The His₆ tag was removed by treating DAHPS_{H6-TEV} with TEV protease in a 4:1 (DAHPS_{H6-TEV}:TEV) molar ratio in elution buffer at 4 °C overnight, with 1 mM EDTA, 1 mM DTT, and 10% glycerol (v/v) added. The cleavage reaction was then buffer exchanged into 20 mM Tris-Cl, pH 7.5, and run through a 1 mL nickel-charged metal affinity column to remove uncleaved DAHPS_{H6-TEV}, TEV, and the cleaved His₆-tag. The protein was concentrated, and the concentration was determined from the A₂₈₀ using the Edelhoch et al. method.^{126,127}

3.2.3. Purification of TEV Protease

TEV protease gene in pRK793 vector was provided by Dr. Murray Junop (Department of Biochemistry and Biomedical Sciences, McMaster University). TEV protease was expressed and purified essentially as described above. It was purified using nickel affinity chromatography similarly to DAHPS_{H6-TEV}, but buffers A and B contained 10% glycerol, and the pH was 8. Purified TEV protease was buffer exchanged into storage buffer (50 mM Tris-Cl, pH 8, 150 mM NaCl, 1 mM EDTA, 2 mM DTT and 5% glycerol) and flash frozen with an ethanol/dry ice bath.

3.2.4. Crystallography

DAHPS_G and DAHP oxime were co-crystallized using the hanging drop vapour diffusion method using the conditions described (Table 3.1). All crystals were grown at 4 °C over 500 µL of 2 M ammonium sulphate. All crystals were diffracted at the National Synchrotron Light Source at Brookhaven National Laboratory by Dr. Murray Junop. The data was indexed, scaled and merged using HKL 2000 software.¹⁵⁴ Crystal structures were solved by molecular replacement using AutoMR from Phenix crystallographic software¹⁵⁶ with a published *E. coli* DAHPS structure (PDB code: 1KFL) as the search model.⁵⁵ Structure refinement was carried out with WinCoot¹⁵⁷ and Phenix refine.

3.3. Results

DAHPS_G•DAHP oxime crystals that were obtained diffracted with resolutions down to 1.65 Å (Table 3.2). All but one crystal was obtained from essentially the same crystallization conditions, 0.2 M tri-lithium citrate, 20% (w/v) PEG 3350, with the main difference being the additives used (Table 3.1). The structures contained one to four tetramers per asymmetric unit. Wild-type DAHPS appears to occur only as a tetramer in solution,¹³¹ so the higher oligomeric forms observed in the asymmetric units are unlikely to have any biological significance. Three structures contained no bound inhibitor, while four contained two DAHP oxime molecules per tetramer, bound to subunits B and C. One structure had incomplete inhibitor occupancy in subunit B, but was otherwise similar to the other inhibitor-bound structures. There was no electron density

visible for the *N*-termini; the first amino acids visible was D6, D7, or L8, depending on the structure. All inhibitor-bound subunits were in the "closed" conformation, as were subunits in some of the inhibitor-free structures. Most unbound subunits in inhibitor-containing structures (i.e., subunits A and D) were in the "open" conformation, while some unbound subunits D were in a "hybrid" conformation that possessed features of both open and closed conformations. The different conformations were very similar to each other, with conformational changes largely restricted to four loops (see below).

Table 3.1: Crystallization conditions used in this study.

DAHPS_G (10 mg/mL) was prepared in 20 mM Tris-Cl, pH 7, with 0.1 mM TCEP and appropriate substrates/inhibitor. Each drop contained protein sample with crystallization buffer (0.2 M trilithium citrate tetrahydrate, 20% (w/v) PEG 3350, unless noted) and additive in the outlined ratios.

Structure (resolution)	Additive	Substrate/Inhibitor	Drop ratio ^a
Wai003_4_10 (1.83 Å)	30% (w/v) D-(+)-glucose monohydrate	1 mM DAHP oxime	6:4:1
101_4_9 ^c (1.65 Å)	30% (w/v) D-(+)-glucose monohydrate	1 mM DAHP oxime	8:2:1
101_3_15 ^c (1.95 Å)	30% (w/v) D-(+)-glucose monohydrate	1 mM DAHP oxime	8:2:1
MJ106_2_3 ^c (1.95 Å)	30% (v/v) 2-propanol	1 mM DAHP oxime	1:1:0.2
MJ106_3_8 ^c (2.00 Å)	40% (v/v) 1,4-butanediol	1 mM DAHP oxime	1:1:0.2
MJ109_2_7 ^b (2.42 Å)	30% (v/v) ethylene glycol	1 mM DAHP oxime	1:1:0.2
MJ109_1_11 (2.00 Å)	0.1 M praseodymium(III) acetate hydrate	1 mM DAHP oxime	1:1:0.2
MJ110_4_7 (1.90 Å)	30% (v/v) ethylene glycol	1 mM DAHP oxime (crystals soaked with 8 mM DAHP oxime)	1:1:0.2
RS7_4_13 (2.12 Å)	30% (w/v) D-(+)-galactose	5 mM DAHP oxime	1:1:0.2
Wai003_3_5 ^c (2.13 Å)	30% (v/v) ethylene glycol	5 mM DAHP oxime	1:1:0.2
RS7_1_5 (1.94 Å)	30% (v/v) ethylene glycol	1 mM DAHP oxime (crystals soaked with 8 mM DAHP O-(2-fluoroethyl)oxime)	1:1:0.2
MJ108_1_7 (2.29 Å)	30% (w/v) D-(+)-galactose	5 mM E4P, 5 mM PEP	1:1:0.2
MJ108_2_25 ^c (3.1 Å)	30% (v/v) 2-propanol	5 mM DAHP oxime, 5 mM PEP, 5 mM Phe	1:1:0.2
MJ200_6_9 ^c (1.97 Å)	30% (v/v) 2-propanol	5 mM DAHP oxime, 5 mM PEP, 5 mM Phe	1:1:0.2
MJ110_2_5 (1.97 Å)	30% (v/v) ethylene glycol	5 mM DAHP oxime, 5 mM PEP, 5 mM E4P	1:1:0.2

^a Volume ratio of protein solution:crystallization buffer:additive. The inhibitor/substrates/Phe were added to the protein solution in the indicated concentrations beforehand.

^b Crystallization buffer was 100 mM imidazole, pH 8, 0.2 M Lithium sulfate, 10% (w/v) PEG 3000.

Table 3.2: X-ray data collection and refinement statistics of unique DAHPS_G structures.

Data for the highest resolution shell is presented in parentheses.

	Wai003_4_10	MJ109_2_7
	DAHPS _G •DAHP oxime ₂	(DAHPS _G) ₂
Data collection		
Wavelength (Å)	1.1	1.1
space group	C2	P1
unit cell parameters		
a, b, c, (Å)	211.0, 53.5, 150.9	53.2, 107.9, 142.7
α, β, γ, (deg)	90.0, 115.4, 90.0	102.7, 100.4, 104.3
no. of molecules per asymmetric unit	4	8
resolution range (Å)	50 - 1.83 (1.86 - 1.83)	50-2.42 (2.46-2.42)
no. of unique reflections	132804	107663
data redundancy	3.1 (2.8)	1.9 (1.9)
completeness (%)	97.2 (98.1)	96.2 (95)
I/σ(I)	18.3 (2.7)	10.33 (1.89)
R _{merge} (%)	5.2 (38)	7.3 (38.8)
Model and Refinement		
resolution range (Å)	32.26-1.81 (1.88-1.81)	46.07-2.40 (2.49-2.40)
R _{work} (%)	0.1908	0.1989
R _{free} (%)	0.2296	0.276
no. of reflections	125405	98549
cutoff criterion [(F _{obs} /σF _(obs))]	0.07	0.09
no. of amino acid residues/atoms	1376/11355	2756/21193
no. of ligand/ion atoms	4	0
rmsd for bond lengths (Å)	0.007	0.008
rmsd for bond angles (°)	1.009	1.105
average B factor (Å ²)	31	48.6

	MJ109_1_11	RS7_1_5
	(DAHPS _G •Mn ²⁺ ₄ •SO ₄ ²⁻) ₂ • (DAHPS _G •Mn ²⁺ ₃ •SO ₄ ²⁻) ₂	DAHPS _G • DAHP oxime ₂
<hr/>		
Data collection		
Wavelength (Å)	1.1	1.1
space group	P1	C2
unit cell parameters		
a, b, c, (Å)	106.6, 108.3, 144.2	209.8, 53.5, 149.6
α, β, γ, (deg)	71.6, 79.1, 75.9	90.0, 115.5, 90.0
no. of molecules per asymmetric unit	16	4
resolution range (Å)	50-2.0 (2.03-2.00)	50.00-1.95 (1.98- 1.95)
no. of unique reflections	366760	102957
data redundancy	1.9 (1.8)	2.8 (2.4)
completeness (%)	92.3 (87.2)	93.4 (85.7)
I/σ(I)	12.5 (1.8)	14.6 (2.2)
R _{merge} (%)	5.7 (36.1)	6.0 (43.7)
<hr/>		
Model and Refinement		
resolution range (Å)	46.50-2.00 (2.08-2.00)	43.19-1.94 (2.01- 1.94)
R _{work} (%)	0.1975	0.2005
R _{free} (%)	0.2545	0.2541
no. of reflections	238410	98915
cutoff criterion [(Fobs/σF(obs)]	0.05	0.06
no. of amino acid residues/atoms	0/45608	1376/11371
no. of ligand/ion atoms	16/14	2
rmsd for bond lengths (Å)	0.007	0.007
rmsd for bond angles (°)	1.055	1.055
average B factor (Å ²)	33.7	35.53

	RS7_4_13	MJ110_4_7
	DAHPS _G •DAHP oxime ₂	DAHPS _G
Data collection		
Wavelength (Å)	1.1	1.1
space group	C2	C2
unit cell parameters		
a, b, c, (Å)	210.0, 53.4, 150.7	211.1, 53.2, 151.3
α, β, γ, (deg)	90.0, 115.4, 90.0	90.0, 115.4, 90.0
no. of molecules per asymmetric unit	4	4
resolution range (Å)	50.00-2.12 (2.16-2.12)	50.00-1.90 (1.93-1.90)
no. of unique reflections	85303	117561
data redundancy	3.7 (3.6)	3.2 (3.1)
completeness (%)	99.9 (100)	97.9 (97.6)
I/σ(I)	12.8 (3.3)	9.7 (3.6)
R _{merge} (%)	9.3 (40.6)	8.3 (29.0)
Model and Refinement		
resolution range (Å)	40.78-2.12 (2.19-2.12)	32.26-1.89 (1.96-1.89)
R _{work} (%)	0.1761	0.1926
R _{free} (%)	0.2316	0.2451
no. of reflections	81691	109438
cutoff criterion [(F _{obs} /σF _(obs))]	0.15	0.08
no. of amino acid residues/atoms	1382/11397	1381/11711
no. of ligand/ion atoms	2	0
rmsd for bond lengths (Å)	0.007	0.007
rmsd for bond angles (°)	1.028	1.028
average B factor (Å ²)	30.6	36.9

	MJ108_1_7	MJ110_2_5
	DAHPS _G •Mn ²⁺ ₂ •PEP ₂ •P _{i2}	DAHPS _G •PEP ₄ •Lig ₂
<u>Data collection</u>		
Wavelength (Å)	1.1	1.1
space group	C2	C2
unit cell parameters		
a, b, c, (Å)	210.19, 52.9, 150.48	210.72, 53.18, 150.37
α, β, γ, (deg)	90.0, 115.7, 90.0	90.0, 115.8, 90.0
no. of molecules per asymmetric unit	4	4
resolution range (Å)	50.0-2.3 (2.34-2.3)	50-1.98 (2.01-1.98)
no. of unique reflections	67094	105376
data redundancy	3.7 (3.4)	3.6 (3.6)
completeness (%)	99.8 (99.5)	99.8 (99.8)
I/σ(I)	14.8 (3.6)	17.7 (3.2)
R _{merge} (%)	8.7 (33.7)	5.8 (40.8)
<u>Model and Refinement</u>		
resolution range (Å)	43.44-2.30 (2.38-2.30)	43.48-1.97 (2.04-1.97)
R _{work} (%)	0.1620	0.1853
R _{free} (%)	0.2288	0.2319
no. of reflections	63928	100847
cutoff criterion [(Fobs/σF(obs))]	0.14	0.09
no. of amino acid residues/atoms	1372/11432	1371/11653
no. of ligand/ion atoms	2/0	6/0
rmsd for bond lengths (Å)	0.007	0.007
rmsd for bond angles (°)	1.061	1.053
average B factor (Å ²)	27.98	37.43

3.3.1. DAHPS_G•DAHP Oxime Structure

The DAHPS_G•DAHP oxime crystal structures revealed DAHP oxime bound in two of the four active sites of each tetramer, in subunits B and C (

Figure 3.3). All previously published structures of DAHPS(Phe) had four identical subunits with one PEP (or 2-phosphoglycolate) molecule bound per subunit, in addition to divalent cations and/or the allosteric inhibitor, phenylalanine.^{54,55,136,158}

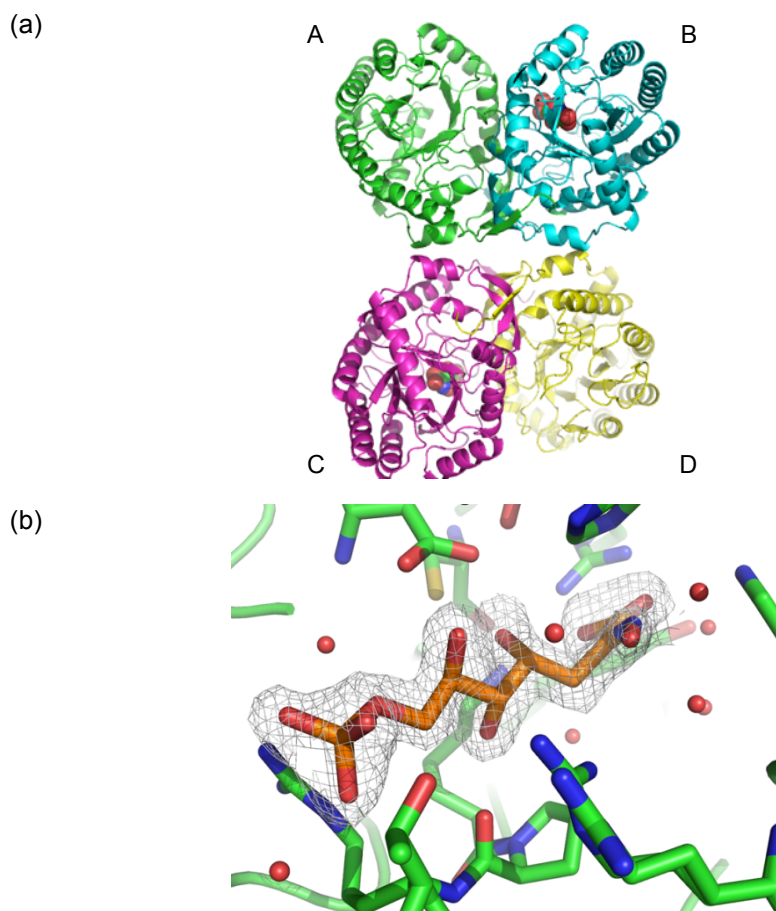


Figure 3.3: DAHPS_G•DAHP oxime crystal structure from Wai003_4_10.

(a) Ribbon diagram of DAHPS_G•DAHP oxime structure Wai003_4_10, with inhibitor molecules bound to subunits B and C shown as spheres. Subunits are displayed from left to right A/B on the top dimer and C/D on the lower dimer. (b) DAHP oxime (orange carbon atoms) in the active site with its density map at the 1 σ level overlaid.

Seven structures of DAHPS_G•DAHP oxime crystallized in the presence of 1 mM DAHP oxime were solved in this study. Two structures of DAHPS_G•DAHP oxime were crystallized in the presence of 5 mM DAHP oxime (Table 3.1). The highest resolution structure was 101_4_9, with 1.65 Å resolution. However the overall density map of Wai003_4_10, at 1.83 Å resolution, was superior with respect to DAHP oxime density. Comparing bound subunits B and C to the unoccupied subunits A and D revealed that the backbones of subunits A/D were nearly identical to each other, and subunits B/C are nearly identical to each other (Table 3.3). In fact, subunits A/D were very similar to B/C except in four regions: D6-E12, F95-K105, G188-T192, and L312-L318. C α alignment of the subunits excluding the variable loops shows that all subunits are similar to each other. When C α of the variable loops are aligned, the differences between A/D and B/C became apparent. The numbers in Table 3.3 underestimate the true variability of the variable loops as there were numerous residues without visible electron density in the variable loops that were not included in the alignment.

In Wai003_4_10, subunit B had the lowest B-factors. B-factors (also called temperature factors) are a measure of how well-defined the electron density of an atom is. Low B-factors indicate well-defined electron density, while high B-factors can indicate static or dynamic disorder in the structure. As the distance increases from the B subunit, the B-factors increased. Subunit C, which bound the second inhibitor molecule, had similar B-factors to the unbound subunits A

and D (Figure 3.4). It is interesting that inhibitor binding did not affect B-factors with respect to both subunits, suggesting that B-factors were determined primarily by packing forces.

Table 3.3: Structural alignment of subunits within the Wai003_4_10 tetramer: Root mean square deviation (rmsd) of C α atoms.

		rmsd difference in C α positions (Å)				
		non-variable region				
		Subunit →	A	B	C	D
variable region	A			0.40	0.43	0.27
	B		1.83		0.23	0.37
	C		1.95	0.30		0.43
	D		0.45	1.94	2.00	

Each subunit of the DAHPS_G•DAHPOxime cocrystal structure Wai003_4_10 was aligned with every other subunit through its C α atoms, using the "superimpose" command in Pymol. The structural alignment used all the amino acids in the "non-variable" parts of the structure, comprising 91% of the structure: I13-Y94, G106-N187, I193-S311, A319-G350. The four variable region peptides (D6-E12, F95-K105, G188-T192, and L312-L318) were excluded from the structural alignment calculations, but rmsd values were calculated based on the alignment of the non-variable regions. The rmsd values for the variable regions underestimate the true structural variability, as there was no electron density for part of every peptide in at least one subunit, except for G188-T192.

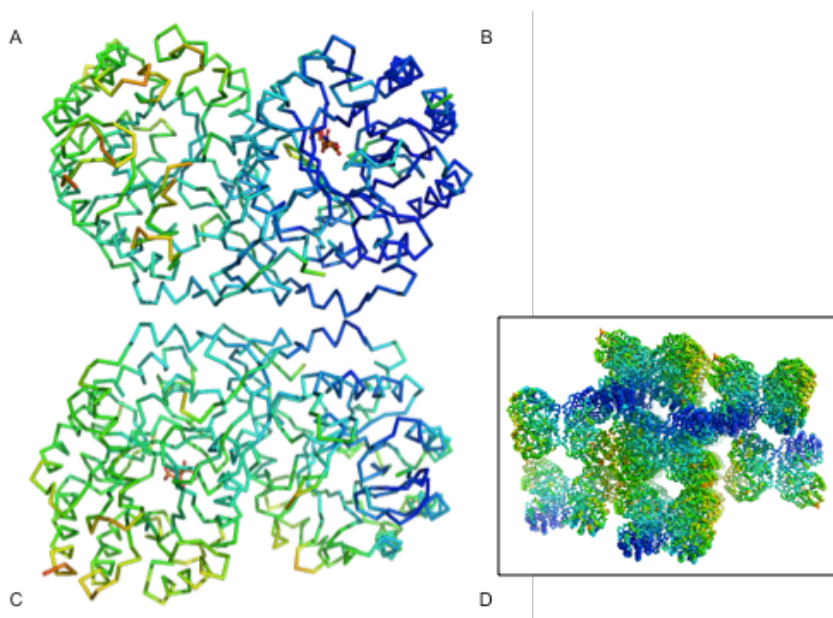


Figure 3.4: R-factors in the DAHPS₆•DAHP oxime structure, Wai003_4_10.

Subunits are displayed from left to right A/B on the top dimer and C/D on the lower dimer. B-factors are coloured from low (blue, 9 Å²) to high (red, 77 Å²). Subunit B had the lowest temperature factors with the B-factors increasing as distance increases away from subunit B. Subunit C, which contained DAHP oxime, had higher B-factors than subunit B. Boxed figure shows the packing of DAHPS₆.

The following loops displayed significant changes in conformation and/or unordered stretches of peptide: D6-E12, F95-K105, G188-T192, L312-L318. D16-E12 extended across the tight-dimer interface to interact with the other subunit. F95-K105 formed the "bottom" of the active site, and is part of the tight-dimer interface. The G188-T192 peptides from the subunits in each tight-dimer pair were close to each other, but only made indirect contact through water molecules. L312-L318 was "above" the active site, and solvent exposed (Figure 3.5). In many of the structures, the L312-318 peptide was disordered, with no electron density visible. The most dramatic shift occurred in the loop F95-K105, which made up part of the active site, and which moved from towards the active site and became more ordered upon DAHP oxime binding. In the DAHP oxime-

bound structure, the loop assumed a conformation similar to the substrate-bound conformations previously reported. We refer to this as the "closed" conformation, as the loop closes around, and binds to, the terminal phosphate group (corresponding to the phosphate of E4P), though there is still significant solvent exposure to one side of the inhibitor molecule. All inhibitor-bound subunits adopted the closed conformation. There were no significant differences between DAHP oxime-bound subunits and those structures in the literature with bound metal ions and/or PEP. Most subunits without bound DAHP oxime adopted an "open conformation". The F95-K105 loop moved away from the active site in the open conformation, exposing the terminal phosphate to bulk solvent. In many open structures, there was missing electron density in the F95-K105 loop. In addition, residue K97, the residue that is believed to coordinate the carbonyl oxygen of C1,⁵² moved into the active site, barring DAHP oxime binding. A similar open-type conformation was observed in a DAHP₄•Mn₄•PEP₄•Phe₄ structure that contained the allosteric inhibitor, phenylalanine.⁵⁴ In the unbound subunits this region was frequently disordered, particularly from residues 99-103.

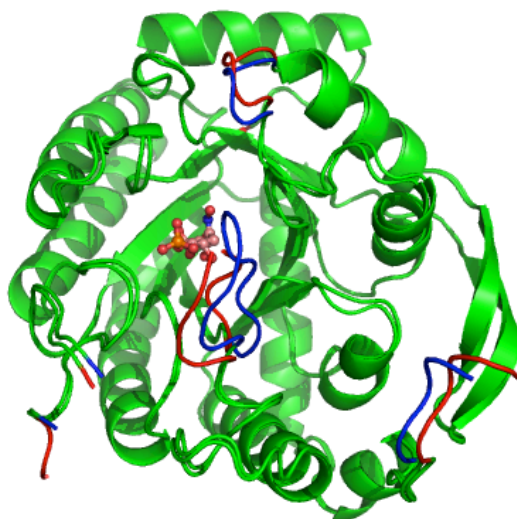


Figure 3.5: Alignment of DAHPS_e subunits C and D from the DAHP oxime-bound structure Wai003_4_10.

Aligned residues are coloured green. The variable loops are coloured blue for subunit C and red for subunit D. Variable loops include D6-E12, F95-K105, G188-T192 and L312-L318, as described in Figure 3.4.

Structure Wai003_4_10 was crystallized in the presence of 1 mM DAHP oxime; the inhibitor bound in subunits B and C with occupancies of 0.64 ± 0.04 and 0.78 ± 0.04 , respectively. In comparison, RS7_4_13 was crystallized in the presence of 5 mM DAHP oxime, and the inhibitor occupancy increased to 0.8 in both subunits B and C, which appears to be the maximum possible occupancy. Soaking 8 mM DAHP oxime into crystals that were previously co-crystallized with 1 mM DAHP oxime caused the crystals to shatter, most likely due to changes in ion strength in the crystal drops. One structure (MJ110_4_7), when soaked with 8 mM DAHP oxime did not shatter, however no evidence of bound DAHP oxime was observed.

3.3.2. *DAHP Oxime Binding*

DAHP oxime bound in the active site with the C1 carboxylate and the oxime moiety occupying the PEP binding site and the phosphate moiety bound in the presumed E4P phosphate binding site. The intervening carbohydrate chain of DAHP oxime was bound to the enzyme through a network of hydrogen bonds. It was anchored in position through hydrogen bonding to Lys97, Arg92 and Lys186. The oxime nitrogen atom made contact with Lys186, His268 and the water molecules Wat1 and Wat2. These two water molecules were present in all DAHP oxime-bound subunits. Wat1 and Wat2 were also in close contact with the oxime oxygen atom. The phosphate made contact with Arg99, and Thr100. The loop containing Arg99 and Thr100 closed around the phosphate group of DAHP oxime. The backbone carbonyl group of Pro98 was hydrogen bonded with the C5 hydroxyl of DAHP oxime. The C4 and C6 hydroxyl groups formed a bidentate hydrogen bonding interaction with the Asp326 O δ atoms, while the C4 hydroxyl made a further hydrogen bond to the Lys97 N ϵ atom (Figure 3.6). DAHP oxime binding was identical in both subunits.

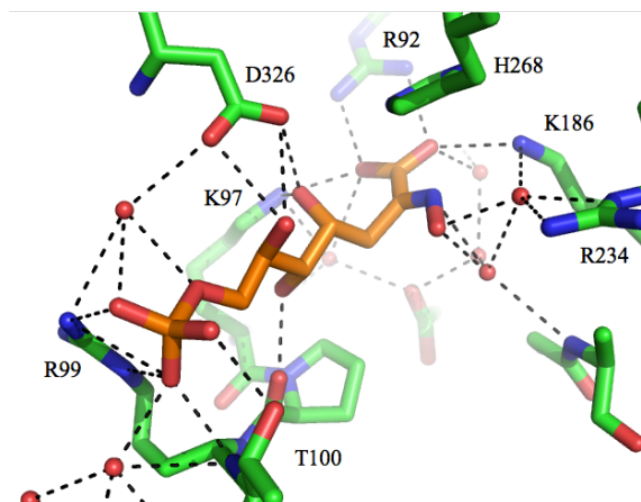


Figure 3.6: DAHPS_G binding site with DAHP oxime. Subunit C of Wai003_4_10 is shown.

One DAHP oxime-containing structure, RS7_1_5, had subunit D in a "hybrid" conformation. Subunit A had an open conformation and subunits B and C had closed conformations, as expected (Figure 3.8). The "hybrid" conformation had the K97 sidechain oriented similarly to chains B and C (i.e., not occluding the inhibitor/substrates binding site), and the loop in residues R99–V102 was similar to the subunit A. Thus, this structure was characterized as 1:2:1, or A(open):B/C(closed):D(hybrid).

3.3.3. Unbound Structures

Three ligand-free structures of DAHPS_G were solved, namely: MJ109_2_7, MJ110_4_7, and MJ109_1_11. All structures were crystallized in the presence of DAHP oxime; however, there was no evidence of DAHP oxime in the active sites. MJ109_2_7 crystallized with a dimer of tetramers in the asymmetric unit; all subunits were in identical, closed conformations essentially

identical to subunits B and C in the DAHP oxime-bound structures. In MJ110_4_7, all subunits were in the open conformations very similar to chains A and D in the inhibitor-bound structures. MJ109_1_11 crystallized as a tetramer of tetramers with metal ions in 14 of 16 active sites, though no metal was added to the crystallization buffer. Mn^{2+} was modeled into the structures as it fit into the electron density map, and in our assays DAHPS is most active with Mn^{2+} . Each tetramer had the same subunit conformations: A(open):B/C(closed):D(hybrid).

3.3.4. Cocrystallization of Inhibitor/Substrates/Phenylalanine.

Attempts to cocrystallize DAHPS_G with mixtures of substrates and DAHP oxime, or DAHP oxime and phenylalanine resulted in structures that were duplicates of those already solved, with one exception.

Structure MJ108_1_7 was solved as a DAHPS_G• Mn^{2+} ₂•PEP₂•Pi₂ structure. PEP molecules were bound to subunits B and C in the previously observed PEP binding site.⁵⁴ Electron density for inorganic phosphate (Pi) was observed in the same position as the terminal phosphate as DAHP oxime, which is presumably also the phosphate binding site for E4P. There was electron density in the metal binding site in subunits B and C, which was modelled as Mn^{2+} . The overall structures of subunits B and C were nearly identical, except that the temperature factors were lower for subunit B than C, similar to the temperature factor distribution of the DAHP oxime-bound structures. The L312-L318 loop was

disordered in both subunits. The unbound subunits A assumed the closed conformation, while D was in the hybrid conformation.

Structure MJ110_2_5 was solved as DAHPS_G•PEP₄•Lig₂, where Lig is an unknown phosphate-containing ligand. Subunits B and C were in the closed conformation, as expected for ligand-bound DAHPS_G, but subunits A and D were in the hybrid conformation, the only structure were subunit A was observed in the hybrid conformation. One PEP molecule was bound in each monomer in its usual position. There was an unknown phosphate-containing ligand with the phosphate group located in the DAHP oxime/E4P binding site in subunits B and C (Figure 3.7).

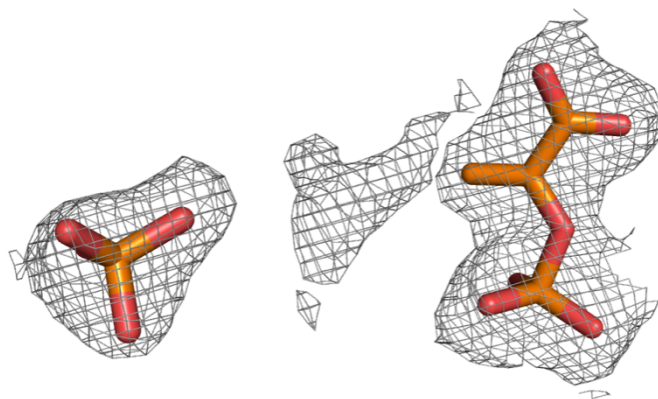


Figure 3.7: Electron density map showing unidentified electron density.

Electron density map showing bound PEP (right) and P_i (left), and unidentified electron density in subunit C of MJ110_2_5 structure. Density map was scaled to 1 σ .

The crystal was grown in the presence of PEP, E4P and DAHP oxime.

The electron density was not continuous from the phosphate to the PEP binding site, making the ligand unlikely to be DAHP oxime. Also, the electron density did not overlap well with DAHP oxime in other structures. The electron density

of the phosphate group was unambiguous, but if E4P was modelled into the structure, the electron density around the hydroxyl oxygen atoms was not convincing. It was discontinuous around the C4 carbon atom of E4P and only observable if the density map was scaled below 1σ . Refining occupancy of the site did not improve fitting. The structures of the individual subunits remained similar to each. Subunits B and C were in the closed conformation, while A and D were in the hybrid conformation. There was more disorder in the loop defined by residues 98-103 in subunits A and D.

3.4. Discussion

Seven unique DAHPS_G crystal structures were solved in this study, plus several duplicates that were solved enough to observe that they duplicated existing structures, and then were not fully refined (Table 3.1, Figure 3.8). All but one previously reported structures of the phenylalanine-regulated *E. coli* DAHPS were symmetrical, with all subunits adopting the closed conformation.^{54,136} The exception is DAHPS•Mn²⁺₄•PEP₄•Phe₄ (PDB: 1KFL⁵⁵) which had essentially identical open-like conformations in all four active sites, though the symmetry was broken by the W215 and H217 side chain conformations. These residues, which are located near the Phe binding site at the weak dimer interface, gave the tetramer two-fold symmetry, with subunits A and D having the same W215 and H217 side chain conformations as each other, as did subunits B and C.⁵⁵

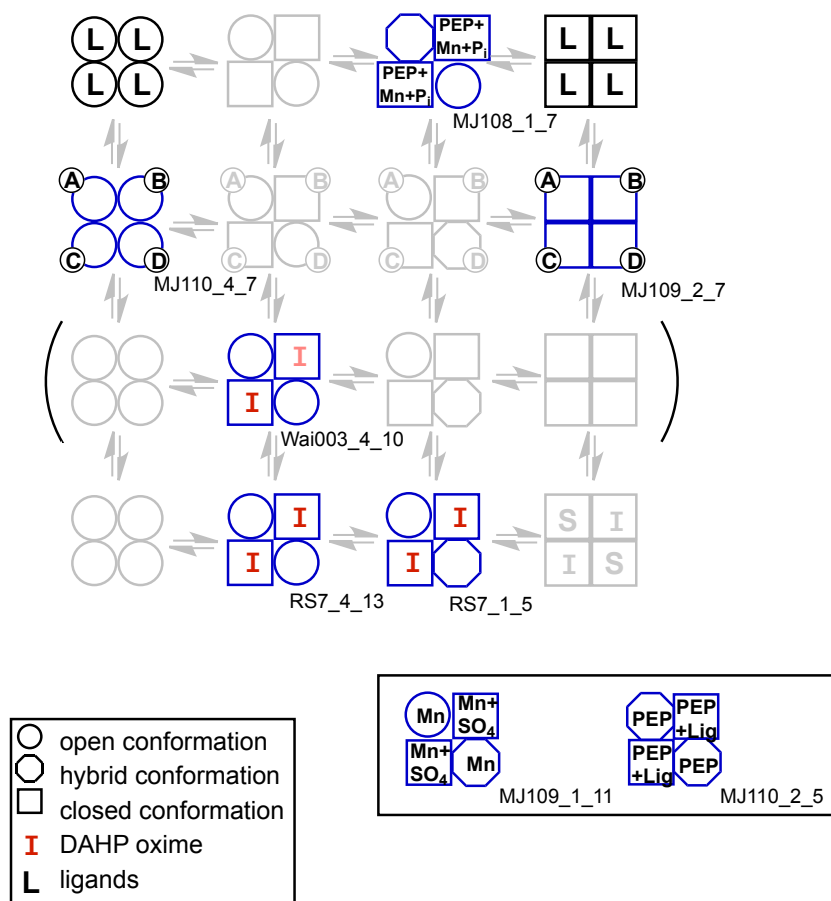


Figure 3.8: Observed conformations in DAHPS_G and DAHPS_G•ligand crystal structures.

Schematic representation of DAHPS_G conformations observed in this study (blue). Circles represent "open" (unbound) conformations, squares indicate "closed" (bound) conformations, and octagons represent "hybrid" structures, which are unbound, but contain features of both bound and unbound conformations. All previously solved *E. coli* DAHPS(Phe) structures (black) were fully symmetrical around the active site,^{54,136} though structure 1KFL⁵⁵ had two-fold symmetry in the dimer-dimer interface (see text). 1KFL contained Mn²⁺, PEP, and Phe, but PEP was misoriented in the active site. "L" (for ligand) in the figure indicates some combination of bound divalent metal ion, PEP, Phe, 2-phosphoglycolate, and/or sulfate.

The ligand-free structures of DAHPS (namely MJ110_4_7 and MJ109_2_7) adopted all-open and all-closed conformations, respectively. Three ligand-bound structures (Wai004_4_10, RS7_4_13 and MJ110_2_5) displayed two-fold symmetries. All three conformations, open, closed, and hybrid, were observed in MJ108_1_7, MJ109_1_11, and oxime bound RS7_1_5. Although

solid state structures do not always reflect the reality of solution phase structures, the fact that so many different conformations were observed in crystal structures that were crystallized under similar conditions implies that all conformations are relatively accessible in the solution phase in both the ligand-free and ligand-bound states.

The DAHP oxime-bound DAHPS_G structures revealed a two-fold symmetry in which DAHP oxime bound to two of the four active sites in each tetramer. The structures reported here are the first examples of asymmetric DAHPS active sites. The incomplete binding of DAHP oxime explains the residual rate observed at high inhibitor concentrations; however, why only 50% of the binding sites were bound is not understood. Structures of *M. tuberculosis* DAHPS, a homotetramer in solution showed two-fold symmetry in crystals structures where the asymmetric unit contained two monomers (PDB:3NV8).³⁹ Symmetry pairs had to be generated to get the full tetramer. Furthermore, one structure was solved with incomplete binding, as PEP was bound to only one of the subunits, with P_i bound in the other.

Structurally, both the bound and unbound sites were similar to each other. The unbound subunits had the K97 sidechain rotated such that it occupied the E4P binding site, thus excluding DAHP oxime binding. Nonetheless, the enzyme was still active at high inhibitor concentrations, meaning that the K97 sidechain was moveable. This strongly suggests that it was changes in enzyme dynamics, rather than discrete structural changes, that gave rise to the strong negative cooperativity

of DAHP oxime binding observed between subunits A and B, and between C and D.

In *M. tuberculosis* DAHPS, which contains binding sites for both tryptophan and phenylalanine as allosteric inhibitors, the presence of either molecule enhances the binding affinity for the other.¹⁵⁹ Both crystal structure and small angle x-ray scattering (SAXS) showed virtually no change when comparing the structures of free enzyme and allosteric inhibitor-bound enzyme. However, molecular dynamic simulations suggested that the signal is transmitted through changes in dynamics of the distal binding site upon binding of one of the inhibitors. Similarly, changes in protein motion were found to be responsible for negative cooperativity of cAMP binding to catabolite activator protein (CAP), a transcriptional activator which binds two cAMP molecules; that is, the increase in K_M for binding the second cAMP molecule was due to changes in protein motion.¹⁶⁰

The strong negative cooperativity of DAHP oxime binding between the subunits of the tight dimer, as observed in both the crystal structures and in the residual rate in inhibition assays suggest a half-of-sites reactivity mechanism in DAHPS catalysis. There are two manifestation of half site reactivity; sequential catalysis^{115,161} and alternating catalysis.¹¹¹⁻¹¹³ Catalysis in purine nucleoside phosphorylase is an example of sequential catalysis. Purine nucleoside phosphorylase is a homotrimeric enzyme that catalyzes the phosphorolysis of purine nucleosides to the purine base and ribose 1-phosphate. When the purine

product is formed, it forms a tightly bound enzyme•purine complex.¹⁶² It has been proposed that the enzyme uses the energy of formation and release of ribose 1-phosphate in one site to aid dissociation of the purine product from the neighbouring site.¹¹⁵ Inhibitor binding at one site completely inactivates the homotrimeric enzyme. In contrast, alternating catalysis involves a single subunit carrying out one full catalytic cycle before catalysis can occur in an adjacent subunit. An example of alternating catalysis is cytochrome bc_1 complex.¹¹¹ The complex, which is composed of multiple subunits, transfers electrons from ubiquinol to cytochrome *c*. The wild-type complex is a dimer; however, it was found that hybrid dimers where one complex is inactivated by mutation retained wild-type activity.

Our observations are in line with an alternating catalysis mechanism. In this mechanism inhibitor binding in one active site reduces, but does not abolish, activity at neighbouring sites.¹¹¹ There is also an indication of subunit communication in DAHP oxime inhibition of DAHP(Phe), as inhibitor binding leads to a 70% reduction in apparent k_{cat} , rather than the 50% expected if two subunits were inhibited and two were unaffected. The nature of this inter-subunit communication is not clear.

Aside from the two-fold symmetry around the W215/H217 site in one DAHPS crystal structure (1KFL),⁵⁵ there is no evidence in the literature to suggest half-of-sites reactivity for DAHPS. However, as noted in a review by Seydoux et

al.,¹⁶³ half-of-sites reactivity in a number of enzymes was discovered only through pseudo-substrates or inhibitors, and was not visible with the normal substrates.

For *E. coli* KDO8PS, an alternating catalytic cycles mechanism has been proposed.⁷⁶ In that study, KDOPS catalysis was observed in the presence of PEP and E4P or R5P. As E4P is one carbon smaller than the natural substrate and R5P has incorrect stereochemistry, KDO8P was not formed. Rather, it was observed that PEP was being consumed in two stages. First involved rapid conversion of PEP to pyruvate and P_i , then a slow conversion of PEP to 2-phosphoglyceric acid. It was found that the rapid conversion of PEP to pyruvate and P_i occurred in half of the active sites, inactivating the subunits, while in the remaining two subunits, the aborted reaction product, 2-phosphoglyceric acid was being formed at a slow rate. From this observation the authors proposed a half site reactivity mechanism. PEP was proposed to be bound to all subunits, while A5P binding alternates between subunits. Upon catalysis in these sites, the products KDO8P and inorganic phosphate are displaced by PEP and A5P binding in the remaining sites (Figure 3.9).

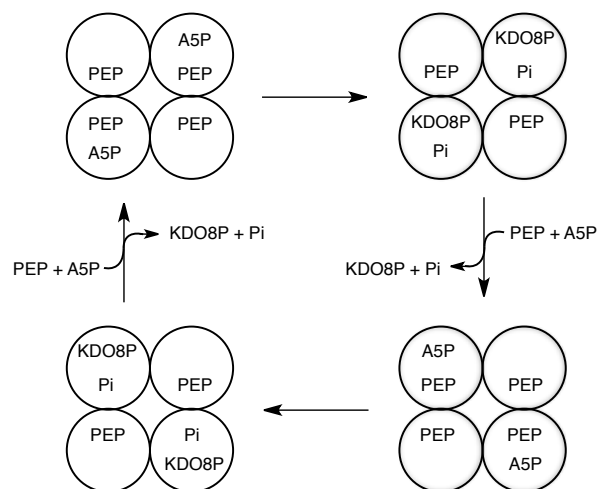


Figure 3.9: Proposed catalytic cycle for *E. coli* KDO8PS.

In the proposed kinetic mechanism, all subunits may bind PEP, while A5P binds to alternating sites, where catalysis occurs, followed by product dissociation and A5P binding in the remaining sites. Figure was recreated from Howe et al.⁷⁶

This mechanism closely relates to our observations in that binding of DAHP oxime does not affect binding of substrates to the remaining sites. The remaining sites are able to undergo catalysis, albeit at with a lower k_{cat} .

As part of this study, seven unique crystal structures were solved. The unbound structures suggest a dynamic enzyme able to adopt multiple conformations. Upon inhibitor binding, two-fold symmetry is created with strong negative cooperativity for complete inhibitor binding. Structurally, there is no obvious cause of the observed negative cooperativity, as both the inhibitor bound and unbound subunits are similar in structure. Only two of the four available subunits are DAHP oxime-bound in the crystal structures, with the unbound sites remaining active with a reduced apparent k_{cat} value. These observations suggest that a) DAHPS utilizes an alternating subunit catalytic mechanism, and b)

changes in enzyme dynamics rather than discrete structural changes may be responsible for the observed negative cooperativity.

Chapter 4 - DAHP Synthase Dynamics

4.1. Introduction

Enzymes' motions and those motions' relation to function have become an expanding area of research in recent years.¹⁶⁴⁻¹⁶⁸ Two techniques that are widely utilized include NMR¹⁶⁸⁻¹⁷² and hydrogen/deuterium (H/D) exchange.^{167,173,174}

4.1.1. NMR

Historically, the study of large macromolecules by NMR has been limited due to signal overlap and signal loss with increasing size. Advances in protein NMR have lead to new methodologies that can be applied to large macromolecules, namely transverse relaxation optimized spectroscopy (TROSY) NMR¹⁷⁵ and ¹⁹F NMR.¹⁷⁶

4.1.2. TROSY NMR

The application of NMR to large macromolecules is limited by loss of magnetization due to transverse relaxation (T_2).¹⁷⁷ The predominant mechanisms that lead to rapid T_2 relaxation include dipole-dipole coupling and chemical shift anisotropy. Individual multiplets in a two spin system (e.g., ¹⁵N-¹H) undergo different rates of relaxation due to cross coupling of the different relaxation mechanisms.^{178,179} TROSY NMR focuses on the single multiplet that has the longest T_2 relaxation time,^{175,177} with application towards proteins of higher molecular mass.

4.1.3. ^{19}F NMR

Fluorine has a natural abundance of 100% ^{19}F , and, as there are no other fluorine atoms in proteins, no background signal.¹⁷⁶ The high sensitivity of the fluorine nuclei allows for high sensitivity in 1D NMR spectra as well as in studying tertiary structure through ^{19}F - ^{19}F or ^{19}F - ^1H NOEs experiments.¹⁸⁰ As an NMR probe, ^{19}F chemical shifts are highly sensitive to van der Waals forces and electrostatic fields.¹⁷⁶ Changes in the chemical shift can then be used to study ligand binding and conformational change within larger proteins than is traditionally possible by protein NMR.¹⁷⁶

4.1.4. *H/D Exchange by Mass Spectrometry*

An alternative methodology to study protein dynamics is through hydrogen/deuterium (H/D) exchange by mass spectrometry. In H/D exchange experiments, the rates and extent of exchange of solvent D atoms with exchangeable H atoms in a protein provide information on protein structure and dynamics. The exchange rate of exchangeable protons in the protein will depend on solvent accessibility and the extent of hydrogen bonding (i.e., structure) of each proton. Protons in structured regions will have more hydrogen bonding and will undergo slower exchange with solvent compared to less hydrogen bonded protons in unstructured or less structured regions.^{181,182}

Historically, H/D exchange by mass spectrometry was a laborious process involving H/D exchange, proteolytic digestion of sample, separation of the

resulting peptides by liquid chromatography, followed by offline mass spectrometry to detect deuterium incorporation.¹⁸² This procedure is long and allows for extensive back exchange of D atoms with H atoms, which results in the loss of important kinetic data. Recently, Rob et. al.¹⁸¹ developed a microfluidics-based system with online mass spectrometer to study H/D exchange, and used DAHPS_G, cytochrome c and ubiquitin to demonstrate the method's utility. Using their microfluidics device, they investigated the H/D exchange rates of weakly structured loop regions and compared their results with published crystallographic data. The H/D exchange data for cytochrome c and ubiquitin were generally consistent with the X-ray crystal structures, which helped to demonstrate that when the solution and crystal structures are the same, the method will demonstrate that fact. This method has the potential for rapid measurement of H/D exchange rates on the time scale of seconds to minutes, with low H/D back exchange rates, making it useful in studying protein dynamics. Protein size is largely irrelevant in H/D exchange studies by mass spectrometry.

In this chapter we outline our study of DAHPS dynamics by NMR and H/D exchange. Due to the size of the DAHPS tetramer, both ¹⁹F NMR and TROSY NMR proved to be unsuitable for study. Global H/D exchange experiments with free, PEP-bound and DAHP oxime-bound DAHPS_G showed DAHPS_G to be highly dynamic, with weak secondary structure in the free form. PEP binding imposed structural rigidity in line with the observed crystal

structures. DAHP oxime binding shifted the enzyme into a different dynamic state that was distinct from both the free and PEP-bound enzyme.

4.2. Materials and Methods

4.2.1. Purification of DAHPS_G for H/D exchange experiments

Expression and purification of DAHPS_G (*E. coli* DAHP synthase (*aroG*) with an *N*-terminal TEV protease cleavable His₆-tag in a pET300/NT-DEST plasmid) was carried out as described in Chapter 3. After removal of the *N*-terminal His₆ tag, DAHPS_G was then buffer exchanged into 20 mM ammonium acetate, pH 7.5, and run through a 1 mL nickel-charged metal affinity column to remove uncleaved DAHPS_{H6-TEV}. The protein was concentrated, and its concentration was determined from the A₂₈₀.^{126,127}

4.2.2. H/D Exchange Experiments

H/D exchange rates for the burst phase were obtained by rapidly mixing 50 μM DAHPS_G in 10 mM ammonium acetate, pH 7 with the same buffer in D₂O in a capillary tube mixer, then atomizing the mixture into a mass spectrometer. Mixing times was adjusted by adjusting the length of capillary tubing between initial mixing and injection into the mass spectrometer (Figure 4.1).

For extended preincubations, H/D exchange data was gathered by preincubating 50 μM DAHPS_G in 10 mM ammonium acetate, pH 7, made in D₂O, for the indicated time before injecting into the mass spectrometer.

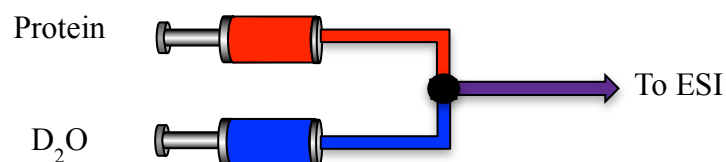
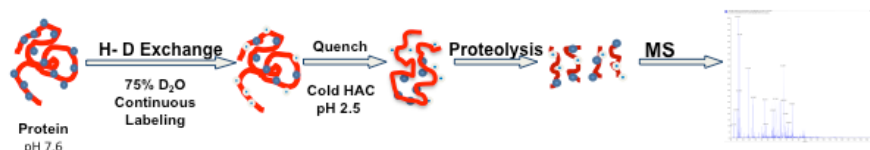


Figure 4.1: Schematic of the global H/D exchange experiment setup.

Protein in 20 mM ammonium acetate, pH 7.5, was mixed with the same buffer in D₂O in a mixing chamber, and then injected directly into the mass spectrometer. Mixing time was varied by varying the length of tubing leading to the mass spectrometer.

Spatially resolved H/D experiments were carried out on a microfluidics device made by Tamanna Rob from Dr. Derek Wilson's group (York University) (Figure 4.2). See Rob et. al.,¹⁸¹ for the protocol.

(a)



(b)

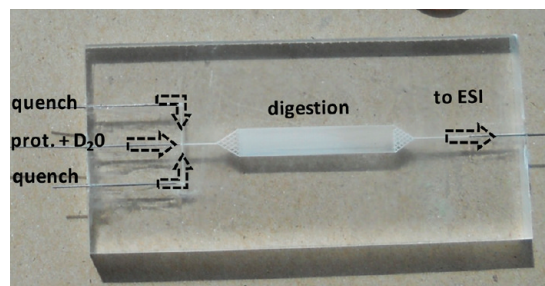


Figure 4.2: Diagram of the spatially resolved H/D exchange experiments.

a) Schematic representation of the steps involved in the spatially resolved H/D exchange experiment. The enzyme was allowed to exchange with D_2O from 42 ms to 10 s. The mixture was then quenched at pH 2.6 using 4% acetic acid. The mixture was then digested with pepsin and injected into the mass spectrometer. (Schematic was created by Tamanna Rob.) b) Picture of microfluidics device used in this experiment. (Figure is from reference ¹⁸¹, used with permission from the American Chemical Society, ©2012).

4.2.3. Labelling of DAHPS with 5-Fluorotryptophan or $^{15}N_2$ -Tryptophan

Seed cultures of *E. coli* BL21*(DE3) cells containing His₆-TEV tagged *aroG* in pET300 vector were grown in M9 medium (see Chapter 2 for preparation protocol) containing 100 µg/mL ampicillin for 8 h. The seed culture was then transferred to 25 mL M9 culture containing 100 µg/mL ampicillin for overnight growth. The overnight culture was used to inoculate 500 mL M9 containing 100 µg/mL ampicillin. Cells were grown at 37°C with shaking until OD₆₀₀ = 0.6. Glyphosate (1 g/L) was added to inhibit aromatic amino acid biosynthesis, and cells shaken for additional 30 min to consume all endogenous aromatic amino acids. L-tyrosine, L-phenylalanine and D/L-5-fluorotryptophan (FTrp) (50 mg/L

of each)¹⁸³ were added along with 1 mM IPTG to induce protein expression. Cells were harvested after 4 h by centrifugation at 8000 × g for 20 min. Cells were re-suspended in 5 mL of buffer A (50 mM Tris-Cl, pH 7.5, 150 mM NaCl, 50 mM imidazole)/g of cell pellet and purified using the same procedure outlined in chapter 3.

The *N*-terminal His₆ tag was removed by treating DAHPS_{H6-TEV} with TEV protease as described in Chapter 3 to yield DAHPS_G. The cleavage reaction was then buffer exchanged into 20 mM Tris-Cl, pH 7.5, and run through a 1 mL nickel-charged metal affinity column to remove uncleaved DAHPS_{H6-TEV}. The flowthrough was collected and concentrated using centrifugal ultrafiltration. D₂O was added to a final concentration of 10% (v/v) before running on the 600 MHz NMR for to obtain a 1-D ¹⁹F NMR spectrum. The final protein concentration was 200 μM.

Incorporation of ¹⁵N-tryptophan into DAHP synthase was carried out by supplementing the M9 medium with 50 mg of ¹⁵N₂-tryptophan in place of D/L-5-fluorotryptophan. TROSY experiments were run in 20 mM Tris-Cl, pH 7.5, with 50 mM KCl and 10% D₂O on a 700 MHz NMR.

4.2.4. ¹⁹F NMR

¹⁹F NMR spectra of FTrp-labelled DAHPS_G (200 μM in 90% H₂O/ 10% D₂O 20 mM Tris-Cl, pH 7.5, 0.1 mM TCEP) was obtained on Bruker 600 MHz

NMR with the help of Dan Sorenson and Bob Berno from the McMaster University NMR facility. The 1-D spectrum was obtained at 10 °C with 2048 scans.

¹⁵N-Tryptophan NMR

¹⁵N-¹H TROSY spectra of [¹⁵N₂-Trp]DAHPS_G (330 μM in 90% H₂O/10% D₂O 25 mM Tris-Cl, pH 7.5, 50 mM KCl, 0.1 mM TCEP) were obtained on a Bruker 700 MHz NMR spectrometer. The 2-D spectra was obtained at 33°C with 212 (t1) and 1024 (t2) complex points and spectral widths of 31.82 ppm and 15.94 ppm for the ¹⁵N and ¹H dimensions, respectively, were recorded with 32 scans and a recycle delay of 1.70 s⁻¹. Spectrum was obtained by Dr. Rajeevan Selvaratnam.

4.3. Results

4.3.1. ¹⁹F NMR

We attempted to employ fluorine NMR as a means of studying the dynamics or changes in dynamics upon inhibitor binding in DAHPS_G by following changes in fluorine chemical shifts and peak widths. We chose to label DAHPS with 5-fluorotryptophan (FTrp) because there are four Trp residues/monomer. Each Trp residue is located in a different region within the monomer: Trp104 is located near the opening of the active site; Trp159 is buried

in hydrophobic core near the active site; Trp215 is at the tight dimer-dimer interface, and Trp331 is solvent exposed.

In order to label the protein with 5-fluorotryptophan (FTrp) residues, the protein was expressed in M9 minimal medium, with glyphosate added to prevent endogenous aromatic amino acids synthesis. Seed cultures that were grown in LB and used to inoculate 1L M9 medium were able to grow in the presence of glyphosate, suggesting residual aromatic amino acids from the LB were present. Therefore, a glycerol stock of aroG:pET300 vector in BL21(DE3) cells that were acclimatized to M9 medium were used for expression. Mass spectrometry confirmed FTrp incorporation in DAHPS_G.

In principle, four unique peaks would be expected in the DAHPS_G ¹⁹F NMR spectrum, one for each tryptophan. The spectrum of 5-fluorotryptophan showed a multiply split signal at -124 ppm (Figure 4.3a). The multiplet was due to ¹H coupling, as the NMR probe was not designed to decouple ¹⁹F and ¹H nuclei. The ¹⁹F NMR spectrum of FTrp-DAHPS_G showed a multiply split peak at -119 ppm (Figure 4.3b). It is not clear whether this one peak represents numerous FTrp residues, or a single residue with the others not visible due to local dynamics of the individual FTrp residues. Addition of 2 mM PEP led to the collapse of the splitting resulting in a single peak (Figure 4.3c). The loss of splitting with the addition of PEP cannot be explained. No visible precipitation was observed. It is unlikely to be a contaminant, as a contaminating compound with a peak exactly overlapping the signal from DAHPS_G is unlikely. Also, any contaminating

product would likely be removed during protein purification and buffer exchange steps. We do not know why splitting was lost or why only one signal was observed.

We did not observe any protein signal from the TROSY experiments.

Since this work was performed, an undergraduate student, Elizabeth Curiel-Tejeda expressed and characterized the Tyr-sensitive isoform of *E. coli* DAHPS. Scott Prosser's lab at University of Toronto at Mississauga has obtained good quality ^{19}F and ^{15}N spectra with this labelled protein.

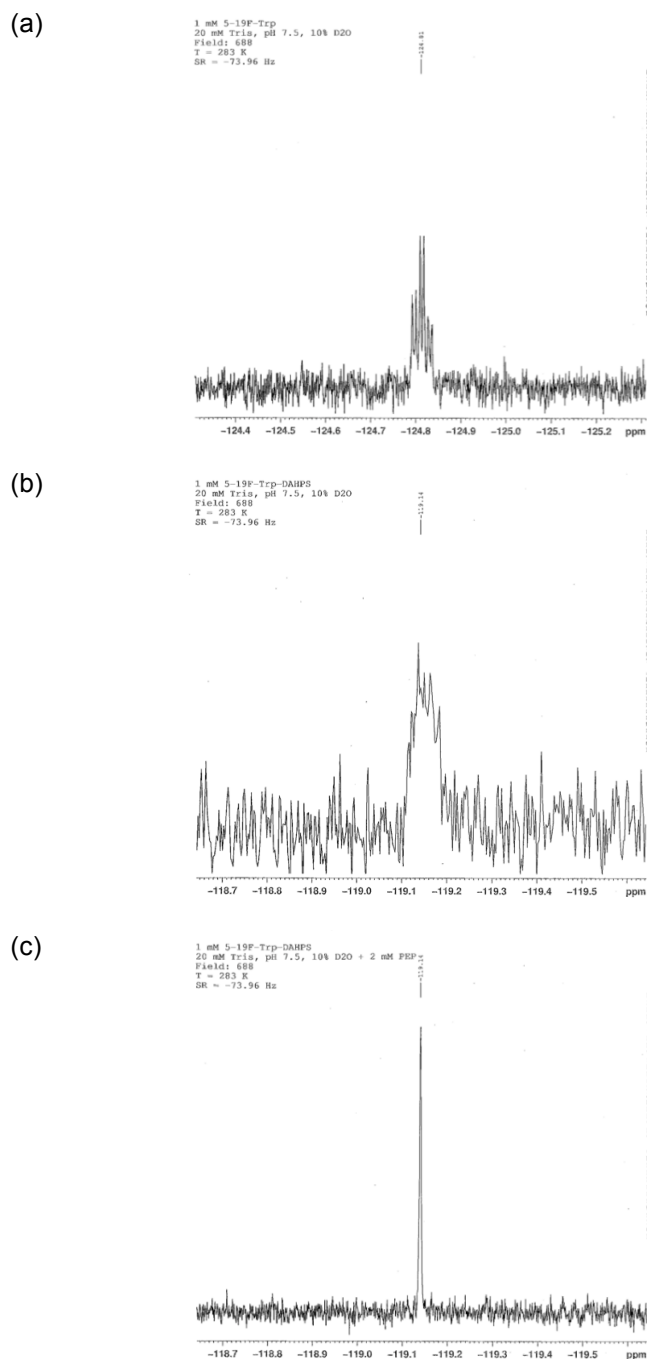


Figure 4.3: ^{19}F NMR spectra of 5-fluorotryptophan labelled DAHPS_G.

(a) ^{19}F NMR spectrum of 1 mM 5-fluorotryptophan in 20 mM Tris-Cl, pH 7.5, with 10% D₂O. The spectrum was obtained at 10°C with 16 scans. (b) ^{19}F NMR spectrum of 200 μM DAHPS_G in 20 mM Tris-Cl, pH 7.5, with 10% D₂O. The spectrum was obtained at 10°C with 2048 scans. (c) ^{19}F NMR spectrum of 200 μM DAHPS with 2 mM PEP in 20 mM Tris-Cl, pH 7.5, with 10% D₂O. The spectrum was obtained at 10°C with 2048 scans.

4.3.2. *Global H/D Exchange*

To study the effect of inhibitor binding on the global DAHPS_G structure and dynamics, we investigated H/D exchange rates on the bound and unbound enzyme. H/D exchange was monitored by following the increase in apparent molecular weight (ΔMass) as a function of time (Figure 4.4). Under the extremely mild ionization conditions used for this experiment, some solvating waters remained associated with the protein molecules in the mass spectrometer. As such, the absolute values of ΔMass were not informative on their own, as they included solvating waters; however, the relative values in the presence of different ligands, and changes as a function of time, were informative. There are two stages of global H/D exchange; a burst phase where surface exposed and unstructured protons are exchanged within 1 s of mixing, followed by slow exchange of structured protons (Figure 4.4).

Free DAHPS_G had a burst phase in which $\Delta\text{Mass} \approx 900$ within 2 s, after which an additional ~ 300 exchanges were observed over 60 min. DAHPS_G•PEP had a burst phase in which $\Delta\text{Mass} \approx 400$, followed by ~ 220 exchanges over 60 min. Thus, H/D exchange indicated that PEP-bound DAHPS_G was significantly more structured. DAHPS_G•DAHP oxime had a burst phase with $\Delta\text{Mass} \approx 600$, followed by a slow exchange of ~ 525 over 60 min. DAHPS oxime-bound DAHPS_G had an initial burst lying between that of the free and PEP-bound DAHPS_G, suggesting that rigidity is introduced with DAHP oxime binding, but

that it remains more dynamic than PEP-bound DAHPS_G, and approaches the total exchanges observed with free DAHPS.

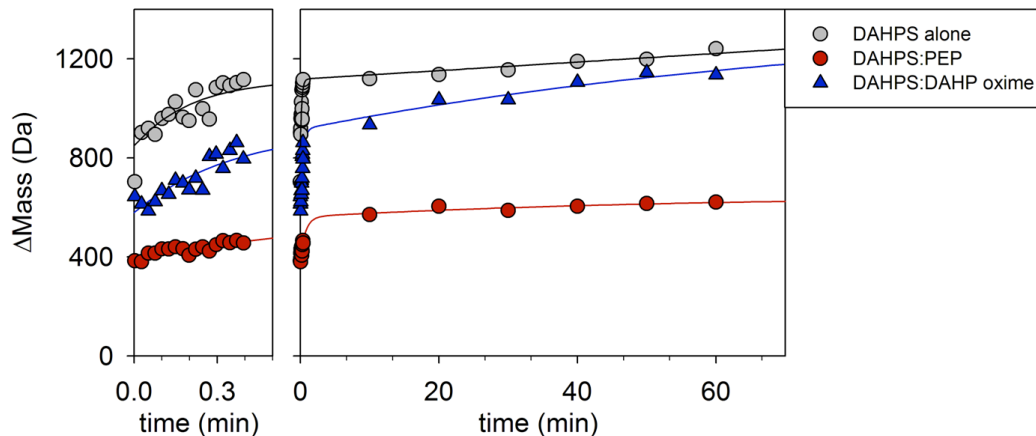


Figure 4.4: Global H/D exchange data for free DAHPS_G, DAHPS_G•DAHHP oxime and DAHPS_G•PEP.

Data is plotted as the change in mass (ΔMass) vs. mixing time with D₂O-containing buffer. Figure courtesy of Dr. Paul Berti. Data collected by Peter Liuni and Dr. Derek Wilson of York University.

4.3.3. Spatially Resolved H/D Exchange

In collaboration with Tamanna Rob and Dr. Derek Wilson (York University) we recently published spatially resolved H/D exchange experiments on DAHPS_G.¹⁸¹ Spatially resolved H/D exchange measures the number of protons undergoing exchange in a given peptide, as well as the average rate of exchange of a given peptide. The relationship between the rate of exchange in an unstructured peptide with the experimentally measured rate of exchange is illustrated in eq. 4.1.¹⁸¹

$$k_{ex} = \frac{k_{op}}{k_{cl}} k_{int} = K_{op} k_{int} \quad (4.1),$$

where k_{ex} is the measured rate of exchange, k_{cl} and k_{op} are the rates of forming and breaking a hydrogen bond respectively, and k_{int} is the intrinsic rate of exchange of an amide proton in an unstructured peptide. The intrinsic rate is dependent on the local amino acid sequence.^{184,185} The opening/closing equilibrium, K_{op} , a measure of local stability, can be determined from $k_{\text{ex}}/k_{\text{int}}$. More commonly, the local stability of a peptide is expressed as a Protection Factor (PF) which is the inverse of K_{op} , i.e., $\text{PF} = 1/K_{\text{op}}$.¹⁸⁶

On the time scale of the experiments carried out here, exchange of backbone amides from secondary structures should be negligible, and most of the exchangeable protons should be from loop regions.¹⁸¹ In this context, N_{fast} is the number of amide protons in a given peptide that undergo exchange on the time scale of the experiment, and N_{loop} is the number of expected loop amides in that peptide, based on the crystal structure.

Sequence coverage from spatially resolved H/D exchange of free DAHPS_G, DAHPS_G•PEP and DAHPS_G•DAHP oxime was 60%, 58% and 59% with an average peptide length of 6, 6 and 12 amino acids, respectively.

H/D exchange data for free DAHPS_G showed little correlation between N_{loop} and N_{fast} ,¹⁸¹ suggesting a dynamic enzyme with less defined secondary structure around the solvent exposed regions than expected from the crystal structures, and less than that of DAHPS_G•PEP⁵⁵ (Table 4.1, Figure 4.5).

Table 4.1: Time resolved H/D exchange statistics for free and PEP-bound DAHPS_G peptides.

Segment	% N _{loop} ^a	%N _{fast} , ^b DAHPS _G	PF, ^c DAHP _G	%N _{fast} , ^b DAHPS _G *PEP
3-9	100	57 ± 10	16 ± 6	41
18-23	33	59 ± 12	5 ± 4	45
24-36	17	110 ± 5	27 ± 6	93
47-55	75	55 ± 10	6 ± 3	51
69-72	0	49 ± 11	5 ± 3	50
83-88	100	97 ± 9	2 ± 1	97
88-91	0	69 ± 12	2 ± 1	54
96-108	77	105 ± 11	11 ± 3	39
97-102	80	106 ± 17	10 ± 4	40
105-113	25	61 ± 8	6 ± 2	25
108-114	50	92 ± 10	5 ± 3	25
108-117	67	74 ± 12	15 ± 5	26
118-123	0	73 ± 10	9 ± 3	23
118-124	0	77 ± 15	8 ± 4	22
134-140	33	98 ± 19	23 ± 9	35
158-165	57	73 ± 11	15 ± 5	53
186-191	100	68 ± 14	24 ± 8	52
196-203	0	76 ± 16	11 ± 6	47
198-206	38	45 ± 9	12 ± 3	24
205-216	55	65 ± 10	14 ± 4	16
216-220	50	54 ± 7	24 ± 8	51
222-226	50	50 ± 6	32 ± 5	40
232-235	33	98 ± 16	4 ± 1	72
250-253	0	75 ± 18	7 ± 3	78
254-257	33	73 ± 16	9 ± 4	70
258-262	75	73 ± 12	5 ± 2	78
262-267	40	55 ± 10	3 ± 1	39
262-268	50	71 ± 10	5 ± 2	53
276-281	0	18 ± 5	25 ± 11	20
282-293	18	74 ± 13	20 ± 6	-
284-293	22	62 ± 9	12 ± 3	-
289-294	60	59 ± 8	12 ± 2	42
290-296	83	87 ± 17	16 ± 4	37
292-296	100	72 ± 15	11 ± 3	61
300-305	100	74 ± 11	8 ± 2	80
308-315	100	47 ± 18	23 ± 11	46

309-313	100	76 ± 15	32 ± 8	67
343-346	100	50 ± 12	19 ± 9	-

^a %N_{loop} refers to the percent of the observed sequence that is in a loop as determined from crystal structure.

^b %N_{fast} represents the percent of the observed sequence in a loop determined experimentally from exchange rates.

^c Protection factor = 1/K_{op} (eq. 4.1).

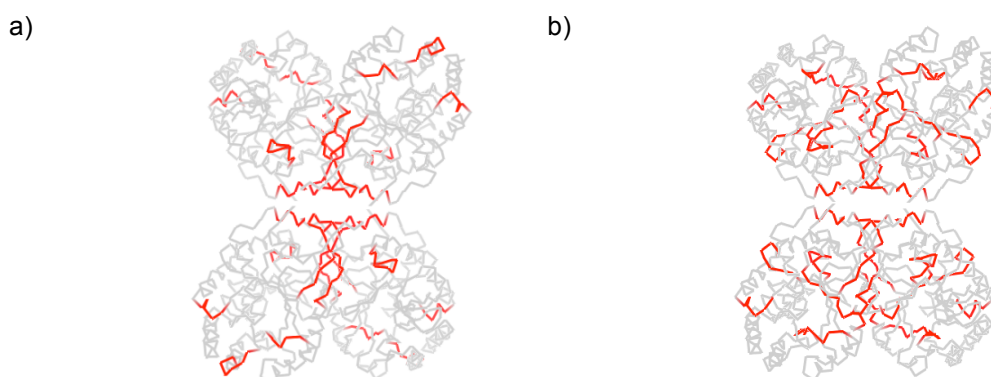


Figure 4.5: %N_{fast} vs. %N_{loop} of DAHPS_G.

E. coli DAHPS(Phe) structure (PDB:1KFL⁵⁵) is shown with loops in red where %N_{fast} was in agreement with %N_{loop}. **a)** Unbound DAHPS_G **b)** DAHPS_G•PEP. Only loops where difference between %N_{fast} and %N_{loop} was ≤10% are highlighted.

Addition of PEP caused stabilization of the enzyme's surface-exposed loops such that the H/D exchange data were in better agreement with crystallographic structures (Table 4.1, Figure 4.5b). The decreased %N_{fast} amplitudes upon PEP addition to DAHPS_G demonstrated a broad structural stabilization. The greatest change in amplitude was observed in the sequences 96-140, 206-216 and 282-294. The sequence 96-140 makes up part of the active site and makes contact along the tight dimer interface as well as the dimer-dimer interface. Sequence 205-216 is found along the tight dimer interface and sequence 282-294 is located on the periphery of the enzyme, and is solvent exposed.

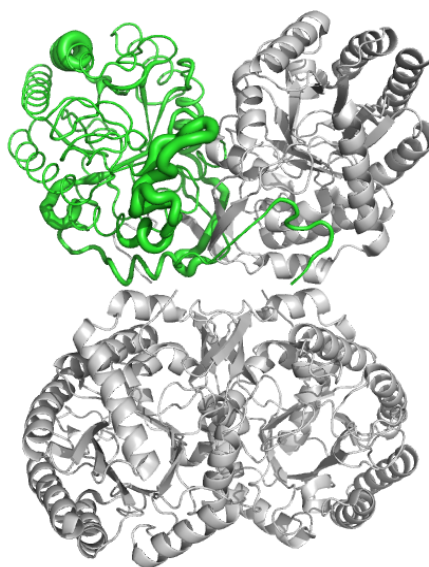


Figure 4.6: Differences in %N_{fast} amplitude between free DAHPS_G and DAHPS_G•PEP. Structure 1KFL⁵⁵ is displayed as a cartoon (gray) except for subunit A (green). The line width in subunit A is thicker for peptides showing greater stabilization upon addition of PEP; i.e., $\Delta\%N_{fast} = \%N_{fast}(DAHPS_G) - \%N_{fast}(DAHPS_G \cdot PEP)$.

Like free DAHPS_G, deuterium uptake in DAHPS_G•DAHP oxime indicated little correlation between %N_{fast} and %N_{loop} amplitudes (Table 4.2, Figure 4.7). In this sense, DAHPS_G•DAHP oxime was more similar to free DAHPS_G than DAHPS_G•PEP. The sequence coverage was somewhat different between free and DAHP oxime-bound DAHPS_G, making a comprehensive comparison between %N_{fast} amplitudes impractical. In general, PF increased with addition of DAHP oxime (Figure 4.8). In particular, the regions surrounding the active site showed increases in PF, which was in line with the global H/D exchange results, where addition of DAHP oxime reduced deuterium uptake relative to DAHPS_G (Figure 4.4).

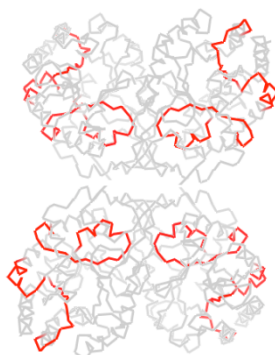
Table 4.2: Time-resolved H/D exchange statistics from DAHP oxime bound DAHPS_G peptides.

Segment (amino acid number)	%N _{loop} ^a	%N _{fast} ^b	PF ^c
5-8	100	55	18
10-23	23	100	10
30-43	0	86	68
37-53	25	52	36
44-48	0	100	24
56-72	38	100	44
57-69	42	100	21
78-88	50	46	13
80-87	57	51	6
124-132	0	86	30
133-145	33	39	18
145-155	40	33	10
146-157	27	31	11
161-171	80	100	41
285-294	33	58	62
290-303	100	100	45
340-351	9	80	35

^a %N_{loop} refers to the percent of the peptide that is in a loop based on the crystal structure.

^b %N_{fast} is the percent of the peptide that is in a loop, as determined experimentally from H/D exchange rates.

^c Protection factor = $1/K_{op}$ (eq. 4.1).

**Figure 4.7: %N_{fast} vs. %N_{loop} of DAHPS_G-DAHP oxime.**

Loops where %N_{fast} is in agreement with %N_{loop} are shown in red. Only loops where difference between %N_{fast} and %N_{loop} are $\leq 10\%$ are highlighted. The structure is 1KFL.⁵⁵

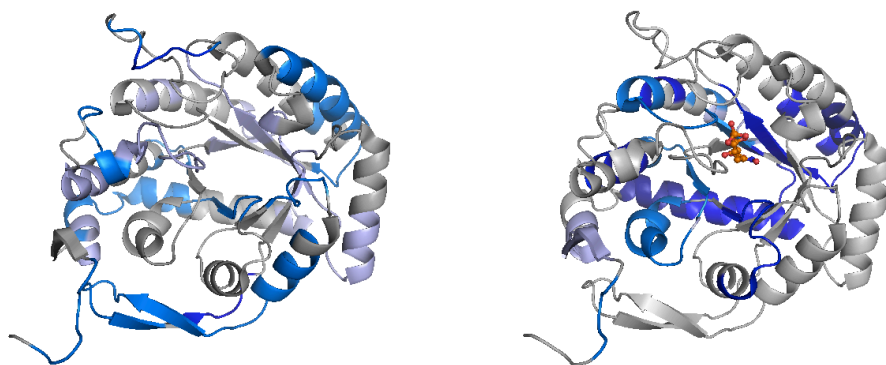


Figure 4.8: Comparison of PF between free DAHPS_G and DAHPS_G•DAHP oxime.

The protein backbone is coloured according to PF values of (left) free DAHPS_G and (right) DAHPS_G•DAHP oxime. Light blue, PF = 1-10, medium blue; PF = 11-29; blue, PF = 30-50, and dark blue, PF > 50. The structure is 1KFL subunit A, with DAHP oxime superimposed on the right structure.⁵⁵

4.4. Discussion

Attempts to probe DAHPS_G dynamics by NMR were unsuccessful.

Presumably, the DAHPS tetramer was too large to be studied by NMR. To improve signal, longer acquisition times, higher enzyme concentration and expression of protein in deuterated medium could have been attempted; however, we believe the size of DAHPS_G(Phe) will still be a limiting factor. Instead, ¹⁹F NMR studies on the dimeric tyrosine-sensitive *E. coli* DAHPS_G are currently underway.

H/D exchange by mass spectrometry demonstrated DAHPS_G to be a dynamic structure with significant stretches of intrinsically disordered peptides in the free enzyme. Of the total number of protons that exchanged within 60 min, 75% exchanged within 1 s of deuterium exposure (Figure 4.4). This implied very little correlation between the surface-exposed secondary structures in solution and those observed in crystal structures of free DAHPS in this study (Chapter 3), and

in the literature.^{53,54,136,158} Adding PEP decreased by > 50% the size of the initial burst of exchange, and the total amount of exchange over 60 min (Figure 4.4). Spatially resolved H/D data reaffirmed the induction of more a structured protein surface upon PEP binding, as revealed by the reduction of %N_{fast} amplitude (Table 4.1).

The region 96-140 underwent the greatest changes in %N_{fast} amplitudes upon PEP binding (Figure 4.6). This is consistent with the crystal structures, where loop 95-105 underwent the largest observed conformational changes between the free and DAHP oxime-bound DAHPS_G structures (Chapter 3). Region 96-140 forms part of the active site and lies between the tight dimer and dimer-dimer interfaces. This region could be significant in the observed cooperative behaviour in DAHP oxime binding.

The second largest change in H/D exchange was peptide 282-293, which is distant from the active site and solvent exposed, with no contact with neighbouring subunits. Upon PEP binding it also showed a significant reduction of %N_{fast} amplitude. The significance of this stabilization is not clear.

DAHP oxime binding did not stabilize DAHPS_G dynamics to the same extent as PEP (Figure 4.7). DAHP oxime binding reduced global H/D exchange and stabilized peptides around the active site, namely residues 56-69 , 161-171 and 290-303. One complication in interpreting the H/D exchange results is the half-of-sites binding by DAHP oxime. The crystal structures and the kinetic data both show that the inhibitor bound to only two subunits of the DAHPS_G tetramer.

However, mass spectrometric data is unable to distinguish peptides originating in the bound subunits from those originating in the unbound subunits.

The H/D exchange data provide evidence that a number of surface-exposed regions that are structured in the X-ray crystal structures (including some regular secondary structures like α -helices) are disordered in the unbound protein in solution. PEP induces a global stabilization of conformers, presumably selecting conformations that are required for catalysis. DAHP oxime introduces dynamic stability to DAHPS_G but not to the extent observed with PEP. Spatially resolved H/D exchange data revealed little similarity in terms of the dynamic changes elicited by PEP binding versus DAHP oxime binding. DAHP oxime-bound DAHPS_G was dynamically distinct from both DAHPS_G•PEP and unbound DAHPS_G. Whether the different dynamic environment is responsible for the observed cooperativity (negative cooperativity, in the form of half-of-sites binding, and the positive cooperativity observed in slow-binding inhibition) is not yet clear, but it is a possibility.

Chapter 5 - Linear Free Energy Relationship Analysis of DAHP Oxime Binding

5.1. Introduction

Enzymes achieve tremendous rate enhancement over uncatalyzed reactions by stabilizing the transition state and thereby lowering the activation energy for the reaction.¹⁸⁷ As a consequence, enzymes bind the transition state more tightly than the reactant(s). In this context, inhibitors that mimic well the features of the transition state can be expected to bind the target enzyme much more tightly than substrate or product mimics; however, potent inhibition alone is not sufficient evidence of transition state mimicry, as opposed to fortuitously tight binding. Demonstration of a linear free energy relationships (LFER) of inhibitor binding, however, is an accepted method to determine if an inhibitor is a transition state mimic.⁸⁷ Figure 5.1 illustrates a thermodynamic cycle for an enzymatic reaction. The transition state species, S^\ddagger , is treated as being in a pseudo-equilibrium with the substrate species, S . The rate of breakdown of S^\ddagger to the product, P , is assumed to be the same for the catalyzed and uncatalyzed reactions, so the reaction rates are determined by the pseudo-equilibrium constants K_{uncat} and K_{cat} . (The transition state is not a stable species with a discrete lifetime, so it cannot formally be considered to be part of an equilibrium.) The activation energy for the transformation from $E + S$ to ES^\ddagger is the same regardless of the pathway travelled, such that the ratio of $K_{\text{TS}}/K_{\text{uncat}}$ must equal $K_{\text{S}}/K_{\text{cat}}$ (eq. 5.1).¹⁸⁸

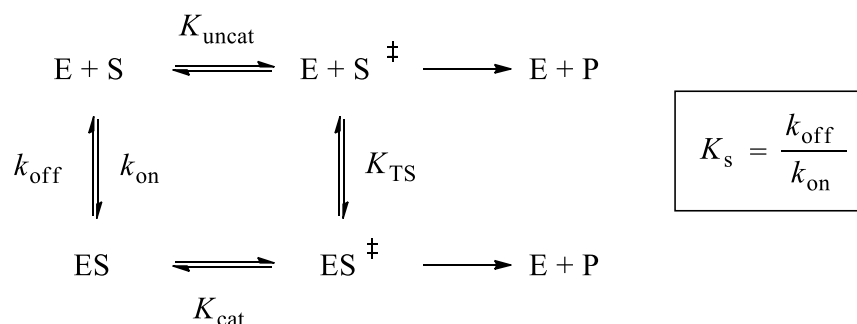


Figure 5.1: Thermodynamic cycle of enzyme binding substrate (S) and transition state (S[‡]).

$$K_{\text{TS}} = \frac{K_s}{K_{\text{cat}}} K_{\text{uncat}} \quad (5.1)$$

K_{uncat} and K_{cat} are pseudo-equilibrium constants that can be converted to reaction rates by applying the Eyring equation (eq. 5.2).¹⁸⁹⁻¹⁹¹

$$k = \kappa \frac{k_B T}{h} e^{-\frac{\Delta G}{RT}} \quad (5.2),$$

where k is the reaction rate. The $(k_B T/h)$ term is the frequency of the vibrational mode for transition state breakdown, where k_B is the Boltzmann constant, T is the temperature and h is Planck's constant. The transmission coefficient (κ), is a proportionality constant that accounts for the probability for product formation with each vibration, i.e., the probability of the transition state breaking down to P, rather than returning to S. ΔG is the free energy of activation derived from the relationship $\Delta G = -RT \ln(K)$. K_{TS} , is the theoretical dissociation constant of a perfect transition state analog. In reality this can never be attained because the transition state is unstable. K_{TS} can therefore be substituted with K_i ,¹⁹² the equilibrium dissociation constant of the inhibitor. In a single substrate reaction,

K_s , is the dissociation constant of substrate binding to the enzyme, measured as the ratio $k_{\text{off}}/k_{\text{on}}$. In eq. 5.1, K_s can be substituted with the Michaelis constant, K_M , defined as $(k_{\text{off}} + k_{\text{cat}})/k_{\text{on}}$. Substituting eq. 5.2 into eq. 5.1, and substituting K_{TS} and K_S with K_i and K_M , respectively, results in eq. 5.3.

$$K_i = \frac{K_M}{k_{\text{cat}}} k_{\text{uncat}} \quad (5.3)$$

As the Michaelis constant, K_M , is not a true dissociation constant, this only establishes a proportionality relationship between K_i and $K_M/k_{\text{cat}}*k_{\text{uncat}}$, rather than a direct equivalence. K_M/k_{cat} is a second order rate constant that reflects the activation energy from the free enzyme and substrate, $E + S$, to ES^\ddagger .⁹⁰ If an inhibitor is a transition state mimic, perturbations to the activation energy (i.e., changes in K_M/k_{cat}) should result in a proportional change in the value of K_i . A plot of $\log(K_i)$ vs. $\log(K_M/k_{\text{cat}})$, should yield a straight line if an inhibitor is acting as a transitions state mimic (eq. 5.4).

$$\log(K_i) = \log\left(\frac{K_M}{k_{\text{cat}}}\right) + \log(k_{\text{uncat}}) \quad (5.4)$$

LFER studies are commonly carried out on single substrate enzymes, which allows for direct comparison of $\log(K_M/k_{\text{cat}})$ with $\log(K_i)$; however, a modified approach is needed for multi-substrate systems.^{87,192} The DAHPS reaction may be regarded as a two substrate (PEP and E4P) or a three substrate (PEP, E4P and Mn^{2+}) reaction. In order to correctly analyze LFER data, it is necessary to account for both (or all three) substrates' K_M values.¹⁹²⁻¹⁹⁴ The

To investigate whether DAHP oxime binds as a transition state mimic, we set out to test whether a linear free energy relationship exists between $\log(K_M/k_{cat})$ and $\log(K_i)$ for a series of DAHPS_{H6} mutants. Our data suggest that DAHP oxime is a transition state inhibitor of DAHPS_{H6}.

5.2. Materials and Methods

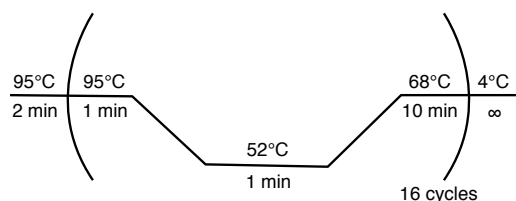
5.2.1. DAHPS_{H6} Mutagenesis

Mutant DAHPS_{H6}'s were generated using Stratagene's QuikChange® Site-Directed Mutagenesis Kit. The primers (Table 5.1) were thermo-cycled (Figure 5.3), and the reaction mixtures were treated for 1 h at 37°C with 1 unit of DpnI to cleave all parental DNA. DpnI-treated samples (10 µL) were run on 1% agarose gel to visualize the product. Successful reactions were transformed into *E. coli* AG1 cells and plated on LB/agar with 10 µg/mL chloramphenicol. Single colonies were grown overnight in 50 mL LB with 10 µg/mL chloramphenicol. DNA was isolated from these cultures using QIAgen Miniprep kit, and sequenced to confirm successful mutagenesis.

Table 5.1: Mutagenesis primers.

The terminal "F" or "R" refers to the forward and reverse primers, respectively.

Name	Primers 5' – 3'
H268AF	CAGGTGATGATCGATTTTCAGCGCCGCTAACTCGTCCAAACAATTC
H268AR	GAATTGTTTGGACGAGTTAGCGGGCGCTGAAATCGATCATCACCTG
R99AF	GCGTCTATTTTAAAAGCCGGCAACCACGGTGGGCTGGAAAGGG
R99AR	CCCTTTCCAGCCCACCGTGGTTGCCGGCTTTTCAAATAGACGC
T100AF	CGTCTATTTTAAAAGCCGCGTGCCACGGTGGGCTGGAAAGGGC
T100AR	GCCCTTTCCAGCCCACCGTGGCACGCGGCTTTTCAAATAGACGC
D326AF	CGGTAAGAGCATCACCGCTGCCTGCATCGGCTGG
D326AR	CCAGCCGATGCAGGCAGCGGTGATGCTCTTACCG
K186AF	GGCTTTCTTGTCCGGTCGGCTTCGCAAATGGCACCGACGGTACG
K186AR	CGTACCGTCGGTGCCATTTGCGAAGCCGACCGGACAAGAAAGCC
C61AF	GTGATTGGCCCAGCCTCAATTCATGATCCTGTGCGCGGC
C61AR	GTGATTGGCCCAGCCTCAATTCATGATCCTGTGCGCGGC
C328AF	GGTAAGAGCATCACCGATGCCGCCATCGGCTGGGAAGATACCG
C328AR	CGGTATCTTCCCAGCCGATGGCGGCATCGGTGATGCTCTTACC

**Figure 5.3: Temperature cycling method used for mutagenesis.**

5.2.2. Expression and purification of Mutant DAHPS_{H6}'s

N-terminally His₆-tagged mutant DAHPS_{H6}'s in pCA24N plasmids were transformed and expressed in *E. coli* K-12 Δ aroG^{195,196} (cells were obtained from Dr. Eric Brown, McMaster University), and purified, as described for DAHPS_{H6} in Chapter 2. This work was carried out by Frederick To.¹⁹⁵

5.2.3. DAHPS_{H6} Mutant Kinetics/Inhibition

Steady state kinetic parameters and K_i 's for DAHPS_{H6} mutants were determined by Frederick To as described in Chapter 2.¹⁹⁵

One mutant enzyme, D326A, displayed apparent substrate inhibition by PEP. A term was added to eq. 2.1 to account for substrate inhibition by PEP, assuming it bound to the E•Mn²⁺•PEP Michaelis complex in the E4P binding site (eq. 5.8):

$$\frac{v_0}{[E]_0} = \frac{k_{cat}[A][B][C]}{K_A K_B K_C} \frac{1}{1 + \frac{[A]}{K_A} + \frac{[A][B]}{K_A K_B} \left(1 + \frac{[B]}{K_{i,B}}\right) + \frac{[A][B][C]}{K_A K_B K_C}} \quad (5.8),$$

where B is PEP and $K_{i,PEP}$ is the inhibition constant due to PEP. Equations 2.1a and 2.1b were similarly modified to fit $K_{i,PEP}$.

5.3. Results

DAHPS_{H6} mutants were expressed in an *aroG* knockout strain, *E. coli* K-12 Δ *aroG*¹⁸⁹ because even small amounts of endogenously expressed DAHPS could have interfered with activity measurements on low activity mutants.

The residues to be mutated were selected based on their interactions with DAHP oxime or proximity to the active site (Figure 5.4). Residues R99, T100, K186, and D326 made direct contacts with DAHP oxime. D326 made contact with Mn²⁺ in structure MJ108_1_7, and in literature structures (e.g., 1N8F,¹³⁶ and 1KFL⁵⁵), but no structure containing both a metal ion and a ligand with the

equivalent of O4 and O6 of DAHP oxime (see Figure 5.4) exists, so it is not known whether the D326 sidechain can form both interactions simultaneously. Residue H268 made contact with the D326 sidechain, presumably forming an ion pair or ion-neutral hydrogen bond. Residue C61 is one of the metal coordinating residues in metal ion-containing structures. Residue C328 was selected for being close to the active site, but not in contact with the inhibitor or metal ion.

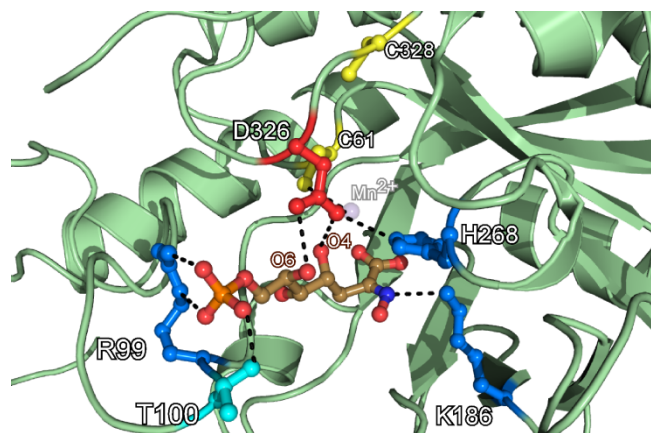


Figure 5.4: DAHPS_{H6} mutants.

Mutated residues are shown, along with their interactions with DAHP oxime or Mn²⁺ (black dashed lines) in subunit C of structure Wai003_4_10. Atoms O4 and O6 of DAHP oxime are labelled. The position of Mn²⁺, which was not present in Wai003_4_10, was taken from structure 1N8F.¹³⁶ (Figure created by P. Berti.)

The steady state kinetic parameters of the mutant DAHPS_{H6}'s were determined, along with the K_i values for fast binding inhibition (Table 5.2). Mutant H268A was unstable; it lost activity almost immediately upon purification and was not characterized kinetically.

Table 5.2: Steady state kinetic parameters for DAHPS_{H6} and mutants^a.

Enzyme	$k_{\text{cat}}/(K_{\text{M,Mn}}K_{\text{M,PEP}}K_{\text{M,E4P}})$ ($\text{M}^{-3}\text{s}^{-1}$)	k_{cat} (s^{-1})	$K_{\text{M,Mn}}$ (M)	$K_{\text{M,PEP}}$ (M)	$K_{\text{M,E4P}}$ (M)	K_i (M)
T100A	$(8.4 \pm 0.8) \times 10^{13}$	8.7 ± 0.9	$(1.1 \pm 0.1) \times 10^{-5}$	$(2.4 \pm 0.3) \times 10^{-5}$	$(3.6 \pm 0.5) \times 10^{-4}$	$(6 \pm 2) \times 10^{-6}$
C328A	$(2.8 \pm 0.7) \times 10^{13}$	17 ± 1	$(1.5 \pm 0.4) \times 10^{-5}$	$(2.5 \pm 0.5) \times 10^{-4}$	$(1.5 \pm 0.3) \times 10^{-4}$	$(6 \pm 2) \times 10^{-8}$
D326A ^b	$(2.4 \pm 0.4) \times 10^{11}$	1.5 ± 0.1	$(5 \pm 1) \times 10^{-4}$	$(3.6 \pm 0.9) \times 10^{-5}$	$(4 \pm 1) \times 10^{-4}$	$(1.8 \pm 0.5) \times 10^{-5}$
C61A	$(5.9 \pm 0.6) \times 10^8$	0.19 ± 0.06	$(9 \pm 1) \times 10^{-5}$	$(5.9 \pm 0.8) \times 10^{-4}$	$(6 \pm 2) \times 10^{-3}$	$(3.8 \pm 0.6) \times 10^{-4}$
R99A	$(1.7 \pm 0.2) \times 10^8$	2.6 ± 0.2	$(3.1 \pm 0.5) \times 10^{-4}$	$(1.4 \pm 0.3) \times 10^{-3}$	$(3.5 \pm 0.6) \times 10^{-2}$	$(6 \pm 2) \times 10^{-4}$
K186A	$(2.7 \pm 0.2) \times 10^7$	0.16 ± 0.01	$(3 \pm 2) \times 10^{-4}$	$(1.0 \pm 0.3) \times 10^{-1}$	$(1.8 \pm 0.4) \times 10^{-4}$	$(3.1 \pm 0.9) \times 10^{-4}$
DAHPS _{H6} ^c	$(1.5 \pm 0.2) \times 10^{15}$	16.4 ± 0.6	$(5.5 \pm 0.7) \times 10^{-6}$	$(1.4 \pm 0.2) \times 10^{-4}$	$(1.5 \pm 0.2) \times 10^{-5}$	$(1.7 \pm 0.5) \times 10^{-6}$

^a Initial velocity data were fitted to eq. 2.1 for steady state kinetic parameters, and eq. 2.3 for K_i .

^b The steady state kinetic parameters for D326A were fitted to eq. 5.8, which took into account the observed substrate inhibition by PEP. $K_{i,\text{PEP}} = (1.3 \pm 0.5) \times 10^{-3}$ M.

^c From Table 2.1.

Table 5.3: Catalytic impairment by mutations^a.

Enzyme	Relative $k_{\text{cat}}/(K_{\text{M,Mn}}K_{\text{M,PEP}}K_{\text{M,E4P}})$	Relative k_{cat}	Relative $1/K_{\text{M,Mn}}$	Relative $1/K_{\text{M,PEP}}$	Relative $1/K_{\text{M,E4P}}$	Relative $1/K_i$
T100A	17	2	2	0.2	24	3
C328A	53	1	3	2	10	0.03
D326A	6×10^3	11	88	0.3	25	11
C61A	2×10^6	88	16	4	439	221
R99A	9×10^6	6	56	10	2412	375
K186A	5×10^7	104	61	682	12	184
DAHPS _{H6}	1	1	1	1	1	1

^a The decrease in k_{cat} or $k_{\text{cat}}/(K_{\text{M,Mn}}K_{\text{M,PEP}}K_{\text{M,E4P}})$ or increase in K_i or K_M values relative to wild-type enzyme.

For example, relative $k_{\text{cat}} = k_{\text{cat,wild-type}}/k_{\text{cat,mutant}}$, and relative $K_i = K_{i,\text{mutant}}/K_{i,\text{wild-type}}$.

Plots of $\log[K_i]$ vs. $\log[(K_{M,PEP} \cdot K_{M,E4P})/k_{cat}]$ demonstrated a strong linear correlation ($R^2 = 0.96$, slope = 0.41) for the two substrates model (Figure 5.5a). The three substrates model, i.e., $\log[K_i]$ vs. $\log[(K_{M,Mn} \cdot K_{M,PEP} \cdot K_{M,E4P})/k_{cat}]$ yielded a similarly strong linear relationship ($R^2 = 0.95$, slope = 0.33) (Figure 5.5b). In both graphs, C328A was excluded from the linear regression, as it was consistently an outlier.

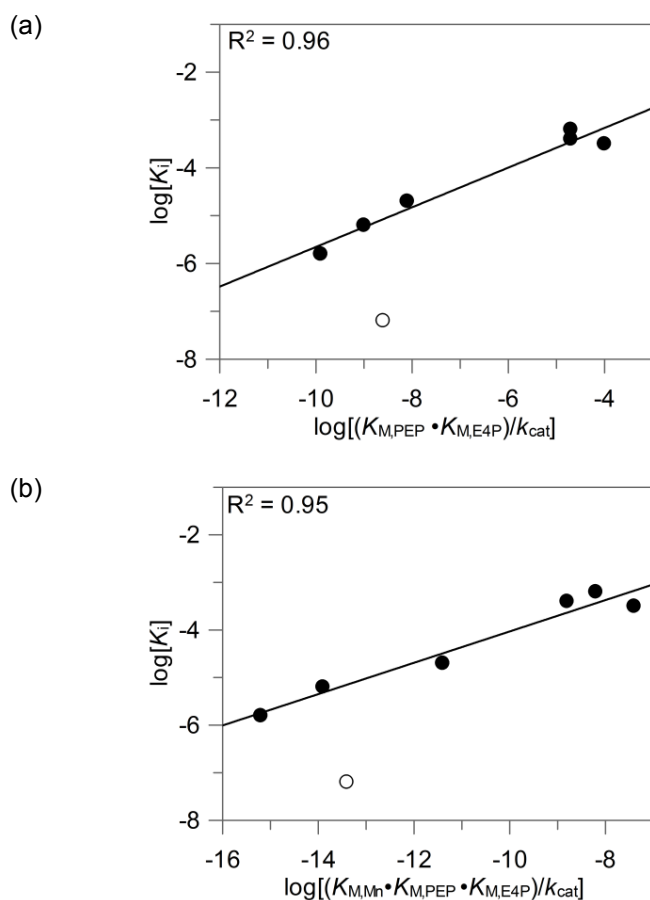


Figure 5.5: Linear free energy relationships for DAHP oxime.

K_i and K_M/k_{cat} values for mutant DAHP_{S_{H6}}'s establish DAHP oxime as a transition state inhibitor. (a) Two substrates model: $\log[K_i]$ vs. $\log[(K_{M,PEP} \cdot K_{M,E4P})/k_{cat}]$, slope = 0.41. (b) Three substrates model: $\log[K_i]$ vs. $\log[(K_{M,Mn} \cdot K_{M,PEP} \cdot K_{M,E4P})/k_{cat}]$, slope = 0.33. C328A (open circles) was not included in the linear fits, as it was an outlier in both graphs.

5.4. Discussion

(For simplicity, " K_M/k_{cat} " in the following sections is used generically to refer to one or both of the more complex parameters $(K_{M,PEP} \cdot K_{M,E4P})/k_{cat}$ and/or $(K_{M,Mn} \cdot K_{M,PEP} \cdot K_{M,E4P})/k_{cat}$.

5.4.1. Effects of Mutations

The effects of mutations on the steady state kinetic parameters spanned a wide range; from a 17-fold decrease in $k_{cat}/(K_{M,Mn}K_{M,Mn}K_{M,E4P})$ for T100A, to 5×10^7 -fold for K186A (Table 5.3).

The largest effects on k_{cat} were with mutations to residues directly involved in catalysis. The largest effect was a 100-fold decrease observed for K186A. K186 is proposed to form a ion/neutral hydrogen bond with the phosphate bridging oxygen of PEP and the THI, and to act as a general acid catalyst in phosphate departure during THI breakdown.^{52,118} The C61A mutation reduced k_{cat} 90-fold, consistent with its role in coordinating the metal ion. Another mutation affecting a metal-binding residue, D326A, caused a 10-fold decrease in k_{cat} . Mutations to residues that do not have an obvious catalytic role had smaller effects on k_{cat} , i.e., 6- and 2-fold, respectively for R99A and T100A, while the remote mutation C328A had no apparent effect on k_{cat} .

In general, the effects of mutations on K_M values were consistent with what would be expected based on crystal structures. For example, the greatest increase in $K_{M,E4P}$ was with R99A, which forms an ion pair with E4P's phosphate

group in crystal structures, while the biggest increase in $K_{M,PEP}$ was observed with K186A, which interacts with the phosphate group's bridging oxygen. Other changes were less easy to rationalize, such as the fact that the C61A mutation caused a larger increase in $K_{M,E4P}$, with which it does not make contact, than $K_{M,Mn}$, which it does coordinate. This illustrates the danger in interpreting K_M values as simple equilibrium dissociation constants; K_M values in multisubstrate, multistep reactions include unknown contributions from the rate constants in individual steps.

5.4.2. LFER Analysis

The linear relationship between $\log[K_i]$ and both $\log[(K_{M,Mn} \cdot K_{M,PEP} \cdot K_{M,E4P})/k_{cat}]$ (the three substrates model) and $\log[(K_{M,PEP} \cdot K_{M,E4P})/k_{cat}]$ (the two substrates model) (Figure 5.5) indicated that DAHP oxime is indeed a transition state mimic. In principle, the plot of $\log[K_i]$ vs. $\log[K_M/k_{cat}]$ should have slope = 1, whereas the slopes for DAHPS_{H6} were 0.41 for the two substrates model, and 0.33 for three substrates. This is discussed in detail below.

It was not obvious *a priori* whether it would be more appropriate to compare K_i with the two substrates or the three substrates model. Mn^{2+} does not undergo a chemical change during catalysis, and is not generally treated as a substrate.^{117,119} However, the metal dependence of inhibition and mutually exclusive binding of Mn^{2+} and DAHP oxime (see Section 2.3.5) suggested that

Mn^{2+} should be treated as a substrate in LFER analysis. In addition, though the metal ion is not itself changed, it has been proposed to participate in catalysis, by polarizing the carbonyl oxygen, O1, of E4P.^{52,53,118,133,136} In addition, the crystal structures suggest that O1 of E4P would be within 2.5 Å of Mn^{2+} , assuming that it bound in the same position as the O4 hydroxyl oxygen of DAHP oxime (see Chapter 3). Thus, it is reasonable to presume that the metal ion interacts with the transition state and that mutations that affect metal binding would also effect the transition state energy. Ultimately, the results of LFER analysis with both the two and three substrate models were essentially the same; that is, both models indicated that DAHP oxime is a transition state mimic.

5.4.3. Transition state mimicry

The LFER graphs identified a correlation between the K_i of DAHP oxime and K_M/k_{cat} of the substrates, thus implying that DAHP oxime is a transition state mimic. However, LFER analysis does not identify which transition state is being mimicked. Based on the proposed mechanism (Figure 1.7, path A), a THI is formed and broken down with associated transition states for its formation and breakdown. From the crystal structures, the nitrogen of the oxime is in hydrogen bonding distance to the K186 ϵ -amino group. THI breakdown will be acid catalyzed,^{197,198} where protonation of the bridging oxygen leads to C-O bond cleavage and phosphate departure. In DAHPS, the K186 ϵ -amino group, is the proposed general acid catalyst. In contrast, a strong interaction of K186 with the

bridging oxygen during THI formation is unlikely, as this interaction would be anticatalytic, as it would tend to withdraw electrons from the nucleophilic PEP molecule during C-C bond formation. Therefore, the transition state being mimicked is that of THI breakdown, where C-O bond cleavage during phosphate departure is catalyzed by the ϵ -amino group of K186 (Figure 1.7). As there is no crystal structure of the DAHPS•THI complex, we compared a DAHPS•PEP complex (1N8F) with DAHPS•DAHP oxime to rationalize the potency of DAHP oxime binding. PEP is bound through numerous contacts, including ion pairs between Arg sidechains and PEP's carboxylate and phosphate moieties, plus the ion/neutral hydrogen bond between the K186 ϵ -amino group and the phosphate bridging oxygen (Figure 5.6). During THI breakdown, the K186 ϵ -amino group could act as a general acid catalyst to protonate the bridging oxygen and promote phosphate departure. Previous experimental and computational studies have shown that the only way to promote C-O bond cleavage for phosphate departure is to protonate the bridging oxygen (see reference,¹⁹⁸ and references therein).

In the DAHP oxime-bound structure, most of these interactions were conserved. Two crystallographic waters were present that overlaid in good agreement with the positions of the two non-bridging oxygens of the PEP phosphate group from structure 1N8F (Figure 5.6).¹³⁶

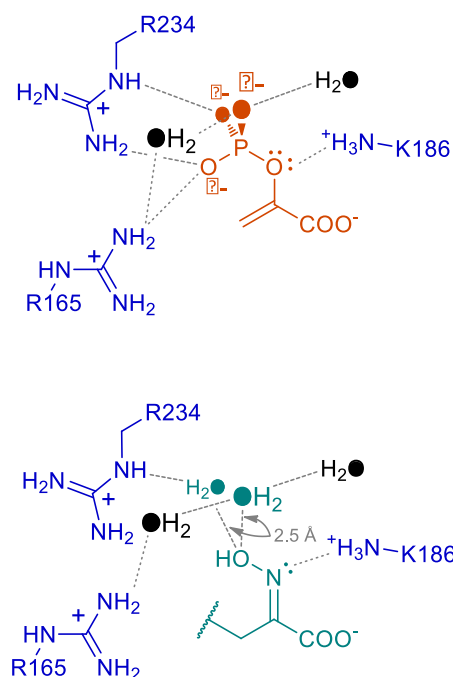


Figure 5.6: DAHP oxime vs. PEP binding.

(Upper) Active site of 1N8F crystal structure showing phosphate contacts of PEP with DAHPS. (Lower) active site of Wai003_4_10 showing contacts of the oxime moiety with the DAHPS_G. The two phosphate oxygens (coloured solid red) have two water molecules occupying the same space in the DAHP oxime-bound structure.

5.4.4. LFER Slopes

In principle, a perfect transition state mimic would have a linear relationship between $\log[K_i]$ vs. $\log[K_M/k_{\text{cat}}]$ with slope = 1. The slopes for DAHPS_{H6} were 0.41 for the two substrates model, and 0.33 for the three substrates model. This implies that while DAHP oxime does mimic the transition state, the interaction of the oxime functional group is not as strong as the transition state interaction it is mimicking.

The slopes of less than unity may arise from two sources, namely the nature of the oxime functional group, and from the fact that this is multi-step reaction.

One source of difference would stem from differences in the ligand atoms that interact with the K186 ϵ -amino group. The phosphate bridging oxygen atom of the THI is substituted with a less electronegative nitrogen atom in DAHP oxime, which would be expected to lead to weaker hydrogen bonding in the inhibitor than in the transition state for THI breakdown. This, in turn, would be reflected in a weaker dependence of K_i than K_M/k_{cat} on mutations.

In addition, deviation of the slope from unity could be a result of K_M/k_{cat} including a contribution from THI formation, as well as THI breakdown. K_M/k_{cat} is a measure of the change in energy from free enzyme and substrate to the first irreversible step, TS. If all of the molecules that reach the TS proceed to product, then the TS formation will represent the first irreversible step and K_M/k_{cat} will reflect that TS. However, if there are partially irreversible steps within the pathway, then K_M/k_{cat} will reflect all partially irreversible steps. For example, while the THI breakdown to products is irreversible, we do not know whether THI formation is also irreversible. If THI formation is reversible and the reverse reaction rate is comparable to the forward breakdown of the THI to product, then the K_M/k_{cat} would reflect the transition states of both THI formation and breakdown. If DAHP oxime mimics the transition state of THI breakdown only, and not THI formation, then slope of $\log[K_i]$ vs. $\log[K_M/k_{cat}]$ will be less than unity.

5.4.5. *Transition State versus Substrate Mimicry*

Given the structural similarity between the substrate molecules and most of the DAHP oxime structure (i.e., everything but the oxime functional group itself), it is possible to argue that DAHP oxime acts only as a substrate mimic, and not as a transition state mimic. It is true that the relationship between K_i and K_M/k_{cat} is dominated by changes in the K_M values, as illustrated by the fact that plots of $\log[K_i]$ vs. $\log[(K_{M,\text{Mn}} \cdot K_{M,\text{PEP}} \cdot K_{M,\text{E4P}})]$ and $\log[K_{M,\text{PEP}} \cdot K_{M,\text{E4P}}]$ have R^2 values and slopes similar to plots of $\log[K_i]$ vs. $\log[K_M/k_{\text{cat}}]$ (compare Figure 5.7 with Figure 5.5). However, it is important to remember that K_M values are not simple measures of affinity, but also include contributions from kinetic steps. In addition, a plot of $\log[K_i]$ vs. $\log[1/k_{\text{cat}}]$ revealed a clear relationship between catalysis and inhibitor binding (Figure 5.8). There was one outlier in that relationship, R99A, which had a k_{cat} value higher than expected based on its K_i value, but the overall trend is clear.

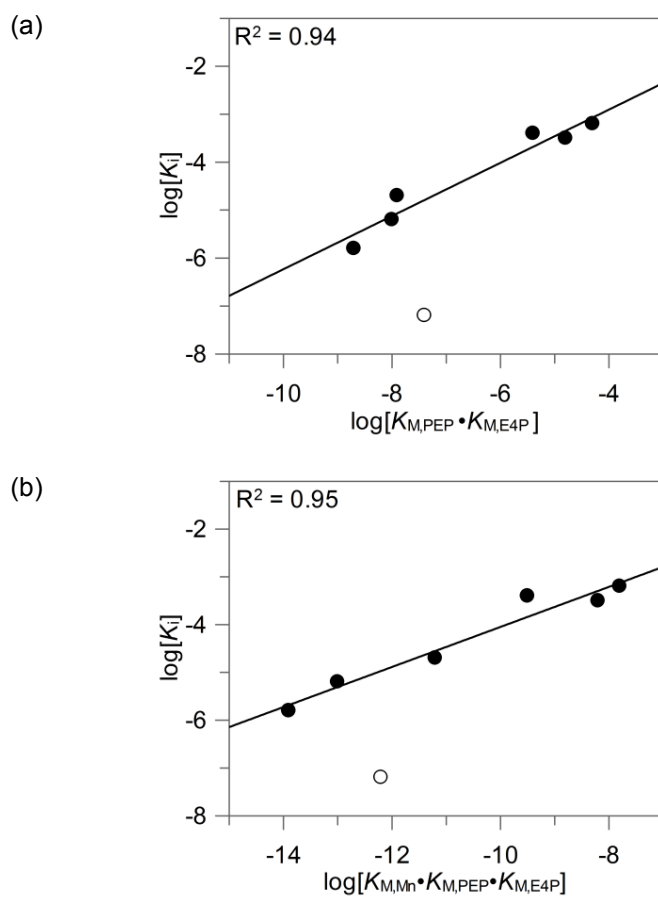


Figure 5.7: Linear correlation of K_i of DAHP oxime with K_M values

Inhibition vs. K_M values illustrates the multisubstrate-like character of DAHP oxime binding. (a) For two substrates, $\log[K_i]$ vs. $\log[K_{M,PEP} \cdot K_{M,E4P}]$ yielded $R^2 = 0.94$, slope = 0.55. (b) For three substrates, $\log[K_i]$ vs. $\log[K_{M,Mn} \cdot K_{M,PEP} \cdot K_{M,E4P}]$ yielded $R^2 = 0.95$, slope = 0.42. C328A (open circles) was not included in the linear fits, as it was an outlier in both graphs.

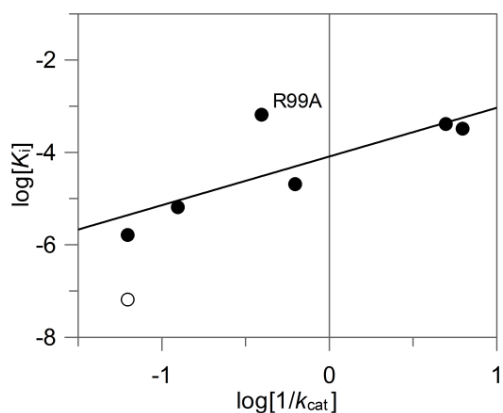


Figure 5.8: Linear correlation of K_i for DAHP oxime with k_{cat}

The $\log[K_i]$ vs. $\log[1/k_{cat}]$ plot illustrates the relationship between inhibition and catalysis. R99A was an outlier; slope = 1.0 and $R^2 = 0.61$ including R99A, slope = 1.1 and $R^2 = 0.98$ without it. C328A (open circle) was not included in the linear fits, as it was an outlier in all graphs.

In summary, DAHP oxime's effectiveness as an inhibitor arises from its mimicking the transition state for THI breakdown during catalysis. We have established DAHP oxime as a transition state inhibitor of DAHPS through LFER analysis. From the LFER analysis, DAHP oxime does not capture the entirety of transition state stabilization, as weaker hydrogen bonding to the oxime group's nitrogen atom, in comparison to the bridging oxygen of the phosphate in the THI weakens the transition state-like character of the oxime. It is also possible that THI breakdown is not the first fully irreversible step, which would also tend to decrease the slope below unity.

Chapter 6 - Concluding Remarks

6.1. Conclusions

In this work, we demonstrated that DAHP oxime is a transition state inhibitor of DAHPS. There was fast-binding inhibition, with $K_i = 1.7 \mu\text{M}$, and slow-binding inhibition. The onset rate of slow-binding inhibition was 0.24 min^{-1} , and the dissociation rate was 0.012 min^{-1} ($t_{1/2} = 58 \text{ min}$). Together, these gave an ultimate equilibrium inhibition constant of $K_i^* = 81 \text{ nM}$, the tightest binding of any known DAHPS inhibitor. DAHP oxime displayed mixed type inhibition, where the inhibitor binds to two of the four subunits of the DAHPS homotetramer. In the bound subunits, inhibitor binding is competitive with respect to the substrates. In the unbound subunits, inhibition is noncompetitive with respect to substrate binding as the substrates' K_M values remained constant, while k_{cat} was reduced.

X-ray crystallography revealed that DAHP oxime bound to only two subunits (B and C) of the four in DAHPS. Structurally, inhibitor-bound subunits (B and C) and unbound subunits (A and D) were similar, except in four regions; mainly D6-E12, F95-K105, G188-T192, and L312-L318. DAHP oxime-bound subunits were essentially identical to PEP-bound subunits, suggesting that the inhibitor induced the same enzyme conformation as the substrates.

The fact that only two subunits bound inhibitor explained the observed residual rate at high inhibitor concentrations. However, given the similarity in structure between PEP-bound DAHPS structures in literature and the inhibitor-

bound structures in this study, and the similarity between the DAHP oxime-bound and inhibitor-free subunits, it was not clear what caused the strong negative cooperativity between subunits A and B (and C and D). H/D exchange experiments helped address this discrepancy. They indicated that DAHPS_G is a dynamic enzyme that is structured in the core, and along both the tight dimer interface (i.e., between the A and B subunits, and between C and D) and the loose dimer interface (i.e., between the AB and CD dimers), but weakly structured in many surface loops, includes those surrounding the active site. Addition of PEP caused significant stabilization of DAHPS_G dynamics. Addition of DAHP oxime also caused stabilization of the enzyme; however, not to the extent observed with PEP. This suggests that changes in loop dynamics upon inhibitor binding could be the source of the observed negative cooperativity (half-of-sites binding), rather than distinct structural changes.

Through this work we have presented a new inhibitory motif that is a transition state mimic inhibitor of DAHPS. The oxime motif can now serve as a scaffold to create derivatives to study structure-activity relationships and to create more potent inhibitors. We have also presented evidence that DAHPS dynamics plays an important role in enzyme function.

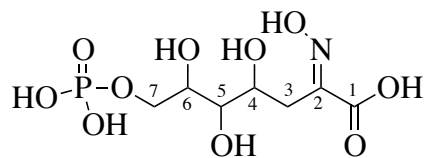
6.2. Future work

Our data suggest DAHPS dynamics plays an important role in its function. DAHP oxime binds to two of the available four subunits. The question remains as to why all four subunits are not bound. It is possible that DAHP oxime binding in

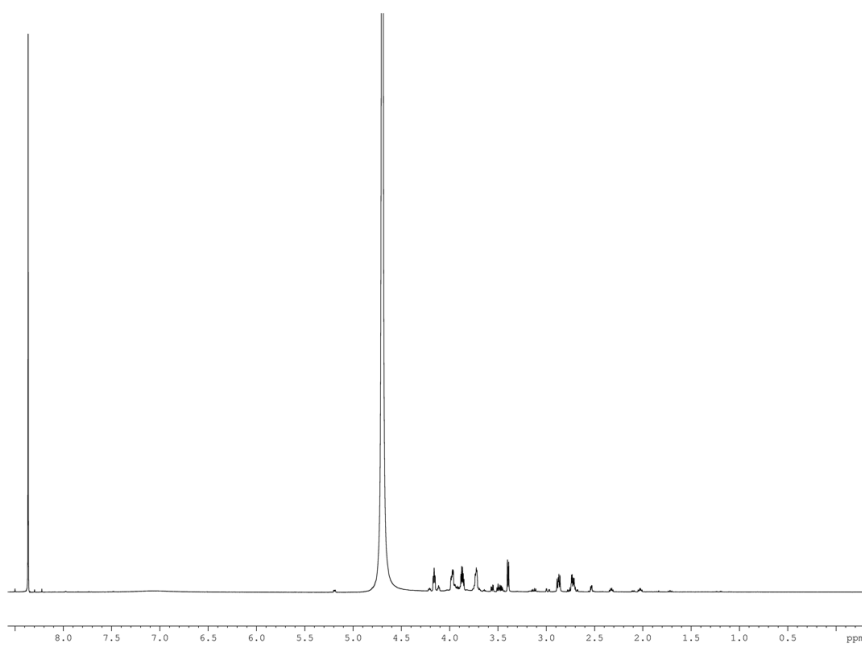
subunit B (C), induces conformational and/or dynamic changes in the unbound subunit A (D). This can be investigated with ^{19}F NMR. The use of ^{19}F NMR to study structural asymmetry in DAHPS(Phe) was not successful; however, preliminary results with the homodimeric DAHPS(Tyr) has shown promise. The commercial availability of fluorinated aromatic amino acids would allow for extensive mapping of local dynamics within the enzyme. Within the DAHPS(Tyr) monomer, each ^{19}F -labelled residue would appear as an individual peak. In a symmetric dimer, equivalent residues would overlap. However, if there were asymmetry within the dimers, the differences would appear as a doubling of the number of visible peaks, as equivalent residues in each subunit would experience different environments. This information would be useful in investigating regions where asymmetry is introduced upon inhibitor binding, and shed light on dynamic signaling within the enzyme.

DAHPS oxime binds to two of the four available active sites, with the unbound active sites remaining catalytically active. This half-of-site activity can be explored using hybrid DAHPSs, that is, DAHPS in which one subunit is active and the other is inactive. Creating chimeric enzymes of tetramers would be difficult with respect to controlling ratios of active vs. inactive subunits in a homotetramer, but in a dimer the ratios could be controlled. Study of the kinetic parameters of the hybrid enzyme would be useful in explaining the half-of-sites activity as to the extent of interaction between subunits in substrate binding and catalysis.

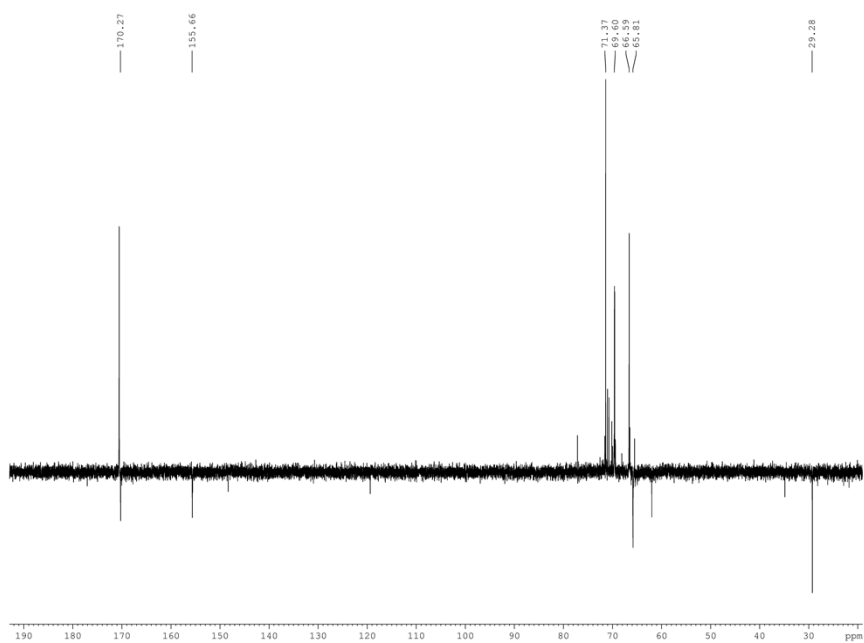
Preliminary experiments with DAHP *O*-fluoroethyloxime, and more recently with DAHP hydrazone, have shown inhibition to be complete, i.e., with no residual rate. Whether this is due to inhibitor binding in all four subunits or whether inhibitor binding in two subunits (B and C) abolishes activity in subunits A and D is not known. Crystallization of DAHPS with DAHP *O*-fluoroethyloxime will address subunit occupancy. H/D deuterium exchange studies with DAHP *O*-fluoroethyloxime will shed light on the dynamic differences (if any) upon DAHP *O*-fluoroethyloxime binding.

Appendix

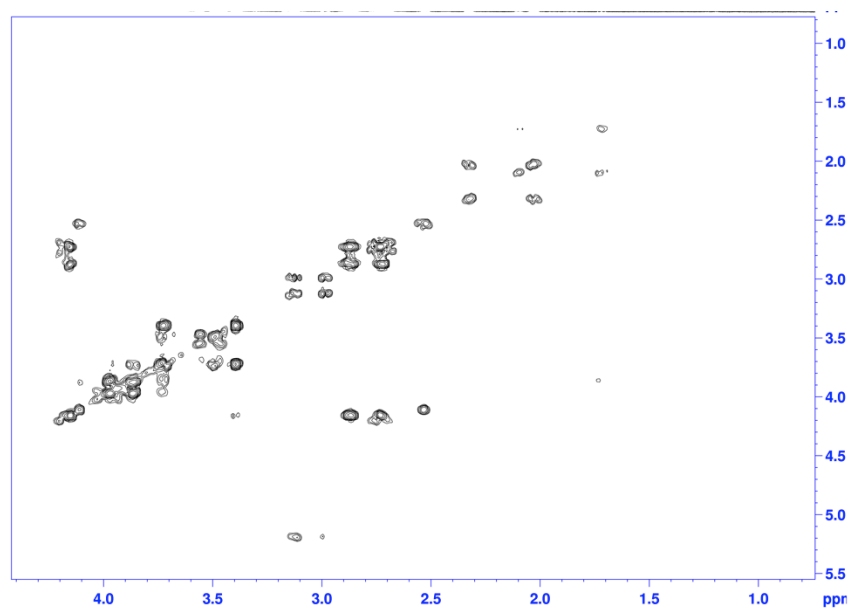
(a)



(b)



(c)



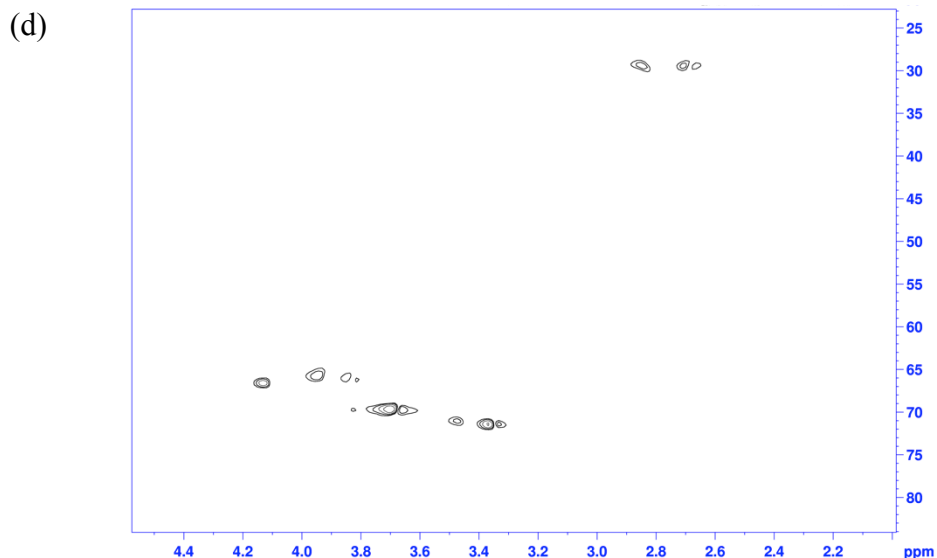


Figure A.1: NMR spectrum of DAHP oxime.

Spectrum was acquired on a 700 MHz NMR spectrometer in D₂O. (a) ¹H, (b) ¹³C, (c) COSY, (d) HSQC.

Table A.1: ¹H and ¹³C assignment of DAHP oxime.

Proton	¹ H δ (ppm)	J _{H-H}	Carbon	¹³ C δ (ppm)
H3	2.73	(dd) 13.28, 5.73	C1	170.27
H3'	2.87	(dd) 13.2, 8.43	C2	155.66
H4	4.17	(m)	C3	29.28
H5	3.4	(dd) 8.92, 1.3	C4	66.59
H6	3.74	(ddd) 8.34, 5.42, 2.43	C5	71.37
H7	3.88	(m)	C6	69.60
H7'	3.99	(ddd) 11.05, 5.64, 2.37	C7	65.81

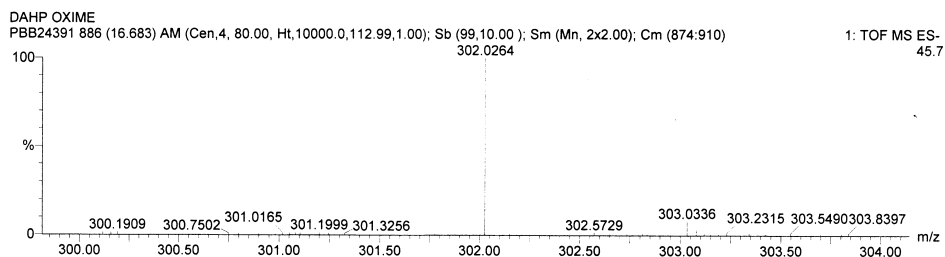


Figure A.2: High resolution mass spectrum of DAHP oxime

Calculated mass of the M-1 peak is 302.0277 Da.

References

- (1) Bush, K. (2004) Antibacterial drug discovery in the 21st century. *Clin. Microbiol. Infect.* 10 Suppl 4, 10–17.
- (2) Abraham, E. P., and Chain, E. (1940) An Enzyme from Bacteria able to Destroy Penicillin. *Nature* 146, 837–837.
- (3) Davies, J., and Davies, D. (2010) Origins and evolution of antibiotic resistance. *Microbiol. Mol. Biol. Rev.* 74, 417–433.
- (4) Edgar, T., Boyd, S. D., and Palamé, M. J. (2009) Sustainability for behaviour change in the fight against antibiotic resistance: a social marketing framework. *J. Antimicrob. Chemother.* 63, 230–237.
- (5) Wright, G. D. (2003) Mechanisms of resistance to antibiotics. *Curr Opin Chem Biol* 7, 563–569.
- (6) Coates, A., Hu, Y., Bax, R., and Page, C. (2002) The future challenges facing the development of new antimicrobial drugs. *Nat. Rev. Drug. Discov.* 1, 895–910.
- (7) Allen, H. K., Donato, J., Wang, H. H., Cloud-Hansen, K. A., Davies, J., and Handelsman, J. (2010) Call of the wild: antibiotic resistance genes in natural environments. *Nat. Rev. Microbiol.* 8, 251–259.
- (8) Walsh, C. (2003) Where will new antibiotics come from? *Nat. Rev. Microbiol.* 1, 65–70.
- (9) Jabes, D. (2011) The antibiotic R&D pipeline: an update. *Curr. Opin. Microbiol.* 14, 564–569.
- (10) Wright, G. D. (2012) Antibiotics: a new hope. *Chem. Biol.* 19, 3–10.
- (11) Rice, L. B. (2008) Federal funding for the study of antimicrobial resistance in nosocomial pathogens: no ESKAPE. *J. Infect. Dis.* 197, 1079–1081.
- (12) Kumarasamy, K. K., Toleman, M. A., Walsh, T. R., Bagaria, J., Butt, F., Balakrishnan, R., Chaudhary, U., Doumith, M., Giske, C. G., Irfan, S., Krishnan, P., Kumar, A. V., Maharjan, S., Mushtaq, S., Noorie, T., Paterson, D. L., Pearson, A., Perry, C., Pike, R., Rao, B., Ray, U., Sarma, J. B., Sharma, M., Sheridan, E., Thirunarayan, M. A., Turton, J., Upadhyay, S., Warner, M., Welfare, W., Livermore, D. M., and Woodford, N. (2010) Emergence of a new antibiotic resistance mechanism in India, Pakistan, and the UK: a molecular, biological, and epidemiological study. *Lancet Infect. Dis.* 10, 597–602.

- (13) Kresse, H., Belsey, M. J., and Rovini, H. (2007, January) The antibacterial drugs market. *Nat. Rev. Drug. Discov.*
- (14) (2010) The 10 × '20 Initiative: Pursuing a Global Commitment to Develop 10 New Antibacterial Drugs by 2020. *Clin. Infect. Dis.* 50, 1081–1083.
- (15) Herrmann, K. M., and Weaver, L. M. (1999) The Shikimate Pathway. *Annu. Rev. Plant Physiol. Plant Mol. Biol.* 50, 473–503.
- (16) DeLeo, A. B., Dayan, J., and Sprinson, D. B. (1973) Purification and kinetics of tyrosine-sensitive 3-deoxy-D-arabino-heptulosonic acid 7-phosphate synthetase from Salmonella. *J. Biol. Chem.* 248, 2344–2353.
- (17) Srinivasan, P. R., and Sprinson, D. B. (1959) 2-Keto-3-deoxy-D-arabino-heptonic acid 7-phosphate synthetase. *J. Biol. Chem.* 234, 716–722.
- (18) Bentley, R., and Haslam, E. (1990) The shikimate pathway--a metabolic tree with many branches. *Crit. Rev. Biochem. Mol. Biol.* 25, 307–384.
- (19) M Dewick, P. (1998) The biosynthesis of shikimate metabolites. *Nat. Prod. Rep.* 15, 17–58.
- (20) Grison, C., Petek, S., Finance, C., and Coutrot, P. (2005) Synthesis and antibacterial activity of mechanism-based inhibitors of KDO8P synthase and DAH7P synthase. *Carbohydr. Res.* 340, 529–537.
- (21) Steinrücken, H. C., and Amrhein, N. (1980) The herbicide glyphosate is a potent inhibitor of 5-enolpyruvyl-shikimic acid-3-phosphate synthase. *Biochem. Biophys. Res. Commun.* 94, 1207–1212.
- (22) Mutunga, M., Graham, S., De Hormaeche, R. D., Musson, J. A., Robinson, J. H., Mastroeni, P., Khan, C. M. A., and Hormaeche, C. E. (2004) Attenuated Salmonella typhimurium htrA mutants cause fatal infections in mice deficient in NADPH oxidase and destroy NADPH oxidase-deficient macrophage monolayers. *Vaccine* 22, 4124–4131.
- (23) Stritzker, J., Janda, J., Schoen, C., Taupp, M., Pilgrim, S., Gentshev, I., Schreier, P., Geginat, G., and Goebel, W. (2004) Growth, virulence, and immunogenicity of Listeria monocytogenes aro mutants. *Infect. Immun.* 72, 5622–5629.
- (24) Braus, G. H. (1991) Aromatic amino acid biosynthesis in the yeast Saccharomyces cerevisiae: a model system for the regulation of a eukaryotic biosynthetic pathway. *Microbiol. Rev.* 55, 349–370.

- (25) Walker, G. E., Dunbar, B., Hunter, I. S., Nimmo, H. G., and Coggins, J. R. (1996) Evidence for a novel class of microbial 3-deoxy-D-arabino-heptulosonate-7-phosphate synthase in *Streptomyces coelicolor* A3(2), *Streptomyces rimosus* and *Neurospora crassa*. *Microbiology (Reading, Engl.)* 142 (Pt 8), 1973–1982.
- (26) Schnappauf, G., Hartmann, M., Künzler, M., and Braus, G. H. (1998) The two 3-deoxy-D-arabino-heptulosonate-7-phosphate synthase isoenzymes from *Saccharomyces cerevisiae* show different kinetic modes of inhibition. *Arch. Microbiol.* 169, 517–524.
- (27) Subramaniam, P. S., Xie, G., Xia, T., and Jensen, R. A. (1998) Substrate ambiguity of 3-deoxy-D-manno-octulosonate 8-phosphate synthase from *Neisseria gonorrhoeae* in the context of its membership in a protein family containing a subset of 3-deoxy-D-arabino-heptulosonate 7-phosphate synthases. *J. Bacteriol.* 180, 119–127.
- (28) Paravicini, G., Schmidheini, T., and Braus, G. (1989) Purification and properties of the 3-deoxy-D-arabino-heptulosonate-7-phosphate synthase (phenylalanine-inhibitable) of *Saccharomyces cerevisiae*. *Eur. J. Biochem.* 186, 361–366.
- (29) Birck, M. R., and Woodard, R. W. (2001) *Aquifex aeolicus* 3-deoxy-D-manno-2-octulosonic acid 8-phosphate synthase: a new class of KDO 8-P synthase? *J. Mol. Evol.* 52, 205–214.
- (30) Gosset, G., Bonner, C. A., and Jensen, R. A. (2001) Microbial origin of plant-type 2-keto-3-deoxy-D-arabino-heptulosonate 7-phosphate synthases, exemplified by the chorismate- and tryptophan-regulated enzyme from *Xanthomonas campestris*. *J. Bacteriol.* 183, 4061–4070.
- (31) Jensen, R. A., Xie, G., Calhoun, D. H., and Bonner, C. A. (2002) The correct phylogenetic relationship of KdsA (3-deoxy-d-manno-octulosonate 8-phosphate synthase) with one of two independently evolved classes of AroA (3-deoxy-d-arabino-heptulosonate 7-phosphate synthase). *J. Mol. Evol.* 54, 416–423.
- (32) Doy, C. H., and Brown, K. D. (1965) Control of aromatic biosynthesis: the multiplicity of 7-phospho-2-oxo-3-deoxy-D-arabino-heptonate D-erythrose-4-phosphate-lyase (pyruvate-phosphorylating) in *Escherichia coli* W. *Biochim. Biophys. Acta* 104, 377–389.
- (33) Brown, K. D., and Doy, C. H. (1966) Control of three isoenzymic 7-phospho-2-oxo-3-deoxy-D-arabino-heptonate-D-erythrose-4-phosphate lyases of *Escherichia coli* W and derived mutants by repressive and “inductive” effects of the aromatic amino acids. *Biochim. Biophys. Acta* 118, 157–172.

- (34) Schoner, R., and Herrmann, K. M. (1976) 3-Deoxy-D-arabino-heptulosonate 7-phosphate synthase. Purification, properties, and kinetics of the tyrosine-sensitive isoenzyme from *Escherichia coli*. *J. Biol. Chem.* 251, 5440–5447.
- (35) Stephens, C. M., and Bauerle, R. (1991) Analysis of the metal requirement of 3-deoxy-D-arabino-heptulosonate-7-phosphate synthase from *Escherichia coli*. *J. Biol. Chem.* 266, 20810–20817.
- (36) Akowski, J. P., and Bauerle, R. (1997) Steady-state kinetics and inhibitor binding of 3-deoxy-D-arabino-heptulosonate-7-phosphate synthase (tryptophan sensitive) from *Escherichia coli*. *Biochemistry* 36, 15817–15822.
- (37) Ahmad, S., Rightmire, B., and Jensen, R. A. (1986) Evolution of the regulatory isozymes of 3-deoxy-D-arabino-heptulosonate 7-phosphate synthase present in the *Escherichia coli* genealogy. *J. Bacteriol.* 165, 146–154.
- (38) Whitaker, R. J., Fiske, M. J., and Jensen, R. A. (1982) *Pseudomonas aeruginosa* possesses two novel regulatory isozymes of 3-deoxy-D-arabino-heptulosonate 7-phosphate synthase. *J. Biol. Chem.* 257, 12789–12794.
- (39) Webby, C. J., Jiao, W., Hutton, R. D., Blackmore, N. J., Baker, H. M., Baker, E. N., Jameson, G. B., and Parker, E. J. (2010) Synergistic allostery, a sophisticated regulatory network for the control of aromatic amino acid biosynthesis in *Mycobacterium tuberculosis*. *J. Biol. Chem.* 285, 30567–30576.
- (40) Wu, J., Sheflyan, G. Y., and Woodard, R. W. (2005) *Bacillus subtilis* 3-deoxy-D-arabino-heptulosonate 7-phosphate synthase revisited: resolution of two long-standing enigmas. *Biochem. J.* 390, 583–590.
- (41) Wu, J., and Woodard, R. W. (2006) New insights into the evolutionary links relating to the 3-deoxy-D-arabino-heptulosonate 7-phosphate synthase subfamilies. *J. Biol. Chem.* 281, 4042–4048.
- (42) Camakaris, H., and Pittard, J. (1973) Regulation of tyrosine and phenylalanine biosynthesis in *Escherichia coli* K-12: properties of the *tyrR* gene product. *J. Bacteriol.* 115, 1135–1144.
- (43) Grove, C. L., and Gunsalus, R. P. (1987) Regulation of the *aroH* operon of *Escherichia coli* by the tryptophan repressor. *J. Bacteriol.* 169, 2158–2164.
- (44) Cornish, E. C., Argyropoulos, V. P., Pittard, J., and Davidson, B. E. (1986) Structure of the *Escherichia coli* K12 regulatory gene *tyrR*. Nucleotide sequence and sites of initiation of transcription and translation. *J. Biol. Chem.* 261, 403–410.

- (45) Im, S. W., and Pittard, J. (1973) Tyrosine and phenylalanine biosynthesis in *Escherichia coli* K-12: complementation between different *tyrR* alleles. *J. Bacteriol.* *115*, 1145–1150.
- (46) Ganson, R. J., D'Amato, T. A., and Jensen, R. A. (1986) The Two-Isozyme System of 3-Deoxy-d-arabino-Heptulosonate 7-Phosphate Synthase in *Nicotiana glauca* and Other Higher Plants. *Plant Physiol.* *82*, 203–210.
- (47) Doong, R. L., Ganson, R. J., and Jensen, R. A. (1993) Plastid-localized 3-deoxy-D-arabino-heptulosonate 7-phosphate synthase (DS-Mn): the early-pathway target of sequential feedback inhibition in higher plants. *Plant Cell. Environ.* *16*, 393–402.
- (48) Suzich, J. A., Dean, J. F. D., and Herrmann, K. M. 3-Deoxy-d-arabino-Heptulosonate 7-Phosphate Synthase from Carrot Root (*Daucus carota*) Is a Hysteretic Enzyme.
- (49) Pinto, J. E. B. P., Dyer, W. E., Weller, S. C., and Herrmann, K. M. (1988) Glyphosate Induces 3-Deoxy-d-arabino-Heptulosonate 7-Phosphate Synthase in Potato (*Solanum tuberosum* L.) Cells Grown in Suspension Culture. *Plant Physiol.* *87*, 891.
- (50) Ray, J. M., and Bauerle, R. (1991) Purification and properties of tryptophan-sensitive 3-deoxy-D-arabino-heptulosonate-7-phosphate synthase from *Escherichia coli*. *J. Bacteriol.* *173*, 1894–1901.
- (51) Baasov, T., and Knowles, J. R. (1989) Is the first enzyme of the shikimate pathway, 3-deoxy-D-arabino-heptulosonate-7-phosphate synthase (tyrosine sensitive), a copper metalloenzyme? *J. Bacteriol.* *171*, 6155.
- (52) König, V., Pfeil, A., Braus, G. H., and Schneider, T. R. (2004) Substrate and metal complexes of 3-deoxy-D-arabino-heptulosonate-7-phosphate synthase from *Saccharomyces cerevisiae* provide new insights into the catalytic mechanism. *J. Mol. Biol.* *337*, 675–690.
- (53) Shumilin, I. A., Bauerle, R., Wu, J., Woodard, R. W., and Kretsinger, R. H. (2004) Crystal structure of the reaction complex of 3-deoxy-D-arabino-heptulosonate-7-phosphate synthase from *Thermotoga maritima* refines the catalytic mechanism and indicates a new mechanism of allosteric regulation. *J. Mol. Biol.* *341*, 455–466.
- (54) Shumilin, I. A., Kretsinger, R. H., and Bauerle, R. H. (1999) Crystal structure of phenylalanine-regulated 3-deoxy-D-arabino-heptulosonate-7-phosphate synthase from *Escherichia coli*. *Structure* *7*, 865–875.

- (55) Shumilin, I. A., Zhao, C., Bauerle, R., and Kretsinger, R. H. (2002) Allosteric inhibition of 3-deoxy-D-arabino-heptulosonate-7-phosphate synthase alters the coordination of both substrates. *J. Mol. Biol.* *320*, 1147–1156.
- (56) Levin, D., and Racker, E. (1959) Condensation of arabinose 5-phosphate and phosphorylenol pyruvate by 2-keto-3-deoxy-8-phosphooctonic acid synthetase. *J. Biol. Chem.* *234*, 2532–2539.
- (57) Comb, D. G., and Roseman, S. (1960) The sialic acids. I. The structure and enzymatic synthesis of N-acetylneuraminic acid. *J. Biol. Chem.* *235*, 2529–2537.
- (58) Raetz, C. R. (1990) Biochemistry of endotoxins. *Annu. Rev. Biochem.* *59*, 129–170.
- (59) Ghalambor, M. A., and Heath, E. C. (1966) The biosynthesis of cell wall lipopolysaccharide in *Escherichia coli*. IV. Purification and properties of cytidine monophosphate 3-deoxy-d-manno-octulosonate synthetase. *J. Biol. Chem.* *241*, 3216–3221.
- (60) Vaara, M. (1993) Antibiotic-supersusceptible mutants of *Escherichia coli* and *Salmonella typhimurium*. *Antimicrob. Agents Chemother.* *37*, 2255–2260.
- (61) Raetz, C. R. H., and Whitfield, C. (2002) Lipopolysaccharide endotoxins. *Annu. Rev. Biochem.* *71*, 635–700.
- (62) Brozek, K. A., and Raetz, C. R. (1990) Biosynthesis of lipid A in *Escherichia coli*. Acyl carrier protein-dependent incorporation of laurate and myristate. *J. Biol. Chem.* *265*, 15410–15417.
- (63) Goldman, R., Kohlbrenner, W., Lartey, P., and Pernet, A. (1987) Antibacterial agents specifically inhibiting lipopolysaccharide synthesis. *Nature* *329*, 162–164.
- (64) Rick, P. D., and Osborn, M. J. (1972) Isolation of a mutant of *Salmonella typhimurium* dependent on D-arabinose-5-phosphate for growth and synthesis of 3-deoxy-D-mannoctulosonate (ketodeoxyoctonate). *PNAS* *69*, 3756–3760.
- (65) Rick, P. D., and Osborn, M. J. (1977) Lipid A mutants of *Salmonella typhimurium*. Characterization of a conditional lethal mutant in 3-deoxy-D-mannoctulosonate-8-phosphate synthetase. *J. Biol. Chem.* *252*, 4895–4903.
- (66) Cochrane, F. C., Cookson, T. V. M., Jameson, G. B., and Parker, E. J. (2009) Reversing evolution: re-establishing obligate metal ion dependence in a metal-independent KDO8P synthase. *J. Mol. Biol.* *390*, 646–661.

- (67) Traving, C., and Schauer, R. (1998) Structure, function and metabolism of sialic acids. *Cell. Mol. Life Sci.* 54, 1330–1349.
- (68) Tanner, M. E. (2005) The enzymes of sialic acid biosynthesis. *Bioorganic Chemistry* 33, 216–228.
- (69) Huang, H.-H., Liao, H.-K., Chen, Y.-J., Hwang, T.-S., Lin, Y.-H., and Lin, C.-H. (2005) Structural characterization of sialic acid synthase by electrospray mass spectrometry--a tetrameric enzyme composed of dimeric dimers. *J. Am. Soc. Mass Spectrom.* 16, 324–332.
- (70) Gunawan, J., Simard, D., Gilbert, M., Lovering, A. L., Wakarchuk, W. W., Tanner, M. E., and Strynadka, N. C. J. (2005) Structural and mechanistic analysis of sialic acid synthase NeuB from *Neisseria meningitidis* in complex with Mn²⁺, phosphoenolpyruvate, and N-acetylmannosaminol. *J. Biol. Chem.* 280, 3555–3563.
- (71) Hao, J., Balagurumoorthy, P., Sarilla, S., and Sundaramoorthy, M. (2005) Cloning, expression, and characterization of sialic acid synthases. *Biochem. Biophys. Res. Commun.* 338, 1507–1514.
- (72) Baardsnes, J., and Davies, P. L. (2001) Sialic acid synthase: the origin of fish type III antifreeze protein? *Trends Biochem. Sci.* 26, 468–469.
- (73) Asojo, O., Friedman, J., Adir, N., Belakhov, V., Shoham, Y., and Baasov, T. (2001) Crystal structures of KDOP synthase in its binary complexes with the substrate phosphoenolpyruvate and with a mechanism-based inhibitor. *Biochemistry* 40, 6326–6334.
- (74) Li, Z., Sau, A. K., Shen, S., Whitehouse, C., Baasov, T., and Anderson, K. S. (2003) A Snapshot of Enzyme Catalysis Using Electrospray Ionization Mass Spectrometry. *J. Am. Chem. Soc.* 125, 9938–9939.
- (75) Kona, F., Xu, X., Martin, P., Kuzmic, P., and Gatti, D. L. (2007) Structural and mechanistic changes along an engineered path from metallo to nonmetallo 3-deoxy-D-manno-octulosonate 8-phosphate synthases. *Biochemistry* 46, 4532–4544.
- (76) Howe, D. L., Sundaram, A. K., Wu, J., Gatti, D. L., and Woodard, R. W. (2003) Mechanistic insight into 3-deoxy-D-manno-octulosonate-8-phosphate synthase and 3-deoxy-D-arabino-heptulosonate-7-phosphate synthase utilizing phosphorylated monosaccharide analogues. *Biochemistry* 42, 4843–4854.
- (77) Dewel, H. S., Radaev, S., Wang, J., Woodard, R. W., and Gatti, D. L. (2001) Substrate and metal complexes of 3-deoxy-D-manno-octulosonate-8-

- phosphate synthase from *Aquifex aeolicus* at 1.9-Å resolution. Implications for the condensation mechanism. *J. Biol. Chem.* *276*, 8393–8402.
- (78) Hedstrom, L., and Abeles, R. (1988) 3-Deoxy-D-Manno-Octulosonate-8-Phosphate Synthase Catalyzes the C-O Bond-Cleavage of Phosphoenolpyruvate. *Biochem. Biophys. Res. Commun.* *157*, 816–820.
- (79) Clark, M. E., and Berti, P. J. (2007) Enolpyruvyl Activation by Enolpyruvylshikimate-3-phosphate Synthase †. *Biochemistry* *46*, 1933–1940.
- (80) Tao, P., Gatti, D. L., and Schlegel, H. B. (2009) The energy landscape of 3-deoxy-D-manno-octulosonate 8-phosphate synthase. *Biochemistry* *48*, 11706–11714.
- (81) Kohen, A., Jakob, A., and Baasov, T. (1992) Mechanistic studies of 3-deoxy-D-manno-2-octulosonate-8-phosphate synthase from *Escherichia coli*. *Eur. J. Biochem.* *208*, 443–449.
- (82) Dotson, G. D., Nanjappan, P., Reily, M. D., and Woodard, R. W. (1993) Stereochemistry of 3-deoxyoctulosonate 8-phosphate synthase. *Biochemistry* *32*, 12392–12397.
- (83) Floss, H. G., Onderka, D. K., and Carroll, M. (1972) Stereochemistry of the 3-deoxy-D-arabino-heptulosonate 7-phosphate synthetase reaction and the chorismate synthetase reaction. *J. Biol. Chem.* *247*, 736–744.
- (84) Dotson, G. D., Dua, R. K., Clemens, J. C., Wooten, E. W., and Woodard, R. W. (1995) Overproduction and one-step purification of *Escherichia coli* 3-deoxy-D-manno-octulosonic acid 8-phosphate synthase and oxygen transfer studies during catalysis using isotopic-shifted heteronuclear NMR. *J. Biol. Chem.* *270*, 13698–13705.
- (85) Sundaram, A. K., PITTS, L., MUHAMMAD, K., Wu, J., BETENBAUGH, M., Woodard, R. W., and VANN, W. F. (2004) Characterization of N-acetylneuraminic acid synthase isoenzyme 1 from *Campylobacter jejuni*. *Biochem. J.* *383*, 83.
- (86) Hopkins, A. L., and Groom, C. R. (2002) The druggable genome. *Nat. Rev. Drug. Discov.* *1*, 727–730.
- (87) Copeland, R. A. (2005) Evaluation of enzyme inhibitors in drug discovery. A guide for medicinal chemists and pharmacologists. *Methods Biochem Anal* *46*, 1–265.

- (88) Segel, I. H. (1993) *Enzyme Kinetics: Behavior and Analysis of Rapid Equilibrium and Steady-State Enzyme Systems* (Wiley Classics Library). Wiley-Interscience.
- (89) Wolfenden, R., and Snider, M. J. (2001) The Depth of Chemical Time and the Power of Enzymes as Catalysts. *Acc. Chem. Res.* *34*, 938–945.
- (90) Fersht, A. (1985) *Enzyme Structure and Mechanism* 2nd ed. W H Freeman & Co (Sd).
- (91) Berti, P. J., and McCann, J. A. B. (2006) Toward a detailed understanding of base excision repair enzymes: transition state and mechanistic analyses of N-glycoside hydrolysis and N-glycoside transfer. *Chem. Rev.* *106*, 506–555.
- (92) Berti, P., and Tanaka, K. (2002) Transition state analysis using multiple kinetic isotope effects: Mechanisms of enzymatic and non-enzymatic glycoside hydrolysis and transfer. *Adv Phys Org Chem* *37*, 239–314.
- (93) McCann, J. A. B., and Berti, P. J. (2007) Transition state analysis of acid-catalyzed dAMP hydrolysis. *J. Am. Chem. Soc.* *129*, 7055–7064.
- (94) Amyes, T., and Jencks, W. (1989) Lifetimes of Oxocarbenium Ions in Aqueous-Solution From Common Ion Inhibition of the Solvolysis of Alpha-Azido Ethers by Added Azide Ion. *J. Am. Chem. Soc.* *111*, 7888–7900.
- (95) Zhu, J., and Bennet, A. J. (1998) Hydrolysis of (2-Deoxy- α -d-Glucopyranosyl)pyridinium Salts: The 2-Deoxyglucosyl Oxocarbenium Is Not Solvent-Equilibrated in Water. *J. Am. Chem. Soc.* *120*, 3887–3893.
- (96) Lee, J. K., Bain, A. D., and Berti, P. J. (2004) Probing the transition states of four glucoside hydrolyses with ^{13}C kinetic isotope effects measured at natural abundance by NMR spectroscopy. *J. Am. Chem. Soc.* *126*, 3769–3776.
- (97) Huang, X., Surry, C., Hiebert, T., and Bennet, A. (1995) Hydrolysis of (2-Deoxy-Beta-D-Glucopyranosyl)Pyridinium Salts. *J. Am. Chem. Soc.* *117*, 10614–10621.
- (98) Bennet, A. J., and Kitos, T. E. (2002) Mechanisms of glycopyranosyl and 5-thioglycopyranosyl transfer reactions in solution. *J. Chem. Soc., Perkin Trans.* *2* 1207–1222.
- (99) Indurugalla, D., and Bennet, A. J. (2001) A Kinetic Isotope Effect Study on the Hydrolysis Reactions of Methyl Xylopyranosides and Methyl 5-Thioxylopyranosides: Oxygen versus Sulfur Stabilization of Carbenium Ions. *J. Am. Chem. Soc.* *123*, 10889–10898.

- (100) Horenstein, B. A., and Bruner, M. (1998) The N-Acetyl Neuraminyloxocarbenium Ion Is an Intermediate in the Presence of Anionic Nucleophiles. *J. Am. Chem. Soc.* *120*, 1357–1362.
- (101) Zhu, J., and Bennet, A. J. (2000) Solvolyses of 2-Deoxy- α - and β - d-Glucopyranosyl 4'-Bromoisoquinolinium Tetrafluoroborates. *J. Org. Chem.* *65*, 4423–4430.
- (102) Morrison, J. F., and Walsh, C. T. (1988) The behavior and significance of slow-binding enzyme inhibitors. *Adv. Enzymol. Relat. Areas Mol. Biol.* *61*, 201–301.
- (103) Copeland, R. A., Pompliano, D. L., and Meek, T. D. (2007) Drug-target residence time and its implications for lead optimization. *Nat. Rev. Drug. Discov.* *5*, 730–739.
- (104) Lu, H., and Tonge, P. J. (2010) Drug-target residence time: critical information for lead optimization. *Curr Opin Chem Biol* *14*, 467–474.
- (105) Schramm, V. L. (1998) Enzymatic transition states and transition state analog design. *Annu. Rev. Biochem.* *67*, 693–720.
- (106) Morrison, J. F. (1982) The slow-binding and slow, tight-binding inhibition of enzyme-catalysed reactions. *Trends Biochem. Sci.* *7*, 102–105.
- (107) Koshland, D. E., Némethy, G., and Filmer, D. (1966) Comparison of experimental binding data and theoretical models in proteins containing subunits. *Biochemistry* *5*, 365–385.
- (108) Monod, J., Wyman, J., and Changeux, J.-P. (1965) On the nature of allosteric transitions: A plausible model. *J. Mol. Biol.* *12*, 88–118.
- (109) Eaton, W. A., Henry, E. R., Hofrichter, J., and Mozzarelli, A. (1999) Is cooperative oxygen binding by hemoglobin really understood? *Nat. Struct Biol.* *6*, 351–358.
- (110) Abeliovich, H. (2005) An Empirical Extremum Principle for the Hill Coefficient in Ligand-Protein Interactions Showing Negative Cooperativity. *Biophysical Journal* *89*, 76–79.
- (111) Castellani, M., Covian, R., Kleinschroth, T., Anderka, O., Ludwig, B., and Trumppower, B. L. (2009) Direct Demonstration of Half-of-the-sites Reactivity in the Dimeric Cytochrome bc₁ Complex: enzyme with one inactive monomer is fully active but unable to activate the second ubiquinol oxidation site in

- response to ligand binding at the ubiquinone reduction site. *J. Biol. Chem.* **285**, 502–510.
- (112) Shi, J., Dertouzos, J., Gafni, A., Steel, D., and Palfey, B. A. (2006) Single-molecule kinetics reveals signatures of half-sites reactivity in dihydroorotate dehydrogenase A catalysis. *PNAS* **103**, 5775–5780.
- (113) Mochalkin, I., Miller, J. R., Evdokimov, A., Lightle, S., Yan, C., Stover, C. K., and Waldrop, G. L. (2008) Structural evidence for substrate-induced synergism and half-sites reactivity in biotin carboxylase. *Protein Sci.* **17**, 1706–1718.
- (114) Kline, P. C., and Schramm, V. L. (1993) Purine nucleoside phosphorylase. Catalytic mechanism and transition-state analysis of the arsenolysis reaction. *J. Am. Chem. Soc.* **32**, 13212–13219.
- (115) Miles, R. W., Tyler, P. C., Furneaux, R. H., Bagdassarian, C. K., and Schramm, V. L. (1998) One-Third-the-Sites Transition-State Inhibitors for Purine Nucleoside Phosphorylase †. *J. Am. Chem. Soc.* **37**, 8615–8621.
- (116) Walker, S. R., and Parker, E. J. (2006) Synthesis and evaluation of a mechanism-based inhibitor of a 3-deoxy-d-arabino heptulosonate 7-phosphate synthase. *Bioorg. Med. Chem. Lett.* **16**, 2951–2954.
- (117) Walker, S. R., Jiao, W., and Parker, E. J. (2011) Synthesis and evaluation of dual site inhibitors of 3-deoxy-d-arabino-heptulosonate 7-phosphate synthase. *Bioorg. Med. Chem. Lett.* **21**, 5092–5097.
- (118) Reichau, S., Jiao, W., Walker, S. R., Hutton, R. D., Baker, E. N., and Parker, E. J. (2011) Potent Inhibitors of a Shikimate Pathway Enzyme from *Mycobacterium tuberculosis*: combining mechanism- and modeling-based design. *J. Biol. Chem.* **286**, 16197–16207.
- (119) Walker, S. R., Cumming, H., and Parker, E. J. (2009) Substrate and reaction intermediate mimics as inhibitors of 3-deoxy-d-arabino-heptulosonate 7-phosphate synthase. *Org. Biomol. Chem.* **7**, 3031–3035.
- (120) Forlani, G., Lejczak, B., and Kafarski, P. (1999) The Herbicidally Active Compound N-2-(6-Methyl-Pyridyl)-Aminomethylene Bisphosphonic Acid Inhibits In Vivo Aromatic Biosynthesis. *J Plant Growth Regul* **18**, 73–79.
- (121) Du, S., Faiger, H., Belakhov, V., and Baasov, T. (1999) Towards the development of novel antibiotics: synthesis and evaluation of a mechanism-based inhibitor of Kdo8P synthase. *Trends Biochem. Sci.* **7**, 2671–2682.

- (122) Belakhov, V., Dovgolevsky, E., Rabkin, E., Shulami, S., Shoham, Y., and Baasov, T. (2004) Synthesis and evaluation of a mechanism-based inhibitor of KDO8P synthase. *Carbohydr. Res.* 339, 385–392.
- (123) Liu, F., Lee, H. J., Strynadka, N. C. J., and Tanner, M. E. (2009) Inhibition of *Neisseria meningitidis* Sialic Acid Synthase by a Tetrahedral Intermediate Analogue. *Biochemistry* 48, 9194–9201.
- (124) Popovic, V. (2012) Inhibition of the bacterial sialic acid synthase, NeuB. *Masters Thesis, McMaster University*, 62 p.
- (125) Morrison, E. (2009) NeuNac oxime: a potent inhibitor of the sialic acid synthase, NeuB. *Masters Thesis, McMaster University*, 79 p.
- (126) Edelhoch, H. (1967) Spectroscopic determination of tryptophan and tyrosine in proteins. *Biochemistry* 6, 1948–1954.
- (127) Pace, C. N., Vajdos, F., Fee, L., Grimsley, G., and Gray, T. (1995) How to measure and predict the molar absorption coefficient of a protein. *Protein Sci.* 4, 2411–2423.
- (128) Lanzetta, P. A., Alvarez, L. J., Reinach, P. S., and Candia, O. A. (1979) An improved assay for nanomole amounts of inorganic phosphate. *Anal. Biochem.* 100, 95–97.
- (129) Sieben, A. S., Perlin, A. S., and Simpson, F. J. (1966) An improved preparative method for D-erythrose 4-phosphate. *Can. J. Biochem.* 44, 663–669.
- (130) Blum, H., Beier, H., and Gross, H. J. (1987) Improved silver staining of plant proteins, RNA and DNA in polyacrylamide gels. *Electrophoresis* 8, 93–99.
- (131) McCandliss, R. J., Poling, M. D., and Herrmann, K. M. (1978) 3-Deoxy-D-arabino-heptulosonate 7-phosphate synthase. Purification and molecular characterization of the phenylalanine-sensitive isoenzyme from *Escherichia coli*. *J. Biol. Chem.* 253, 4259–4265.
- (132) Ouellet, H., Podust, L. M., and de Montellano, P. R. O. (2008) *Mycobacterium tuberculosis* CYP130: crystal structure, biophysical characterization, and interactions with antifungal azole drugs. *J. Biol. Chem.* 283, 5069–5080.
- (133) Furdui, C., Zhou, L., Woodard, R. W., and Anderson, K. S. (2004) Insights into the mechanism of 3-deoxy-D-arabino-heptulosonate 7-phosphate synthase

- (Phe) from *Escherichia coli* using a transient kinetic analysis. *J. Biol. Chem.* **279**, 45618–45625.
- (134) Sundaram, A. K., Howe, D. L., Sheflyan, G. Y., and Woodard, R. W. (1998) Probing the potential metal binding site in *Escherichia coli* 3-deoxy-D-arabino-heptulosonate 7-phosphate synthase (phenylalanine-sensitive). *FEBS Lett.* **441**, 195–199.
- (135) Tran, D., Pietersma, A. L., Schofield, L. R., Rost, M., Jameson, G. B., and Parker, E. J. (2011) Investigating the role of the hydroxyl groups of substrate erythrose 4-phosphate in the reaction catalysed by the first enzyme of the shikimate pathway. *Bioorg. Med. Chem. Lett.* **21**, 6838–6841.
- (136) Shumilin, I. A., Bauerle, R., and Kretsinger, R. H. (2003) The high-resolution structure of 3-deoxy-D-arabino-heptulosonate-7-phosphate synthase reveals a twist in the plane of bound phosphoenolpyruvate. *Biochemistry* **42**, 3766–3776.
- (137) Bode, R., Melo Ramos, C., and Birnbaum, D. (1984) Inhibition of tyrosine-sensitive 3-deoxy-d-arabino-heptulosonate 7-phosphate synthase by glyphosate in *Candida maltosa*. *Electrophoresis* **23**, 7–10.
- (138) Ganson, R. J., and Jensen, R. A. (1988) The essential role of cobalt in the inhibition of the cytosolic isozyme of 3-deoxy-D-arabino-heptulosonate-7-phosphate synthase from *Nicotiana glauca* by glyphosate. *Arch. Biochem. Biophys.* **260**, 85–93.
- (139) Rubin, J. L., Gaines, C. G., and Jensen, R. A. (1982) Enzymological Basis for Herbicidal Action of Glyphosate. *Plant Physiol.* **70**, 833.
- (140) Subramaniam, V., and Hoggard, P. E. (1988) Metal complexes of glyphosate. *J. Agric. Food Chem.* **36**, 1326–1329.
- (141) Heineke, D., Franklin, S. J., and Raymond, K. N. (1994) Coordination chemistry of glyphosate: structural and spectroscopic characterization of bis (glyphosate) metal (III) complexes. *Inorg. Chem.* **33**, 2413–2421.
- (142) Eftink, M. R., Anusiem, A. C., and Biltonen, R. L. (1983) Enthalpy-entropy compensation and heat capacity changes for protein-ligand interactions: general thermodynamic models and data for the binding of nucleotides to ribonuclease A. *Biochemistry* **22**, 3884–3896.
- (143) Benkovic, S. J., Hammes, G. G., and Hammes-Schiffer, S. (2008) Free-Energy Landscape of Enzyme Catalysis †. *J. Am. Chem. Soc.* **130**, 3317–3321.

- (144) Goutelle, S., Maurin, M., Rougier, F., Barbaut, X., Bourguignon, L., Ducher, M., and Maire, P. (2008) The Hill equation: a review of its capabilities in pharmacological modelling. *Fundam. Clin. Pharmacol.* 22, 633–648.
- (145) Cornish-Bowden, A., and Cárdenas, M. L. (1987) Co-operativity in monomeric enzymes. *J. Theor. Biol.* 124, 1–23.
- (146) Blow, D. M., and Steitz, T. A. (1970) X-ray diffraction studies of enzymes. *Annu. Rev. Biochem.* 39, 63–100.
- (147) Blow, D. M., BIRKTOFT, J. J., and HARTLEY, B. S. (1969) Role of a Buried Acid Group in the Mechanism of Action of Chymotrypsin. *Nature* 221, 337–340.
- (148) Copeland, R. A. (2000) *Enzymes: A Practical Introduction to Structure, Mechanism, and Data Analysis* 2nd ed. Wiley-VCH.
- (149) Navia, M. A., Fitzgerald, P. M., McKeever, B. M., Leu, C. T., Heimbach, J. C., Herber, W. K., Sigal, I. S., Darke, P. L., and Springer, J. P. (1989) Three-dimensional structure of aspartyl protease from human immunodeficiency virus HIV-1. *Nature* 337, 615–620.
- (150) Wlodawer, A., Miller, M., Jaskólski, M., Sathyanarayana, B. K., Baldwin, E., Weber, I. T., Selk, L. M., Clawson, L., Schneider, J., and Kent, S. B. (1989) Conserved folding in retroviral proteases: crystal structure of a synthetic HIV-1 protease. *Science* 245, 616–621.
- (151) Jaskolski, M., Tomasselli, A. G., Sawyer, T. K., Staples, D. G., Heinrikson, R. L., Schneider, J., Kent, S. B. H., and Wlodawer, A. (1991) Structure at 2.5-Å resolution of chemically synthesized Human Immunodeficiency Virus Type 1 protease complexed with a hydroxyethylene-based inhibitor. *J. Am. Chem. Soc.* 113, 1600–1609.
- (152) Brik, A., and Wong, C.-H. (2003) HIV-1 protease: mechanism and drug discovery. *Org. Biomol. Chem.* 1, 5–14.
- (153) K Suguna, E. A. P. C. W. S. W. D. C. D. R. D. (1987) Binding of a reduced peptide inhibitor to the aspartic proteinase from *Rhizopus chinensis*: implications for a mechanism of action. *PNAS* 84, 7009.
- (154) Otwinowski, Z., and minor, W. (2007) Processing of X-ray diffraction data collected in oscillation mode. *Meth. Enzymol.* 276A, 307–326.
- (155) Kitagawa, M., Ara, T., Arifuzzaman, M., Ioka-Nakamichi, T., Inamoto, E., Toyonaga, H., and Mori, H. (2005) Complete set of ORF clones of *Escherichia*

- coli ASKA library (a complete set of E. coli K-12 ORF archive): unique resources for biological research. *DNA Res.* *12*, 291–299.
- (156) Adams, P. D., Grosse-Kunstleve, R. W., Hung, L. W., Ioerger, T. R., McCoy, A. J., Moriarty, N. W., Read, R. J., Sacchettini, J. C., Sauter, N. K., and Terwilliger, T. C. (2002) PHENIX: building new software for automated crystallographic structure determination. *Acta Crystallogr. D Biol. Crystallogr.* *58*, 1948–1954.
- (157) Emsley, P., and Cowtan, K. (2004) Coot: model-building tools for molecular graphics. *Acta Crystallogr. D Biol. Crystallogr.* *60*, 2126–2132.
- (158) Wagner, T., Shumilin, I. A., Bauerle, R., and Kretsinger, R. H. (2000) Structure of 3-deoxy-d-arabino-heptulosonate-7-phosphate synthase from *Escherichia coli*: comparison of the Mn(2+)*2-phosphoglycolate and the Pb(2+)*2-phosphoenolpyruvate complexes and implications for catalysis. *J. Mol. Biol.* *301*, 389–399.
- (159) Jiao, W., Hutton, R. D., Cross, P. J., Jameson, G. B., and Parker, E. J. (2012) Dynamic cross-talk among remote binding sites: the molecular basis for unusual synergistic allostery. *J. Mol. Biol.* *415*, 716–726.
- (160) Popovych, N., Sun, S., Ebright, R. H., and Kalodimos, C. G. (2006) Dynamically driven protein allostery. *Nat. Struct. Mol. Biol.* *13*, 831–838.
- (161) Boyer, P. D. (1997) The ATP synthase--a splendid molecular machine. *Annu. Rev. Biochem.* *66*, 717–749.
- (162) Kline, P. C., and Schramm, V. L. (1992) Purine nucleoside phosphorylase. Inosine hydrolysis, tight binding of the hypoxanthine intermediate, and third-site reactivity. *J. Am. Chem. Soc.* *114*, 5964–5973.
- (163) Seydoux, F., Malhotra, O. P., and Bernhard, S. A. (1974) Half-site reactivity. *CRC Crit. Rev. Biochem.* *2*, 227–257.
- (164) Orozco, M. (2014) A theoretical view of protein dynamics. *Chem. Soc. Rev.*
- (165) Luk, L. Y. P., Javier Ruiz-Pernía, J., Dawson, W. M., Roca, M., Loveridge, E. J., Glowacki, D. R., Harvey, J. N., Mulholland, A. J., Tuñón, I., Moliner, V., and Allemann, R. K. (2013) Unraveling the role of protein dynamics in dihydrofolate reductase catalysis. *PNAS* *110*, 16344–16349.
- (166) Hay, S., and Scrutton, N. S. (2012) Good vibrations in enzyme-catalysed reactions. *Nature Chem.* *4*, 161–168.

- (167) Percy, A. J., Rey, M., Burns, K. M., and Schriemer, D. C. (2012) Probing protein interactions with hydrogen/deuterium exchange and mass spectrometry—a review. *Anal. Chim. Acta* 721, 7–21.
- (168) Benkovic, S. J., and Hammes-Schiffer, S. (2003) A perspective on enzyme catalysis. *Science* 301, 1196–1202.
- (169) Eisenmesser, E. Z., Millet, O., Labeikovsky, W., Korzhnev, D. M., Wolf-Watz, M., Bosco, D. A., Skalicky, J. J., Kay, L. E., and Kern, D. (2005) Intrinsic dynamics of an enzyme underlies catalysis. *Nature* 438, 117–121.
- (170) Kay, L. E. (1998) Protein dynamics from NMR. *Nat. Struct. Mol. Biol.* 5, 513–517.
- (171) Kern, D., and Zuiderweg, E. R. (2003) The role of dynamics in allosteric regulation. *Curr. Opin. Struct. Biol.* 13, 748–757.
- (172) Mulder, F. A. A., Mittermaier, A., Hon, B., Dahlquist, F. W., and Kay, L. E. (2001) Studying excited states of proteins by NMR spectroscopy. *Nat. Struct Biol.* 8, 932–935.
- (173) Wagner, G., and Wüthrich, K. (1982) Amide proton exchange and surface conformation of the basic pancreatic trypsin inhibitor in solution: studies with two-dimensional nuclear magnetic resonance. *J. Mol. Biol.* 160, 343–361.
- (174) Zhang, Z., and Smith, D. L. (1993) Determination of amide hydrogen exchange by mass spectrometry: A new tool for protein structure elucidation. *Protein Sci.* 2, 522–531.
- (175) Wüthrich, K., and Wider, G. (2003) Transverse relaxation–optimized NMR spectroscopy with biomacromolecular structures in solution. *Magn. Reson. Chem.* 41, S80–S88.
- (176) Kitevski-LeBlanc, J. L., and Prosser, R. S. (2012) Current applications of ¹⁹F NMR to studies of protein structure and dynamics. *Prog. Nucl. Magn. Reson. Spectrosc.* 62, 1–33.
- (177) Pervushin, K., Riek, R., Wider, G., and Wüthrich, K. (1997) Attenuated T2 relaxation by mutual cancellation of dipole-dipole coupling and chemical shift anisotropy indicates an avenue to NMR structures of very large biological macromolecules in solution. *PNAS* 94, 12366–12371.
- (178) Tjandra, N., Szabo, A., and Bax, A. (1996) Protein Backbone Dynamics and ¹⁵N Chemical Shift Anisotropy from Quantitative Measurement of Relaxation Interference Effects. *J. Am. Chem. Soc.* 118, 6986–6991.

- (179) Gueron, M., Leroy, J. L., and Griffey, R. H. (1983) Proton nuclear magnetic relaxation of nitrogen-15-labeled nucleic acids via dipolar coupling and chemical shift anisotropy. *J. Am. Chem. Soc.* *105*, 7262–7266.
- (180) Loewen, M. C., Klein-Seetharaman, J., Getmanova, E. V., Reeves, P. J., Schwalbe, H., and Khorana, H. G. (2001) How activated receptors couple to G proteins. *PNAS* *98*, 4888–4892.
- (181) Rob, T., Liuni, P., Gill, P. K., Zhu, S., Balachandran, N., Berti, P. J., and Wilson, D. J. (2012) Measuring dynamics in weakly structured regions of proteins using microfluidics-enabled subsecond h/d exchange mass spectrometry. *Anal. Chem.* *84*, 3771–3779.
- (182) Englander, S. W. (2006) Hydrogen exchange and mass spectrometry: A historical perspective. *J. Am. Soc. Mass Spectrom.* *17*, 1481–1489.
- (183) Frieden, C., Hoeltzli, S. D., and Bann, J. G. (2004) The preparation of ¹⁹F-labeled proteins for NMR studies. *Meth. Enzymol.* *380*, 400–415.
- (184) Molday, R. S., Englander, S. W., and Kallen, R. G. (1972) Primary structure effects on peptide group hydrogen exchange. *Biochemistry* *11*, 150–158.
- (185) Yawen Bai, J. S. M. L. M. S. W. E. (1993) Primary Structure Effects on Peptide Group Hydrogen Exchange. *Proteins* *17*, 75.
- (186) Konermann, L., Pan, J., and Liu, Y.-H. (2011) Hydrogen exchange mass spectrometry for studying protein structure and dynamics. *Chem. Soc. Rev.* *40*, 1224–1234.
- (187) Kraut, J. (1988) How do enzymes work? *Science* *242*, 533–540.
- (188) Kurz, J. L. (1963) Transition state characterization for catalyzed reactions. *J. Am. Chem. Soc.* *85*, 987–991.
- (189) Eyring, H. (1935) The Activated Complex in Chemical Reactions. *J. Chem. Phys.* *3*, 107–115.
- (190) Wynne-Jones, W. F. K., and Eyring, H. (1935) The Absolute Rate of Reactions in Condensed Phases. *J. Chem. Phys.* *3*, 492–502.
- (191) Evans, M. G., and Polanyi, M. (1935) Some applications of the transition state method to the calculation of reaction velocities, especially in solution. *Trans. Faraday Soc.* *31*, 875.

- (192) Mader, M. M., and Bartlett, P. A. (1997) Binding Energy and Catalysis: The Implications for Transition-State Analogs and Catalytic Antibodies. *Chem. Rev.* 97, 1281–1302.
- (193) Wolfenden, R. (1972) Analog approaches to the structure of the transition state in enzyme reactions. *Acc. Chem. Res.* 5, 10–18.
- (194) Lienhard, G. E. (1973) Enzymatic catalysis and transition-state theory. *Science* 180, 149–154.
- (195) To, F. (2013) Analysis of DAHP Oxime as a Transition State Mimic of DAHP Synthase. *Undergraduate Thesis, McMaster University*, 27 p.
- (196) Baba, T., Ara, T., Hasegawa, M., Takai, Y., Okumura, Y., Baba, M., Datsenko, K. A., Tomita, M., Wanner, B. L., and Mori, H. (2006) Construction of Escherichia coli K-12 in-frame, single-gene knockout mutants: the Keio collection. *Mol. Syst. Biol.* 2.
- (197) Byczynski, B., Mizyed, S., and Berti, P. J. (2003) Nonenzymatic breakdown of the tetrahedral (alpha-carboxyketal phosphate) intermediates of MurA and AroA, two carboxyvinyl transferases. Protonation of different functional groups controls the rate and fate of breakdown. *J. Am. Chem. Soc.* 125, 12541–12550.
- (198) Loncke, P. G., and Berti, P. J. (2006) Implications of protonation and substituent effects for C-O and O-P bond cleavage in phosphate monoesters. *J. Am. Chem. Soc.* 128, 6132–6140.